High-order harmonic generation in laser-produced plasmas

Johannes Nathan Raphaël Maria Mathijssen

VRIJE UNIVERSITEIT

High-order harmonic generation in laser-produced plasmas

ACADEMISCH PROEFSCHRIFT

ter verkrijging van de graad van Doctor of Philosophy aan
de Vrije Universiteit Amsterdam,
op gezag van de rector magnificus,
prof. dr. J.J.G. Geurts,
volgens besluit van de decaan
van de Faculteit der Bètawetenschappen
in het openbaar te verdedigen
op dinsdag 25 maart 2025 om 13.45 uur
in de universiteit

door

Johannes Nathan Raphaël Maria Mathijssen

geboren te Leiden

promotoren:	prof.dr. S.M. Witte
	prof.dr. K.S.E. Eikema
promotiecommissie:	dr. O.O. Versolato
	dr. L.S. Dreissen
	prof.dr. H.L. Offerhaus
	prof.dr.ir. H.B. van Linden van den Heuvell
	dr. A.S. Stodolna

This work was carried out at the Advanced Research Center for Nanolithography (ARCNL), a public-private partnership between the University of Amsterdam (UvA), Vrije Universiteit Amsterdam (VU), Rijksuniversiteit Groningen (RUG), the Dutch Research Council (NWO), and the semiconductor equipment manufacturer ASML.

Cover: The front cover shows an artist impression of the high-order harmonic generation process in a metallic plasma cloud near the surface of the target. The back cover shows a microscope image of a crater on the surface of a tin target, pierced by the fundamental laser that drives the high-order harmonic generation process. Concept and design by J.N.R.M. Mathijssen.
Printed by: ProefschriftMaken
ISBN: 978-94-6510-486-7
DOI: http://doi.org/10.5463/thesis.1015
A digital version of this thesis is available at: https://research.vu.nl/

Contents

Chapter 1

Introduction

1.1 Metrology

During the last decades, the development of computers has undergone a tremendous progress. Whereas large scale computers with a size of a complete room were employed for decrypting messages, or to calculate trajectories within the gravitational field of the Earth in the middle of previous century, much faster devices which fit in ones hand are nowadays part of our everyday life. This technological advancement shows the still ongoing revolution based on miniaturization of computers, leading to ever faster and smaller electronic devices. At the core of this revolution lies the invention of the transistor, an electronic component capable of switching electronic signals to allow for logical operations and computations. Shrinking down the size of this component has led to an exponential increase of the amount of transistors that can be fitted onto a given surface area, and consequently increasing the computational power of a computer chip, which is commonly referred to as an integrated circuit (IC). This trend has been described by Gordon Moore in 1965, stating that the number of transistors on an IC would double every year [1]. Ten years later, this observation, currently referred to as Moore's Law, has been altered and now refers to a doubling on the amount of transistors on an IC every two years [2]. Up to this day, Moore's law is still a driving factor behind the further miniaturization of transistors. As of now, computer chips with feature sizes, or critical dimension (CD), of few nanometers have been achieved. A zoomed in image of a modern computer chip is shown in figure 1.1, depicting its small features and complex architecture.

As the CD of computer chips decreases further and further, the manufacturing process becomes increasingly difficult. As can be seen in Fig. 1.1, modern chips have complex three-dimensional structures, which are built up layer by layer. It is of vital importance for the performance of the chip that these overlapping layers must be overlaid onto each other with extreme precision. For that reason, alignment and overlay markers are manufactured along with the ICs to locally measure

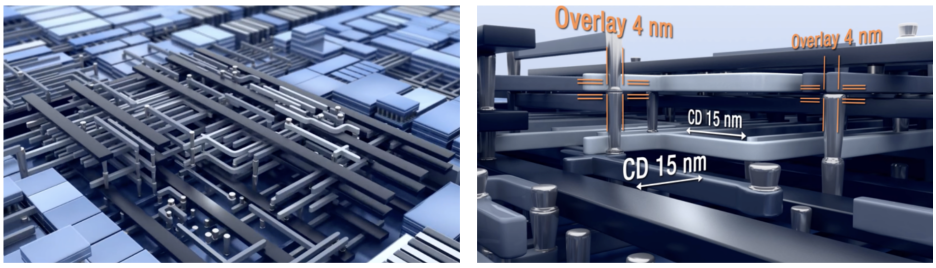

Figure 1.1: Illustrations of lithographic nanostructures, showing multiple-layer nanometer-sized structures, containing different materials. Typical scales for layer-to-layer positioning accuracy (overlay) and critical dimension (CD) are indicated. Illustrations by ASML.

the position of the silicon wafer on which the chips are being manufactured and to measure the position of printed structures with respect to underlying layers, respectively. Such markers are typically a set of gratings oriented horizontally and vertically to measure both x and y position or overlap. As the criteria for overlap error decreases with smaller CD, so must the grating size and pitch of the overlay marker. If we consider the grating equation

$$\frac{\lambda m}{d} = \sin\theta_i - \sin\theta_m, \tag{1.1}$$

in which λ is the probe beam wavelength, m the diffraction order, d the grating pitch, and θ_i and θ_m the angles of incidence and diffraction of order m with respect to the grating normal, respectively. For a probe beam incident at $\theta_i = 0$, solving Eq. 1.1 for θ_m gives

$$\theta_m = \arcsin(-\frac{\lambda m}{d}). \tag{1.2}$$

From this, we can see that the 1st and -1st diffraction orders only exist when $\lambda < d$. Thus, coherent light sources with small wavelengths are required to increase overlay metrology precision.

1.2 High-order harmonic generation

High-order harmonic generation (HHG) is a technique that allows for the production of coherent radiation in the extreme ultraviolet (EUV) spectral range in a compact tabletop setup. This technique, in which intense laser pulses with femtosecond durations interact nonlinearly with a generation medium (mostly noble gases) to produce odd multiples of the driving laser frequency, was discovered in the late eighties [3–5]. Besides being an established route towards shorter wavelengths, the inherent nature of the HHG process also opens pathways to light pulses as short as several tens of attoseconds. The technology has been well

studied over the last decades and is now theoretically well understood [6, 7].

1.2.1 Three step model

Microscopic effects between the drive laser (fundamental) and the generation medium can be described by the three step model [8, 9]. A schematic representation of this model is displayed in Fig. 1.2. This semi-classical theory disentangles the HHG process into three distinct steps and provides an intuitive way to understand the HHG process within the strong field approximation. First, the electric field of a laser pulse bends the Coulomb potential of atoms in the generation medium. After some time t_0 from the maximum of the electric field, a single valence electron will have a finite chance of tunneling through the barrier into the continuum state. Secondly, the electric field of the laser will accelerate the electron away from the now ionized atom and will subsequently be accelerated back to the parent ion as the electric field (oscillating with central frequency ω_0) changes sign. Finally, when the accelerated electron is again close to the parent ion, it has a finite chance of recombining, leading to the emission of an XUV photon.

Assuming the electron at time of ionization t_0 has zero velocity, its distance from the ion as a function of time t can be calculated by solving the equation of motion and formulated as [8, 10]

$$x(t) = \frac{F_0}{\omega_0}(\cos(\omega_0 t) - \cos(\omega_0 t_0) + \sin(\omega_0 t_0)\omega_0(t - t_0)), \tag{1.3}$$

with F_0 the maximum force exerted on the electron by the electric field. In Figure 1.3, we plot several of these electron trajectories for a driving laser with wavelength of 1560 nm and t_0 ranging from 0 to 0.2 optical cycles.

Recombination can occur when the electron returns to the parent ion, i.e. $x(t > t_0) = 0$. The photon energy that is emitted upon recombination is the sum of the ionization potential of the generation medium I_p and the accumulated kinetic energy of the electron at the time of recombination. The electron trajectory with

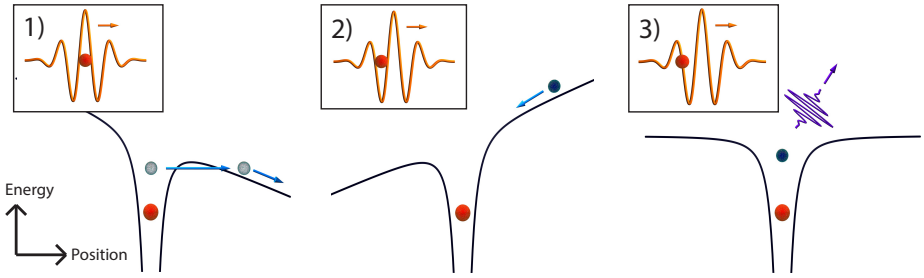

Figure 1.2: Schematic representation of the "three step model", comprising of ionization, acceleration, and recombination.

the highest accumulated kinetic energy of $3.17U_p$ is ionized at 0.05 times the fundamental cycle time. Here, $U_p = \frac{e^2 E_L^2}{4 m_e \omega_0^2}$ is the ponderomotive energy, with e the fundamental charge of the electron, E_L the electric field strength of the drive laser, and m_e the electron mass. The highest reachable photon energy, also referred to as the cutoff energy, can thus be expressed as

$$\hbar\omega = I_p + 3.17U_p. \tag{1.4}$$

Electron trajectories with earlier or later ionization times will have lower kinetic energies and thus result in lower photon energies. Consequently, there are two possible trajectories that will result in the same photon energy. Electron trajectories with later ionization times spend less time in the continuum and electron trajectories with earlier ionization times spend more time in the continuum. These two contributions are called short and long trajectories, referring to the time that the electron spends in the continuum. These two contributions to the HHG spectrum can be experimentally distinguished, as short trajectories tend to have a lower divergence compared to the long trajectories. Furthermore, the two contributions can be influenced by the addition of a secondary electric field with twice the fundamental frequency to the generation process [11], resulting in control over the phase matching between short and long trajectories and thus the divergence properties of the HHG beam [12].

A single HHG burst has a broad bandwidth, typically spanning across the XUV spectral range. Due to the coupling between photon energy and time, these pulses tend to be temporally chirped. As the HHG process can repeat itself twice per laser cycle, over multiple laser cycles, these attosecond XUV bursts will interfere, leading to the well known harmonic peak structure of odd harmonics in the spectral domain. A two-color driving field can break the symmetry between the attosecond bursts generated in the first and second half cycles of the fundamental wave, resulting in a HHG spectrum with both odd and even harmonics [11, 13–15].

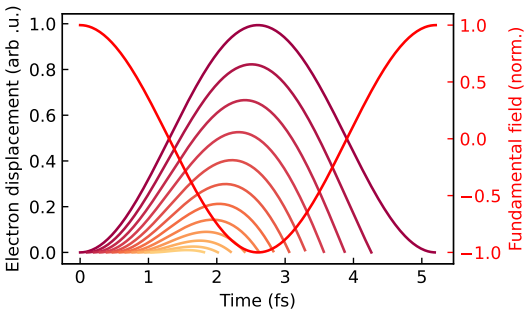

Figure 1.3: Time dependent electron trajectories driven by a 1560 nm fundamental laser field (red line). The line colors of the electron trajectories represent their different ionization times t_0, ranging from 0 to 0.22 optical cycles.

1.2.2 Phase matching

Besides microscopic effects, macroscopic effects of high-order harmonic generation also need to be considered to accurately describe the complete experiment [7, 16, 17]. As the total HHG field originates from many atoms or ions, these individual HHG field amplitude contributions need to constructively interfere to reach maximal signal strength. This condition, also referred to as phase matching, is achieved for a given harmonic order when its phase velocity is equal to that of the fundamental phase velocity. Analogous to the phase matching of low-order harmonics in the perturbative regime, when a given harmonic order q has a phase velocity not equal to the fundamental phase velocity, it will accumulate a phase mismatch Δk_q upon propagation through the nonlinear medium. This phase mismatch determines the distance across which the HHG field constructively interferes and builds up intensity, also referred to as the coherence length $L_{coh} = \pi/\Delta k_q$.

The phase mismatch between the driving fundamental frequency ω_f and a harmonic frequency ω_q consists of four contributions and can be expressed as

$$\Delta k = \Delta k_n + \Delta k_e + \Delta k_d + \phi_{Gouy}. \tag{1.5}$$

The first contribution Δk_n is the phase mismatch introduced by the dispersion of the neutral generation medium. This factor depends on the pressure and ionization fraction of the generation medium, as well as the refractive index difference within the generation medium. The second term Δk_e is the phase mismatch introduced by the free electrons present in the generation medium. The third factor Δk_d is the dipole phase, which is the phase that electrons accumulate during their propagation in the continuum in the second step of the three-step model. This phase varies for the different HHG electron trajectories and is thus dependent on the fundamental wavelength and fundamental field intensity. The final contribution ϕ_{Gouy} is the Gouy phase, which is a geometrical phase term governed by the focusing geometry. Shifting the position of the generation medium with respect to the laser focus influences the Gouy phase as well the other phases as the driving intensity also varies across the focus.

1.2.3 Laser-produced plasmas

Laser-produced plasmas (LPPs) are, as the name already describes, plasmas which are generated by the interaction of laser light with matter. When irradiating a target with a high intensity laser pulse, part of the laser pulse energy is quickly transferred into the target. With sufficient laser pulse energy, this results in the vaporization and ionization of the target, forming a plasma plume consisting of highly excited neutral particles, ions, and free electrons at the surface of the target [18–20]. An example of an aluminium plasma plume generated in our experimental setup is shown in Fig. 1.4. Such LPPs are found to be of interest for various applications, e.g. chemical vapor deposition (CVD) to form thin layers of a given target material. Another interesting application field for LPPs lies in the semiconductor industry, where extremely hot plasmas are generated when

illuminating micrometer-sized tin droplets with a pair of CO_2 laser pulses. Under the correct illumination conditions, the tin plasma starts to efficiently emit EUV photons, which is currently used as the 13.5 nm light source for the state-of-the-art nanolithography machines. In order to maximize conversion efficiency of input laser light to in-band EUV radiation while minimizing harmful ion emission, gaining fundamental insights of laser produced tin plasmas in particular has become an active field of research [21–25].

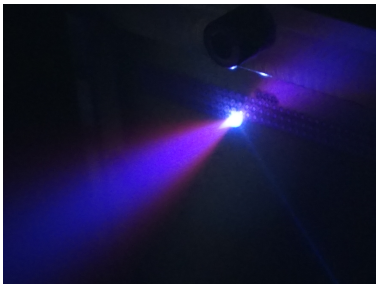

Figure 1.4: Laser-produced plasma plume generated by irradiating an aluminium target with 0.5 ns-long laser pulses. The plasma plume expands in the vacuum chamber and the highly excited atoms and ions in it emit a broad spectrum of electromagnetic radiation, also visible to the human eye.

Depending on the laser pulse wavelength and its pulse length, the interaction between the laser pulse and the target can be very different. A clear set of examples that show the differences in target morphology due to laser ablation with various pulse lengths, pulse numbers, and targets can be found in Ref. [18]. The differences in laser target interaction can in part be explained by considering a two temperature model with separate temperatures for the electrons and the lattice within the target. Such a model assumes that the laser pulse is absorbed by the electrons in the target due to inverse bremsstrahlung, heating up the electron gas. This energy can be transferred from the electrons to the lattice via electron-phonon coupling, a process that takes place in the timescale of $\tau_{e-p} \sim 10\,ps$. Femtosecond lasers with pulse lengths much shorter than this timescale directly excite the electron gas temperature within the target, resulting in a direct vaporization or plasma formation from the solid state. For longer picosecond pulses, the electron gas can transfer part of its energy to the lattice during the laser pulse, melting the target in part before it is ablated. Both femtosecond and picosecond pulses are shorter than the hydrodynamic timescale of plasma evolution, resulting in the excitation of shockwaves within the ablation target [26]. For long nanosecond pulses, the lattice heating timescale is much shorter than the pulse duration. For that reason, the electron and lattice temperatures can be considered equal. Melting of the target material and subsequent vaporization becomes a more dominant contribution for material removal as the length of the pulse increases. Furthermore, the ablation for these long pulses is less efficient due to the energy dissipation into the material. On slightly longer timescales, after creating the initial plasma during the rise time of a long nanosecond pulse,

the remaining pulse energy gets completely absorbed by the plasma at the surface of the target due to the high density of free electrons in the plasma. This plasma layer is thus heated up as long as the pulse remains active and vaporizes more material, resulting in a steady-state ablation flow. The density of the LPP depends on the laser wavelength as the critical electron density above which all laser light gets absorbed due to inverse bremsstrahlung scales as $n_{crit} \propto \lambda^{-2}$ [27–29].

1.2.4 High-order harmonic generation in laser-produced plasmas

Laser-produced plasmas can also serve as generation media for HHG, instead of the more commonly used noble gases. This approach needs a geometry with two laser pulses, where the first laser pulse (referred to in this thesis as the pump pulse) is sent onto a target to create a laser-produced plasma, and the second laser pulse (referred to in this thesis as the fundamental pulse) is, in an orthogonal direction, sent through the plasma plume initiated by the first laser pulse. With two independent laser sources and many experimental parameters to consider, generating high-order harmonics in LPPs is not trivial. The complexity of HHG in LPPs does however also come with the advantage of having many experimental degrees of freedom to optimize HHG yield. Contrary to HHG in commonly used noble gases, HHG in laser produced plasmas enables a choice many different target materials as long as they are solid and non-volatile. Many experiments have been performed in various different target materials, amongst which are Li, Na, K, B, C, Ag, and Al [30–34]. Similar to HHG in noble gases, each of these targets produces a distinct HHG spectrum, which can be useful to optimize the HHG yield in a spectral range of interest. Chapter 3 of this thesis also shows results comparing HHG spectra produced in five different target materials. Besides differences in the overall obtained HHG spectrum for various target materials, target materials with more complex atomic structures compared to the noble gases with their closed outer shells also give rise to a more complex interaction between the returning electrons in the third HHG step and the atomic or ionic wavefunction. Here, specific electron trajectories are able to recombine with an autoionizing state of the ion after which it can resonantly decay back to the ground state, instead of directly recombining to the atomic ground state [35, 36]. This newly proposed four step mechanism of HHG is expressed as a resonant enhancement of a narrowband region within the HHG spectrum. Several elements have shown such resonances at various wavelengths leading to an enhancement of single harmonic signals up to 100 times compared to neighboring harmonics [37–39]. Such a coherent quasi-monochromatic light source at XUV wavelengths could serve as an excellent tool for high-resolution metrology.

Other experimental parameters to consider for HHG in LPPs relate to the pump pulse that generates the plasma medium. The optimal laser-produced plasma for a given target in terms of greatest HHG yield can be prepared by carefully tuning the pump pulse energy, pump pulse length, pump spot size, and the delay between the pump and fundamental pulses [40]. A typical method of

reliably reproducing ideal HHG conditions in the prepared LPP is by examining the XUV spectrum that is emitted by the plasma itself, as the plasma density and temperature result in a distinct signature of spectral lines from various ion species present in the plasma [41]. Given that the coherence length of a specific harmonic is longer than the interaction length of the fundamental laser traversing the expanding LPP, a cylindrical focusing geometry for the pump pulse can be utilized to increase the interaction length and thus increases the HHG yield [42]. For harmonics with less favorable coherence lengths, quasi phase matching schemes with multiple plasma jets have been proposed [43], analogous to quasi phase matching in periodically-poled nonlinear crystals with opposite orientation of the optical axis within the nonlinear crystal. Further HHG optimization can be achieved by controlling the temporal duration of the pump pulse, for which previous studies have yielded varying results [44, 45].

Of course, HHG yield from LPPs can also be controlled by varying experimental conditions relating to the fundamental laser pulses. These parameters include the fundamental pulse energy and chirp, as well as the focus position of the fundamental beam with respect to the plasma plume. Another interesting degree of freedom is the introduction of a two-color drive field, resulting in harmonic spectra with both odd and even order harmonics [46]. Experiments with two-color drive fields have shown increased HHG efficiencies compared to single-color experiments, where enhancement factors up to 50 have been recorded for two-color drive fields with orthogonal polarizations in elongated plasma plumes compared to HHG with a single-color drive field [47–49].

Also, experimental conditions relating to the geometrical conditions need to be considered for optimal HHG yield in LPPs. As the laser-produced plasma expands in the vacuum chamber after it is generated by the pump laser, tuning the delay between the pump and probe pulses, as well as the distance between probe beam and the solid target are of vital importance for efficient harmonic generation. Typically, the pump to probe delay for optimal HHG conditions varies between several tens of nanoseconds and several hundreds of nanoseconds. Before this timescale, either the plasma has not expanded far enough to reach the interaction region, or the free electron density limits phase matching conditions. At later timescales, the plasma plume has expanded too much, such that the plasma density is too low to serve as nonlinear medium. Similarly, the distance from the fundamental beam focus to the solid target allows for probing different regions of the plasma plume, where the plasma density quickly decays as a function of distance from the target. Probing the plasma too close to the target can result in clipping of the probe beam, especially when considering the depth of focus in relation to the width of the target. This latter effect can be minimized with a cylindrical target geometry. Finally, for drive lasers with high repetition rate, the target surface quickly deforms due to the laser ablation of the pump pulse. The stability of harmonic signal during continuous operation can be maintained by scanning the target along its surface to sustain a clean ablation surface for every pump pulse [50].

The processes described above have all focused on optimizing harmonic yield by controlling experimental conditions, resulting in bright EUV spectra with gen-

eration efficiencies comparable to HHG spectra generated in gas media. High-order harmonics in the plateau region have been generated with efficiencies up to 5×10^{-5} in zinc plasmas, and harmonic orders of titanium sapphire lasers with a central wavelength around 800 nm up to order 107 have been achieved in manganese plasma plumes [42]. Instead of optimizing the HHG yield by controlling the generation conditions, producing HHG radiation in laser produced plasmas under varying plasma generation conditions might also act as a diagnostic of the laser-produced plasma. Such an approach can provide valuable information about the dynamics of laser-produced plasmas expanding in a vacuum. In particular, this might be interesting for characterization of tin plasma EUV sources for nanolithography.

1.3 Thesis outline

With all experimental parameters described above, harmonic generation in laser produced plasmas proves to be a complex phenomenon with many unexplored experimental conditions. Therefore, more experiments with a high degree of control on experimental parameters are still needed. The work described in this thesis focuses on such systematic studies on HHG in laser-produced plasmas. For this purpose, we have developed a new experimental setup for high-order harmonic generation using laser produced plasma sources as nonlinear medium. With this setup we have conducted research on various parameters relating to the two drive lasers as well as the target material.

In Chapter 2, we discuss the two laser sources that made this work possible: the fundamental laser driving the high-order harmonic generation (HHG) process, and the pump laser driving the plasma production. The femtosecond laser is an optical parametric chirped-pulse amplifier (OPCPA) operating at a central wavelength of 1.55 µm and delivering pulse energies up to 10 mJ and pulse lengths down to 180 fs at a repetition rate of 100 Hz. The pump laser is a high-energy Nd:YAG based laser amplifier with temporal shaping capabilities to tune its pulse length and shape. Pulses with durations between 0.5 ns and 1 µs can be generated by this laser system. The maximum pulse energy emitted by the pump laser system after full amplification ranges between 270 and 450 mJ, depending on the emitted pulse length.

In Chapter 3, we show the experimental setup that we have developed for generating and detecting high-order harmonics in laser-produced plasmas. This vacuum vessel consists of an experimental chamber where the plasma formation, ion detection and HHG takes place, and an EUV spectrometer which detects the generated EUV light from both the HHG as well as the plasma fluorescence. Furthermore, we report on initial measurements of HHG in various target metal plasmas to showcase their differences in HHG spectra and best generation conditions. We specifically focus on the optimization of HHG parameters for the tin plasma, as this target results in the brightest harmonic signals.

In Chapter 4, the temporal shaping capabilities of the pump laser are utilized to study the effect of plasma characteristics on the spectral distribution of the HHG.

We vary the pump pulse envelope between Gaussian and square shapes, tune the pump pulse between 0.5 ns to 50 ns, and control the delay between pump and fundamental pulses. Furthermore, we measure ion kinetic energy distributions resulting from the various ablation conditions and relate these spectra to the observed HHG signals.

Lastly, Chapter 5 introduces the concept of HHG driven by a two-color (or 2ω) field. A theoretical framework for two-color HHG with orthogonal polarizations is established. The experimental setup from Chapter 3 is extended with a type-I second-harmonic generation (SHG) setup including control over the relative phase between the fundamental beam and its second harmonic. Two-color HHG measurements with control over the relative phase between fundamental and second harmonic are presented. With these measurements, we observe oscillatory signals for both odd and even order harmonics due to the shift in relative phase. Interestingly, the observed high-order harmonics oscillate out of phase from each other, indicating the relevance of the atomic structure in the HHG process.

Chapter 2

Laser systems and experimental setups for laser-produced plasma studies

Abstract

We present an optical parametric chirped pulse amplifier (OPCPA) delivering 10.5 mJ pulses with durations down to 220 fs, at 100 Hz repetition rate, centered at 1550 nm. The system is pumped by a picosecond Nd:YAG amplifier at 1064 nm based on quasi-continuous-wave diode pumping, and seeded by a femtosecond mode-locked Er fiber laser at 1550 nm. This choice of wavelengths enables the use of well established technology and optical components for both pump and signal beams, resulting in a straightforward and robust system design and the ability for further power scaling to be used in high energy laser-produced plasma experiments. We also describe the sub-nanosecond (SNS) laser system at 1064 nm which closely resembles the pump laser of the OPCPA system. The intensity of its CW seed laser can be temporally modulated with a resolution of 0.43 ns up to maximal durations of 1 µs. The temporal gain dynamics in the subsequent amplifiers are pre-compensated to achieve the desired pulse shape after full amplification. The maximum pulse energy of the SNS depends on the amplified pulse shape and ranges between 270 and 450 mJ at a repetition frequency of 100 Hz.

Sections 2.1, 2.2, and 2.4 of this chapter are based on [51].

2.1 Laser requirements

The state of the art extreme ultraviolet (EUV) sources for nanolithography use high-energy lasers which are focused on liquid microdroplets of tin inside a vacuum chamber, creating a laser-produced plasma (LPP) that emits 13.5 nm light [52]. Key plasma characteristics such as the temperature and density are heavily influenced by the input laser parameters [53–55]. These characteristics will in turn govern more practical effects such as the EUV emission spectrum and power, and the energy distribution of emitted ions. A great deal of insight on laser-plasma interaction can be obtained by studying the emission of photons and ions from LPPs for different input laser parameters [56–59].

To study such laser-plasma interactions, we built a high-energy Nd:YAG system with tunable pulse duration in the picosecond range and showed that laser parameters play a key role in the deformation of the microdroplets [60, 61] and in the energy distribution of the ions emitted by the laser-produced plasma [62, 63]. We now aim to extend these studies by using femtosecond pulses to probe beyond electron-phonon interaction timescales, and study ion emission for the case where all the laser energy is deposited before ion dynamics take place. The pulse energies required for laser-plasma interaction studies are typically in the 10 mJ range and above. To generate femtosecond pulses with such high energy, we designed an optical parametric chirped-pulse amplifier (OPCPA) using the ps Nd:YAG amplifier mentioned above as the pump beam, and a commercial ultrashort fiber oscillator-amplifier system at 1.55 µm wavelength as the seed source.

Compared to 532 nm pumped OPCPA systems [64–70], direct pumping with 1064 nm offers a higher pump energy, and it yields a very useful 3.5 µm idler beam when the system is seeded at 1.55 µm. While this work focuses on the amplification of the 1.55 µm seed beam, there is a great deal of interest and work done in femtosecond sources in the mid-IR [71–73]. However, phase-matching schemes in available crystals are less optimal for ultra-broadband amplification, compared to systems pumped by frequency-doubled Nd:YAG at 532 nm and seeded by Ti:sapphire lasers. To circumvent this limitation, prior authors have used quasi-phase matching in periodically (and also aperiodically) -poled Lithium Niobate (PPLN) [71, 74–76]. However, due to the limited power handling capabilities of PPLN, pulse energies are typically limited to tens of µJ. KTA- and KTP-based optical parametric amplifiers (OPAs) have been used to produce mJ-level 1.5 µm and 3.5 µm pulses [72, 77, 78]. However, the broadest phase-matching bandwidth for 1064 nm pumping is centered at 1470 nm, where direct seed generation is challenging due to the absence of broadband laser gain media, and additional nonlinear conversion steps are required [72]. Another configuration for ultrashort pulse generation near 1.5 µm is to change the pump wavelength to the Ti:sapphire range, enabling a white-light-seeded OPA working near degeneracy [79].

When choosing the seed wavelength at 1550 nm (telecom wavelength), fs sources and efficient optics are readily available [80]. This leads to a choice between more involved seeding schemes that produce shorter pulses or a more straightforward approach based on commercial components for higher efficiency and less complexity. Because LPP applications often have more stringent de-

mands on pulse energy and stability rather than pulse duration, in this work we explore the latter option.

2.2 Laser source

In this section, we describe in detail the pump beam generation as well as the OPCPA system. The pump laser system consists of an Nd:YVO_4 oscillator and pre-amplifier, followed by a Nd:YAG power amplifier. The amplification stages are based on two separate systems [81, 82]. The OPCPA is 3-stage system using KTA crystals, where the first two stages have a non-collinear geometry, while the last stage is collinear to avoid generating a spatially dispersed idler beam.

2.2.1 Picosecond pump laser system

The pump laser system is seeded by a home-built Nd:YVO_4 master oscillator, operating at a wavelength of 1064 nm. The crystal is end-pumped by a fiber-coupled diode array which emits 18 W of continuous-wave (CW) radiation at 880 nm [83, 84]. Mode-locking is achieved with a saturable-absorption mirror, resulting in 50 nJ, 7 ps pulses at a repetition rate of 100 MHz. To enable amplification of these pump pulses to the $>$ 100 mJ level while avoiding optical damage, a slightly longer pulse duration is preferred. Therefore a pulse duration adjustment system was implemented. In this system (Fig. 2.1), the beam passes through a grating in a 4-f system with an adjustable slit placed in the Fourier plane, where the spectral content is spatially separated. By adjusting the opening of the slit, the spectrum of the laser is clipped, resulting in a tunable pulse duration up to 120 ps. For OPA pumping, the pulse duration is set to 100 ps. The downside of wavelength selection to achieve longer pulses is the lower seed power available for subsequent amplifier stages. However, this is not a limitation as the pulse energy needs to be reduced to 0.75 nJ with a waveplate and thin-film polarizer (TFP) due to power limitations of the pulse-picking system that follows next.

The spectrally-clipped 100 ps pulses are coupled to a fiber-based pulse picking scheme comprising an acousto-optical modulator (AOM) and an electro-optical modulator (EOM). The AOM (Gooch & Housego Fiber-Q) has a high contrast of 50 dB and can withstand the average power of the oscillator at the full repetition rate, but its 30 ns rise time is not sufficient to select single pulses from the 100 MHz pulse train. We therefore use it to time gate a 400 ns window, containing 40 consecutive pulses, at a 100 Hz repetition rate. The subsequent EOM (Jenoptik AM 1064) has a specified rise time of 0.25 ns with a lower contrast of 30 dB, and is controlled by an arbitrary waveform generator. The EOM can pick, from the lower average power burst after the AOM, any number of isolated pulses. In normal operation for OPA pumping, a single pulse is picked. This pulse picking assembly combines the high contrast of the AOM with the speed and flexibility of the EOM. For the present OPCPA pumping application it is mainly used to reduce the repetition rate to 100 Hz, but it can also be used

for more advanced schemes, such as pulse trains with adjustable time delays (in increments of 10 ns) between each pulse [62].

After the pulse picking, the pulses are first amplified by two grazing-incidence "bounce" pre-amplifier stages. The system comprises two Nd:YVO_4 crystals, doped at 1% and 0.5%, and with dimensions of 5 × 2 × 20 mm and 6 × 4 × 20 mm, for the first and second crystals, respectively. The design of this bounce amplifier closely follows the concept presented by Morgenweg et al. [81]. As shown in Fig.2.1, the crystals are pumped from the side by quasi-continuous-wave (QCW) pulsed laser diodes (DILAS MY-series) tuned to 880 nm through temperature control. These QCW diodes provide high pump fluence for 120 µs (slightly longer than the upper state lifetime of Nd:YVO_4) at a repetition rate of 100 Hz, resulting in a high gain with negligible thermal effects on the crystal or beam propagation. The significant doping level combined with strong single-sided pumping creates a region of very high gain confined close to the pumping surface. The beam travels through this high-gain region at an angle, and is aligned such that it undergoes a total internal reflection at the center of the pumped surface. This reflection averages away the inhomogeneity caused by the side-pumping geometry. Without this reflection, the beam would experience higher gain closer to the pumped crystal surface, leading to an uneven amplified beam profile.

The first crystal is traversed twice, using an optical isolator in between the passes to avoid parasitic lasing. After this double pass the pulse energy reaches 180 µJ. With an input energy of 120 pJ, that amounts to an average gain per pass exceeding 10^3. A consequence of the high gain is a significant amount of amplified fluorescence in addition to the amplified seed pulse. To improve pulse contrast before the second bounce amplifier stage, the amplified beam is focused through a 200 µm pinhole. Since the amplified beam and the fluorescence have a slightly different divergence and beam shape, this spatial filter can be set up such that the amplified pulse is transmitted more efficiently than the fluorescence background. After a single pass through the second crystal, we achieve a pulse energy of 1.4 mJ, which is sufficient to effectively seed a power amplifier based on large-aperture Nd:YAG rods. For optimum stability, the EOM selects a pulse from the center of the pulse train transmitted by the AOM, which results in a series of pre-pulses at 0.1% peak energy transmitted into the amplifier. In addition, after amplification we observe 0.6 mJ fluorescence in a 120 µs time window.

To prevent these parasitic pulses and most of the amplified fluorescence from the pre-amplifier from reaching the power-amplifier and extracting gain, two Pockels cells (PCs) and polarizers are placed between the pre- and power-amplifier stages. These PCs have rise and fall times of 5 ns, sufficiently fast to pick a single pulse, with a contrast greater than 2000:1, experimentally verified with a fast photodiode. An optical isolator is used as the last polarizer of this assembly, to protect the preceding systems against amplified back-reflections from the power-amplifier.

The power-amplifier comprises two Nd:YAG amplification modules (Northrop Grumman REA6308 and REA10008), which are both employed in a double-pass configuration [82]. These modules contain 146-mm-long cylindrical Nd:YAG

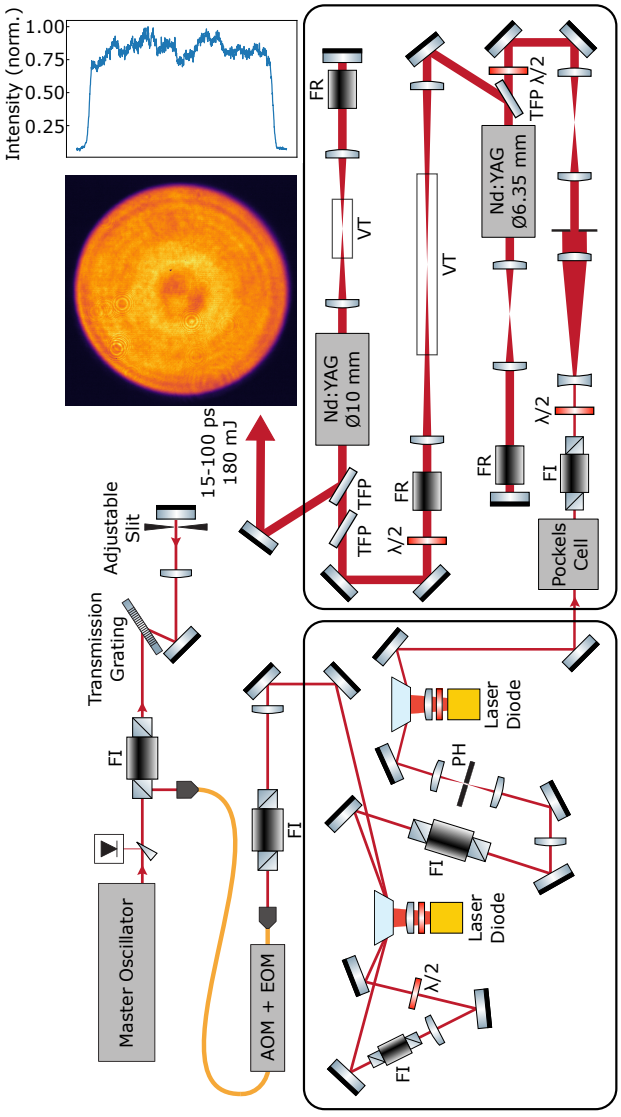

Figure 2.1: Schematic of the 1064 nm pump source, consisting of the oscillator and spectral clipping system, the bounce pre-amplifier and the power amplifier units. The final output beam profile is shown on the top right, imaged from the second YAG module to a CCD camera. FR: Faraday rotator; FI: Faraday isolator; PH: 200 µm pinhole; TFP: Thin-film polarizer; VT: Vacuum tube; $\lambda/2$: Half-wave plate

rods with 6.35 and 10 mm diameter, respectively. The rods are transversely pumped by QCW diodes arranged in a five-fold symmetry. Especially in this amplifier stage, the QCW pumping enables high gain and stored energy while keeping thermal effects at a manageable level. For effective OPCPA pumping it is beneficial to have a flat-top spatial beam profile after the power amplifier. To this end, the Gaussian beam from the pre-amplifier is expanded to 12 mm ($1/e^2$-diameter) and passes through a 2 mm diameter aperture. The beam profile at the aperture plane is relay imaged in the center of the first Nd:YAG module. This first module has a diameter of 6.35 mm and is under-filled by a 5.4 mm beam. Although more energy can be extracted by using a larger beam inside the rod, we found that this results in the five-fold pattern of the pump geometry being imprinted on the outer edges of the beam.

To mitigate the effects of thermally-induced lensing and birefringence, a double-pass amplifier configuration is utilized [82, 85, 86]. The plane inside the rod at which the aperture is imaged, is subsequently relay-imaged by a telescope with unit magnification, onto a mirror which reflects the beam back for the second pass through the rod. A Faraday rotator placed close to this end mirror rotates the polarization of the beam by 90° after a double pass. This combination of spatial imaging and polarization rotation results in a compensation of the thermally-induced birefringence in the Nd:YAG rod [86]. After the double-pass, the resulting polarization is linear and rotated over 90° with respect to the incident beam, allowing convenient beam extraction with a TFP.

The image plane in the first amplifier rod is then relay-imaged in the center of the second module, using a telescope that expands the beam diameter to 8.6 mm. A Faraday rotator is placed in this telescope between the modules, which in combination with the TFPs optically isolates the passes to prevent self-lasing and damage from high-energy back-reflections. To prevent optical breakdown in air, a vacuum tube is placed at the focus of each imaging telescope after the first double-pass amplifier. Similar to the first module, the beam from the first pass through the 10 mm diameter Nd:YAG module is imaged onto a mirror and back-reflected for a second pass, with a 90° rotated polarization.

The wavelength of the pump diodes can be controlled through temperature tuning, enabling adjustment of the overlap with the Nd:YAG absorption band. Optimization of the pump wavelength leads to a higher energy output, but also results in a stronger absorption with a shorter absorption length close to the outer diameter of the rods, and therefore a spatial gain profile that peaks towards the rod edges. As a result, temperature tuning of the pump diodes also enables some control over the output beam profile, and we exploit this feature to optimize the flat-top profile at the end of the amplifier chain. The resulting beam profile is depicted as an inset to Fig. 2.1. We operate the modules at 240 V for 235 microseconds at a peak current of 70 A and 85 A to reach gain saturation for the first and second module, respectively. For optimal beam profile the temperatures are set to 21.5 °C and 20 °C, respectively. The final amplified output energy is 180 mJ, for a pulse duration of 100 ps. This energy level is intensity-limited, determined by the damage threshold of the optical coatings on the Nd:YAG rods and other components. At longer pulse durations, higher pulse energy can

readily be extracted from the amplifier. The output energy can also be scaled further by utilizing amplifier rods with a larger diameter, allowing for larger beam diameters.

2.2.2 Ultrafast optical parametric chirped pulse amplifier at 1.5 µm

The OPA is seeded by a commercial Erbium-doped fiber laser (C-Fiber Sync High Power by Menlo Systems), which delivers 3 nJ, 90 fs pulses at 100 MHz repetition rate. The laser is equipped with a fast response piezo-mounted cavity mirror, which is used to synchronize the laser repetition frequency to that of the oscillator in the pump system. For this purpose, the repetition rates of both oscillators are monitored using fast photodiodes (EOT-3500, 12.5 GHz bandwidth). The photodiode outputs are fed into a 1.5 GHz-bandwidth frequency mixer to produce a difference frequency beat signal, which is then used as input for a PID loop which actuates the piezo. As the difference frequency is sensitive to the relative phase between the two repetition rate signals, the relative time delay between the two laser pulse trains remains fixed each time the loop is closed. This locking scheme typically achieves timing synchronization at the 1 ps level. In addition to the piezo-mirror, the laser oscillator is also equipped with a stepper motor with a larger operating range, which enables coarse compensation of longer-term drifts and day-to-day differences in lab conditions.

The femtosecond pulses are stretched with positive group-velocity dispersion to a duration of around 30 ps in a Martinez-type 4-f grating system. The stretcher contains two equal 940 lines/mm transmission dielectric gratings with a manufacturer-specified diffraction efficiency of 95%, and the total device has an overall measured efficiency of 83%.

A schematic of the OPA layout is shown in Fig. 2.2. The OPA consists of three single-passed 10 mm long, $\theta = 42.5^\circ$ KTA crystals (Castech Inc.). The first two passes are set up in a noncollinear geometry, with noncollinear angles of 2° and 1.5°, respectively. This geometry enables the pump and idler beams from the first two passes to be easily separated from the amplified signal beam. The noncollinear geometry also has a slightly broader gain bandwidth (Fig. 2.3, green trace). The pump beam is *s*-polarized, while the seed beam is *p*-polarized, for all three stages.

The pump beam is imaged on the first and second crystals, resulting in smooth flat-top spatial profiles with diameters of 1.7 mm and 1.9 mm, respectively. The seed beam has a $1/e^2$ diameter of 1.3 mm in both crystals. Both stages are pumped at 22.5 mJ and the seed is amplified to 1.4 mJ after the first two stages.

The third OPA stage is set up in a collinear geometry. While this results in a reduced gain bandwidth (Fig. 2.3, blue trace), it has the benefit of producing an idler beam that is not spatially dispersed so that it can be used in future experiments. The pump and seed beams have diameters of 4.0 mm and 3.4 mm ($1/e^2$), respectively. The last stage is pumped by up to 135 mJ and produces up to 12.5 mJ of uncompressed 1550 nm pulses. Fluorescence at the signal wavelength was characterized by blocking the seed to the first OPA stage while pumping all

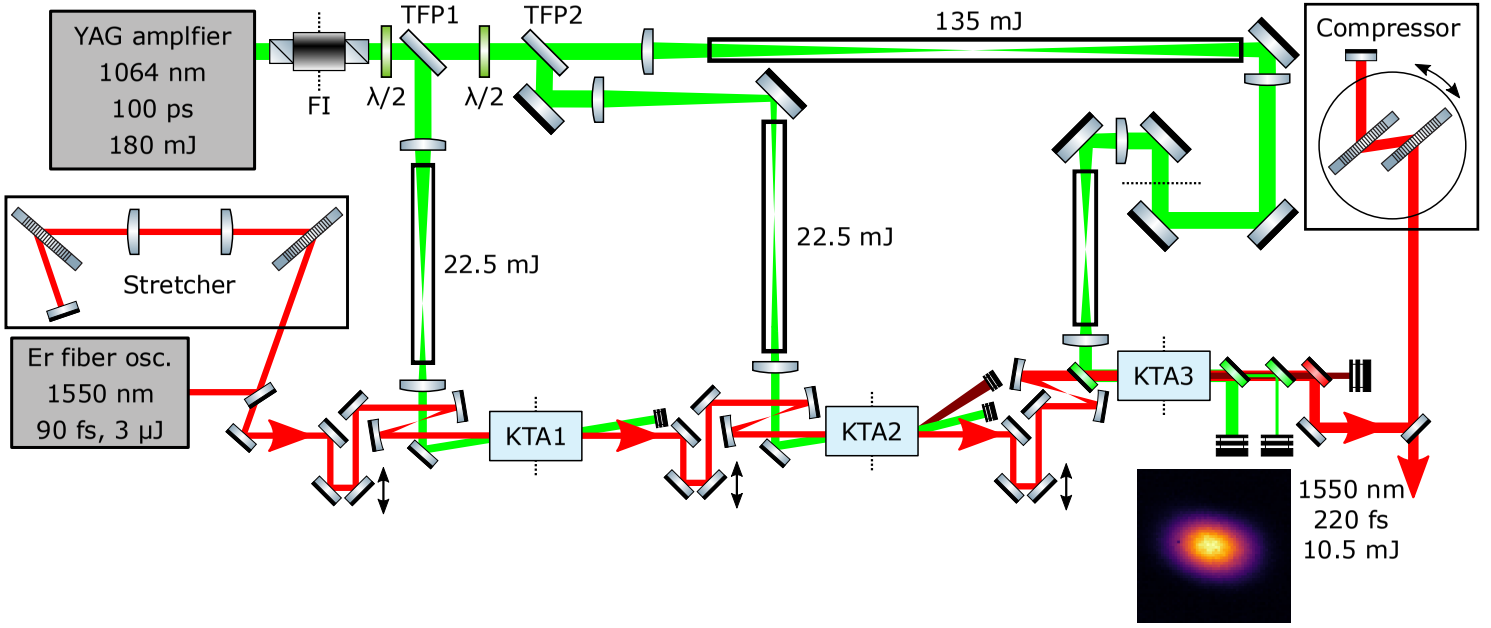

Figure 2.2: A detailed schematic of the OPCPA system. The dotted lines are points where the flat-top beam profile of the pump beam is imaged. On the bottom right we show the signal output of the OPCPA, focused by a 50 mm convex lens to a 75 µm spot ($1/e^2$-diameter). The same acronyms as in Fig. 2.1 are used.

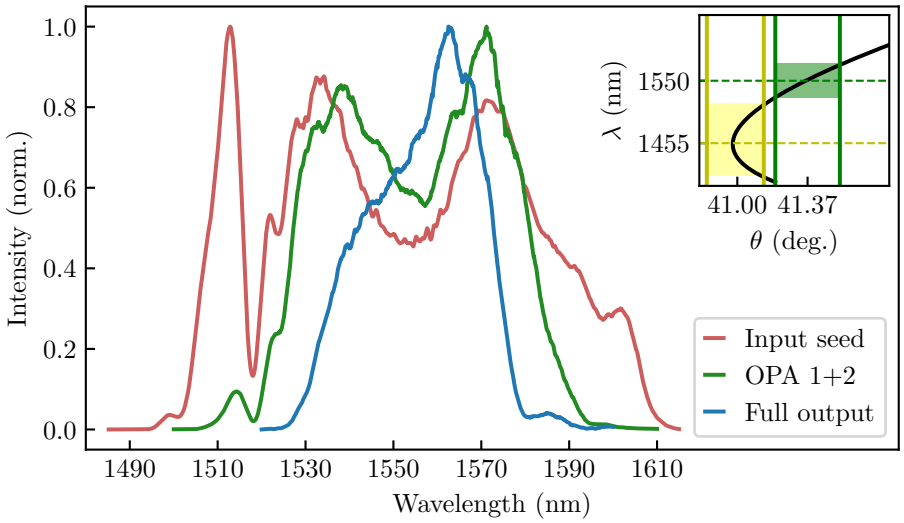

Figure 2.3: Spectra at various stages in the OPCPA system. The inset shows the phase-matching curve for KTA with 1064 nm pumping. The shaded areas highlight the phase-matching bandwidths for a 0.15° acceptance angle, centered at 1455 nm (yellow) and 1550 nm (green). λ: wavelength; θ: phase-matching angle.

stages at full power. In this configuration, the fluorescence energy remains below the mW-level detection limit of the power meter.

After the final crystal, there is a significant imprint of the pump spatial profile onto the signal beam, resulting in a flat-top-Gaussian mix that diffracts as it propagates. Nevertheless, the beam can be focused into a smooth Gaussian-like profile with a $1/e^2$-diameter of 75 µm by a plano-convex lens, as shown in the inset of Fig. 2.2.

To separate the outgoing beams, we use a set of custom-designed dielectric dichroic mirrors (Layertec). The first of these mirrors reflects the pump beam while transmitting both signal and idler, and afterwards signal and idler are separated with another dichroic mirror. In practice, two pump-separating mirrors are used to remove the pump radiation from the amplified signal beam with sufficient contrast.

The amplified signal pulses are compressed by a pair of gratings identical to those in the stretcher. Using transmission gratings enables us to use an efficient Littrow configuration in the compressor, and have a compact layout that can be conveniently mounted on a rotation stage for fine-tuning the compression [65], as the input angle provides control over the ratio between second- and third-order dispersion. Like the stretcher, the compressor boasts a high efficiency of 85%, resulting in compressed pulses of 10.5 mJ. Over timescales of minutes, an energy stability of 1.5% rms was typically measured.

2.2.3 Pulse characterization

As shown in Fig. 2.3, after two stages, the amplified spectrum is narrower than the initial seed spectrum. This is due to the limited phase matching bandwidth. The effect is further exacerbated after the third stage, due to the collinear geometry. To characterize the resulting pulse duration after the full amplifier system, we use a second-harmonic-generation frequency-resolved optical gating (SHG-FROG) device containing a 200 µm thick BBO crystal into which we send a small fraction of the amplified output beam. The measured and reconstructed SHG-FROG traces are shown in Fig. 2.4, along with the retrieved pulse shape. The Fourier-transform (FT) limited pulse durations corresponding to the input seed and amplified output spectra are also displayed for comparison. We find that the gain bandwidth in the collinear geometry increases the FT-limited pulse duration from 73 fs at the input of the OPA to 158 fs after all three crystals. The actual duration of the compressed pulse was measured to be 220 fs, as shown in Fig. 2.4. The discrepancy with the FT-limit likely comes from uncompensated residual higher-order dispersion, or possibly spectrally dependent gain saturation effects [87]. If a spatially dispersed idler is not an issue, then one could take a noncollinear geometry for the third OPA stage, and achieve a broader bandwidth and a subsequent reduction of the achievable pulse duration.

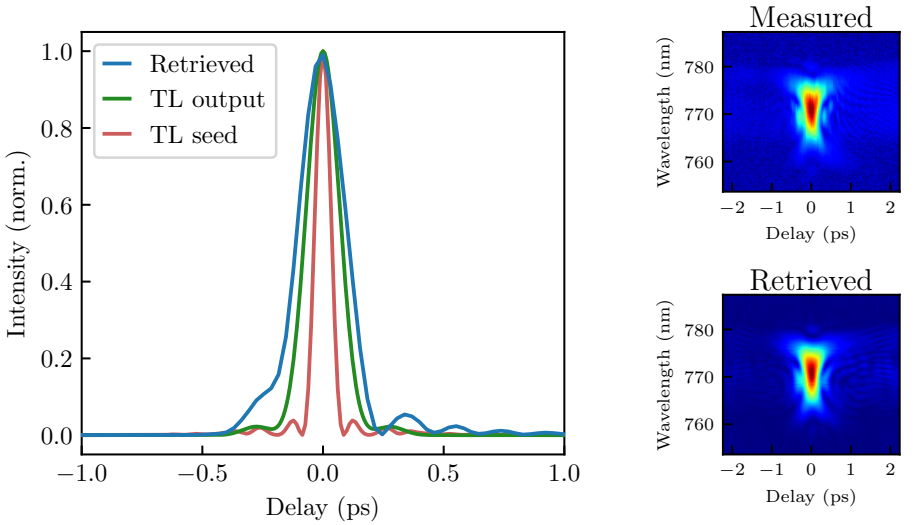

Figure 2.4: Pulse characterization of the OPCPA output at full amplification, using SHG-FROG. Transform limited pulses were calculated from the spectra shown in Fig. 2.3.

2.3 Sub-nanosecond laser system for generating laser-produced plasmas

In this section, we describe the sub-nanosecond (SNS) laser system, which was developed previously [88] and is used in the present work for generating the laser-produced plasmas in our experimental setup [89]. For the high-order harmonic generation in laser-produced plasma experiments, the SNS laser is externally triggered by the picosecond pump laser system described above, allowing for electronic control of the delay between pump and fundamental pulses without using a delay line. A detailed schematic of the SNS laser system is shown in figure 2.5. It comprises a fully fiber based CW seed laser with pulse shaping capabilities, a Nd:YVO_4 grazing incidence "bounce" pre-amplifier, and a Nd:YAG power amplifier. The seed laser is a commercial CW fiber laser (NKT Koheras BoostiK Y10) delivering 2 W at a wavelength of 1064 nm. The arbitrary pulse shaping capability of this laser system is achieved by modulating the intensity of this seed laser by means of an AOM and two EOMs. It is capable of generating pulses with lengths up to 1 microsecond with a resolution of 0.43 ns, depending on experimental requirements. The AOM (Gooch and Housego Fiber-Q) modulates the CW laser into square pulses with a contrast of 50 dB at a repetition rate of 100 Hz to generate the initial pulse train. Subsequently, two EOMs (Jenoptik AM 1064) further modulate the pulse intensity to the desired pulse shape to be amplified. These EOMs are individually driven by a 2.3 Gs/s dual-channel arbitrary wavefront generator (Tabor Electronics WX2182C). Changes in the pulse shape due to gain dynamics of the subsequent two amplification stages are compensated for in this initial pre-shaping setup. Together, the pulse shaping AOM and EOMs are specified to have a 12 dB insertion loss. This, together with a given, specific pulse shape, can be used to estimate an upper limit on the seed pulse energy. The pulse energy of a Gaussian 0.5 ns (FWHM) seed pulse is estimated to have an energy of 30 pJ and a 500 ns square-shaped pulse is estimated to have an energy of 63 nJ.

The grazing incidence bounce amplification stage is nearly identical to the bounce amplification system for the picosecond OPCPA pump laser described above. It also comprises of two Nd:YVO_4 crystals, doped at 1% and 0.5%, and with dimensions of 5 × 2 × 20 mm and 6 × 4 × 20 mm, for the first and second crystals, respectively. These crystals are pumped from the side by QCW laser diode arrays emitting roughly 240 W at 880 nm during 110-microsecond-long pulses. The first crystal is passed twice, with an optical isolator between the two passes to prevent backreflections, parasitic amplified spontanious emission in the direction opposite to the seed laser propagation, and self-lasing of the amplifier. After the first crystal, another optical isolator as well as a spatial filter are placed in the beam path to further suppress parasitic ASE contributions and to eliminate hazardous back reflections and self-lasing. After passing the second bounce crystal, the seed pulses are amplified up to 2.84 mJ, depending on the pulse length of the seed beam.

Between the Nd:YVO_4 bounce amplifier and the Nd:YAG power amplifier, a Pockels cell in combination with two optical isolators temporally gates the ampli-

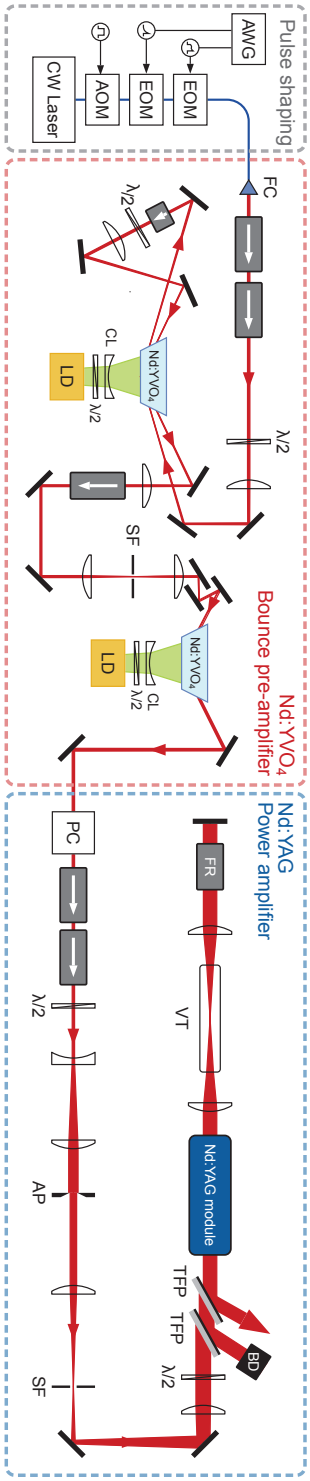

Figure 2.5: A detailed schematic of the SNS laser system, comprising a fiber-based pulse shaping section, a Nd:YVO_4 bounce pre-amplifier and a Nd:YAG power-amplifier. The same acronyms as in Fig. 2.1 are used.

fied pulses from the bounce amplifier and further reduces the bounce ASE outside of the temporal window of the main pulse, preventing gain loss in the power-amplifier. After the PC, the beam is expanded to a e^{-2} diameter of 3.05 mm, after which it gets clipped by a hard aperture with a diameter of 2.4 mm. This truncated Gaussian beam is relay imaged with 2 times magnification onto the Nd:YAG power amplifier module (Northrop Grumman REA6308, identical to the first power amplifier module of the picosecond pump system). A weak spatial filter is positioned at the focus of this relay telescope to smoothen the hard edges of the aperture in consecutive image planes. This Nd:YAG module is also employed in a double pass configuration. After the first pass, the beam is relay imaged without magnification onto a backreflection mirror. A vacuum tube with anti-reflection coated windows on either end is placed around the focus of the relay imaging telescope to prevent breakdown in air. A Faraday rotator, also passed twice, rotates the polarization by 90 degrees, which counteracts the thermally-induced birefringence of the Nd:YAG rod and allows for extraction of the amplified beam with a TFP. An additional TFP dumps any residual leakage of the first TFP to reduce the chance of self-lasing. The extracted amplified beam is again relay-imaged onto an optical isolator to protect the amplifier from hazardous back reflections. The pulse energy emitted by the system after full amplification ranges between 270 and 450 mJ, depending on the emitted pulse length.

A small energy fraction up to 20 mJ of this amplified beam is guided to the experiment. A final relay imaging telescope reduces the beam size after the optical isolator to 5 mm, after which it is freely propagated to the experimental setup described in Chapter 3.

2.4 Conclusion

We have described an OPCPA delivering 220 fs pulses with 10.5 mJ of energy at 1550 nm center wavelength, at a repetition rate of 100 Hz. The pump laser for it delivers 100 ps pulses with 180 mJ of energy at 1064 nm wavelength. In the system design, robust and direct pump and seed sources were chosen. Even though these choices limited the minimum achievable pulse duration, the achieved performance satisfies the needs for high-field and laser-driven plasma experiments at ultrafast timescales. In addition, the use of robust laser technology at these standard wavelengths enables a straightforward and reliable seeding scheme, and significant further power scaling capabilities and flexibility for plasma experiments due to the stand-alone pump source. Furthermore, the use of direct laser seeding provides a relatively high seed intensity, which is an important advantage for achieving high pulse contrast and low fluorescence background [65, 66].

In addition, we have presented a description of the SNS laser system which acts acts as the pump beam that generates the laser-produced plasmas in which the high-order harmonic radiation is produced. This laser delivers pulses with variable lengths in the range of 0.5 ns to 1 microsecond with pulse energies ranging between 270 and 450 mJ, depending on the selected pulse shape.

Chapter 3

Material-specific high-order harmonic generation in laser-produced plasmas for varying plasma dynamics

Abstract

We present a new experimental setup for high-order harmonic generation in laser-produced plasmas, allowing the generation of coherent VUV and EUV light, as well as characterization of the laser-produced plasmas by studying the emitted harmonics. We have successfully generated high-order harmonics in laser-produced Al, Ni, Ag, In, and Sn plasmas. Large differences in harmonic spectra and signal yields have been observed for these different targets. Harmonics up to order 25, corresponding to a wavelength of 62.4 nm and photon energy of 19.9 eV, have been measured with tin plasmas. Scanning laser parameters and delay between pump and fundamental laser pulses allows us to optimize the harmonic yield and observe the temporal dynamics of the laser-produced tin plasma.

This chapter has been published as [89].

3.1 Introduction

Next-generation nanolithography devices make use of extreme ultraviolet (EUV) radiation, emitted by a laser-produced plasma (LPP) in tin, to print nanometer-sized features on semiconductor wafers. Such LPPs are created by illuminating a target with intense laser radiation that ablates part of the target surface and forms a plasma. The properties of such LPPs are heavily dependent on the incident laser parameters. Additionally, the EUV radiation which is emitted by this plasma strongly depends on the plasma properties. A thorough understanding of the plasma dynamics and its influence on optical emission is therefore an important subject of study.

Many efforts have been spent in understanding the fundamental physics of EUV emission from tin LPPs, as well as the laser-matter interaction leading to the deformation of micrometer-sized tin droplets to more suitable EUV source targets [90–92]. The UV and EUV emission spectra of tin LPPs generated by lasers of various wavelengths have been measured to optimize the spectral purity and conversion efficiency of laser light to in-band EUV radiation [23, 24, 93]. Ion and debris studies have also been carried out to gain fundamental knowledge on the plasma conditions in the LPP EUV source, and to extend the industrial lifetime of collector optics close to the LPP [25, 94, 95].

High-order harmonic generation (HHG) in the LPP by an auxiliary femtosecond laser may serve as a new method to gain time-resolved information from the LPP expanding in the vacuum, since the nonlinear HHG process is highly sensitive to variations in plasma density. The highest achievable photon energy in the single atom response of HHG is given by the cutoff energy $E_C = 3.17 \cdot U_P + I_P$, where $U_P = 9.33738 \cdot 10^{-5} \cdot I[\mathrm{PW/cm^2}] \cdot \lambda^2[\mathrm{nm}]$ is the ponderomotive energy of the electrons in the drive laser field with intensity I and central wavelength λ, and I_P is the ionization potential of the generation medium. The cutoff energy scales with the ionization potential I_P, meaning that HHG spectra are also sensitive to the different ionic charge states in the LPP.

The concept of generating high-order harmonics (HHs) in LPPs started in 1992 by generating HHG in rare-gas like ions with high ionization potentials to increase the cutoff energy [30]. Although these initial experiments did not lead to an increase of the cutoff energy due to mismatches in the phase between driving laser and its harmonics as well as defocusing effects caused by the presence of free electrons, large progress in terms of HH yield and extending the cut-off energy has been made in the field of LPP-based HHG since then. Many elements have served as targets to generate HHs in LPPs with various yields in HH strength and spectra [31–34]. The highest-order harmonic generated in Mn LPPs from a secondary plateau region was H107 and high conversion efficiencies up to $5 \cdot 10^{-5}$ for the 11^{th}-19^{th} harmonics have been achieved in Zn LPPs [42]. Additionally, contrary to HHG in noble gases, the resonant enhancement of single HHs, where the strength of a single HH in the plateau region is enhanced up to two orders of magnitude compared to its neighboring HHs, has been observed in plasma HHG [36–38]. Such resonantly enhanced HHs with high flux and narrow bandwidth have great potential for diffraction-based experiments such as coherent diffractive

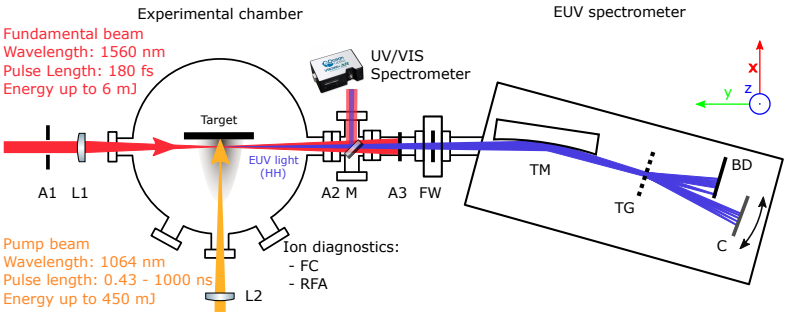

Figure 3.1: A schematic of the vacuum setup, consisting of an interaction chamber where the plasma and high-order harmonics are generated, and an EUV spectrometer to analyze the high-order harmonics. A: Aperture, L1: f = 300 mm lens, L2: f = 1000 mm lens, M: Insertable Mirror, FW: Filter wheel, FC: Faraday cup, RFA: Retarding field energy analyzer, TM: Toroidal mirror, TG: Transmission grating, BD: Beam dump, C: EUV camera.

imaging.

Although significant progress has been made in this field, experiments that focus on the influence of plasma composition on HHG have remained scarce. For this purpose, HHG experiments in more controlled LPPs with control over the plasma density and ionization degree are needed. In this work, we present a new setup that allows systematic studies of the spatial and temporal properties of controlled LPPs from various targets. Conversely, this setup is capable of controlling the plasma formation in order to maximize the harmonic yield for various different targets. We present bright HHG in various LPPs and showcase the impact of changing plasma generation laser parameters on the HHG spectra. Firstly, we give a full description of the experimental setup. Secondly, the results for HHG in various LPPs, as well as the dynamics of HHG in tin plasmas are presented, followed by the discussion, outlook, and a conclusion.

3.2 Experimental setup for plasma-based high-order harmonic generation

The experimental setup for the generation and detection of HHG in LPPs consists of two major components, being the interaction chamber and the EUV spectrometer. A schematic of the vacuum system is shown in Figure 3.1.

In the center of the interaction chamber, a solid metal target is mounted on a 4-dimensional translation stage (XYZR). The pump beam that creates the plasma is a high-energy Nd:YAG laser system with arbitrary sub-nanosecond pulse shaping capability [88]. This laser system outputs pulses with a flattop beam profile, a central wavelength of 1064 nm, pulses up to 1 µs duration with a shaping resolution of 0.43 ns and pulse energy up to 450 mJ at a repetition rate of 100 Hz. It is loosely focused to a spot size of 450 µm (e^{-2} diameter) on the

target. For most of the experiments, the shortest possible pulse length of 430 ps is used to generate the LPP. In this case, the pump energy E_p is varied between 0.5 and 20 mJ, depending on the target. Longer 60 ns pulses were also used to create quasi-static LPPs where the plasma charge state composition could be tuned by varying the laser energy. In this latter case, similar pump energies of 5 mJ and 10 mJ were sent on the target to generate the plasma.

The solid target in the center of the interaction chamber is partially ablated with every pump pulse, leaving a crater at the surface of the target. When this crater becomes too deep, the laser-target interaction geometry changes resulting in a plasma that is less suitable for generating HHs as has been previously observed by Hutchison et al. [50]. Therefore, the target is translated in the horizontal and vertical (Y and Z) direction to a fresh spot after every burst of 157 pump pulses. The EUV camera then acquires the HHG signal from the final 150 shots as the first seven pump pulses remove the native oxide layer from the target surface. Besides the crater formation process, debris from the plasma is slowly coating the outside walls of the vacuum chamber. This debris takes up to a few milliseconds to fully expand into the vacuum chamber, well before the next pulse arrives in the experiment. Part of the LPP debris ends up at the pump laser viewport, although we find that the high-intensity laser pulses drive a self-cleaning process, causing every consecutive laser pulse to remove most debris from the viewport again.

Additionally, the distance between the target and the fundamental beam can be varied by translating the target in the X direction up to 2 mm. As this translation is much smaller compared to the focal length of 1000 mm, the effect on the generated plasma is negligible. Together with the delay between the pump and fundamental pulses, this allows us to probe the expanding plasma plume both spatially and temporally.

3.2.1 Ion diagnostics

To get an indication of the ion charge states that are present in the plasma, a Faraday cup (FC) and a retarding field energy analyzer (RFA) are mounted on the experimental chamber at a small 9° angle with respect to the pump beam. The FC measures ion time-of-flight (TOF) currents, but is insensitive to specific charge states. In combination with the distance between the target and the FC, the kinetic energy distribution of the ions can be obtained from these TOF measurements. Similar to the FC, the RFA also measures ion TOF currents, although it discriminates ions with $E_{kin}/z < U_{Ret}$ where E_{kin} is the kinetic energy of the ion, z its charge state, and U_{Ret} the voltage applied to the retarding field plate in the RFA. Thus by scanning the voltage applied to the RFA, such kinetic energy distributions can be obtained for all the charge states that enter the detector [96]. It should be noted that the actual charge state composition and their kinetic energy distributions might be different inside the plasma compared to the measured ions at the ion detectors, because of recombination processes in the expanding plasma. Nevertheless, significant differences in measured charge states and kinetic energies at the detectors provide evidence of a changed plasma

composition.

3.2.2 High-order harmonic generation

After a delay $\Delta\tau$ with respect to the start of the pump pulse, the fundamental pulse is sent through the plasma to generate the high-order harmonics. This delay can be electronically varied without the need of an optical delay line, ensuring identical alignment for all delays. The fundamental or harmonic driving laser for this setup is a high-energy optical parametric chirped-pulse amplifier (OPCPA) system delivering ultrashort pulses down to 180 fs at a central wavelength of 1.55 µm, with pulse energies up to 10 mJ at a repetition rate of 100 Hz [51]. After spatial filtering with an 800 µm aperture to clean up the beam profile, up to 8 mJ of fundamental pulse energy reaches the experiment of which typically up to 6 mJ is actually sent into the experimental chamber. It is focused into the plasma plume with a 300 mm lens to a spot size of 115 µm (e^{-2} diameter), resulting in a laser peak intensity up to $6 \cdot 10^{14}$ W/cm^2 in the plasma plume to generate the HHs.

3.2.3 EUV spectrometer

As the HHs travel collinear with the fundamental beam, the EUV spectrometer is mounted in the line of sight of the fundamental beam. A retractable mirror M can be inserted into the beamline to send the fundamental beam and its low-order harmonics out of the vacuum chamber. Here the alignment of the fundamental beam through the experimental chamber can be monitored with the aperture pair A1 and A2. The overlap between the plasma and the fundamental beam can then be optimized by maximizing the third harmonic generation (THG) signal measured by the UV/VIS spectrometer as this signal is much stronger than the HHs and the acquisition time of the UV/VIS spectrometer is significantly shorter. Since the divergence of the HHs is typically lower than that of the fundamental beam, part of the fundamental beam is clipped by the final aperture A3 while transmitting most of the HH beam. A filter wheel (FW) is mounted behind the final aperture A3. This particular filter wheel can hold up to five different filters for transmitting the HHs in a specific spectral range while blocking the fundamental beam.

Within the EUV spectrometer chamber, a toroidal mirror under a grazing incidence angle of 7.5° is used to image the HH generation point onto the EUV camera (C) plane, with a demagnification of 1.8 to increase the spectral resolution. A grating mount holding up to three transmission gratings is placed between the toroidal mirror and the detector plane. The distance between the gratings and the detector plane equals 170 mm. These gratings are home-fabricated in collaboration with the AMOLF Nanolab cleanroom facility. For the fabrication, we sputter coat a 100 nm-thick gold layer on top of a free standing silicon nitride film with a thickness of 50 nm and a square clear aperture of 500 µm (Ted Pella). A binary grating containing several support structures is then patterned into the gold-coated film by means of a focused ion beam (FIB). For the current experi-

ments, a transmission grating with a line density of 1000 mm^{-1} is mounted in the holder to disperse the frequency components of the HHs and the EUV plasma emission.

To measure harmonics in the wavelength range above 70 nm, no suitable metal filters are available, and therefore we measure these HHs without any filter in the beamline. Since the EUV camera is unable to handle the intensity of the fundamental IR beam, a beam dump (BD) is placed between the transmission grating and the EUV camera to block the 0^{th} and -1^{st} diffraction order. The remaining 1^{st} order is transmitted to the EUV camera. Finally, the dispersed HHs and the plasma emission are collected and measured by an EUV camera (Greateyes GE 2048 512 BI UV3). This detector is mounted on a rotational stage, centered around the transmission grating. This allows us to conveniently rotate the camera to capture different spectral regions while keeping the distance between the grating and the EUV camera constant. Angles up to 18° with respect to the 0^{th} order can be reached in both directions. In combination with the 1000 mm^{-1} grating, this spectrometer allows us to measure a total wavelength span between 6 nm and 300 nm, while we can measure a range of 160 nm with a resolution around 1 nm in a single camera position. This resolution is limited by the clear aperture of the transmission grating and the imaging aberrations introduced by the toroidal mirror. The expected spectral widths of the HHs lie between 0.8 nm and 3 nm, and our spectrometer resolution is therefore sufficient to resolve the bandwidth of most HHs.

3.3 Results

To explore the capabilities and limitations of the setup, we first study HHG for various generation media. We then proceed to show the possibility for this experimental setup to function as a spatially and temporally resolved plasma diagnostic. Finally, we show the degree of control we can exert on the LPPs to systematically study the dependence of the HHG signal on the plasma composition.

3.3.1 HHG in various LPPs

In figure 3.2, we show the optimal HH spectra generated in LPPs from five different metals, namely aluminium, nickel, silver, indium, and tin. The motivation for these five materials lies in the differences in atomic weight and their differences in first and second ionization potentials. An overview of the atomic numbers Z, the masses, and the ionization potentials for all targets can be found in Table 3.1.

Measured HHG spectra for all tested elements are displayed in Fig. 3.2. The bottom panel in each measurement shows a camera image from which the static background signals from the fundamental beam and pump beam have been subtracted. All these results are averages of recordings at 21 separate spots on the target, with 150 laser shots on each spot. The remaining background signal in the images can be attributed to the remainder of the fundamental beam and the HHs in the 0^{th} order which are scattered from the beam dump onto the EUV

Table 3.1: Overview of atomic masses and ionization potentials of the materials used for LPP-based HHG. Ionization energies obtained from [97]

Target:	Z	Mass (U)	1^{st} Ip (eV)	2^{nd} Ip (eV)
Aluminium (Al)	13	26.98	5.98	18.8
Nickel (Ni)	28	58.69	7.63	18.2
Silver (Ag)	47	107.9	7.57	21.49
Indium (In)	49	114.8	5.79	18.9
Tin (Sn)	50	118.7	7.34	14.6

camera. The top panel in each graph shows the vertically integrated signal from the central 15 pixels around the HHG signal on the EUV camera image after further subtracting the sum of 15 vertical pixels located 50 pixels below the HH signal to reduce the broad background signal contribution.

A first observation from Fig. 3.2 is that the HHG spectra vary strongly for different elements, and require significantly different laser parameters to optimize HHG spectrum and flux. The optimum HH spectrum obtained in aluminium plasma was generated with a pump energy of 8 mJ, a fundamental energy of 4 mJ and a delay between the two pulses of 30 ns. The highest-order harmonic detected in these experiments is H17 at a wavelength of roughly 92 nm or a photon energy of 13.6 eV. Noticeably, the strength of H7 is much brighter than that of its neighboring harmonics, including the fifth harmonic. This observation might hint at a resonance enhancement effect, although further experiments are needed to verify this.

The pump energy and fundamental energy required to drive optimal HHG in nickel plasmas is similar to that of the aluminium case, namely 6 mJ and 4 mJ, respectively. Also the optimal delay of 30 ns is virtually identical to the aluminium case. The signal strength of the HHG in the nickel plasma is however more than two orders of magnitude lower compared to HHG in aluminium plasmas. The harmonic cutoff for HHG in nickel is also lower as the highest-order harmonic detected is H13.

For the case of silver, again similar laser energies were needed to drive HHG in the plasma plume. The optimum energies for pump and fundamental pulses were found to be 8 mJ and 2.5 mJ, respectively. Highest HHG yields were observed around a delay of 90 ns. The fundamental beam was more strongly absorbed in the silver plasma compared to the other targets. Additionally, the HHG spectrum shows a lower H9 intensity compared to the intensities of harmonics seven and eleven. This might be explained by the presence of the $4d^9 5p$ to $4d^9 7s$ spectral line of Ag II at 172.4 nm. However, other spectral lines can also be found in the vicinities of H7 and H11, while these harmonics seem to be absorbed less. Another possible explanation for the weaker H9 might be that the HH spectrum is cutoff at H9 while H11 is resonantly enhanced, although more research is needed to confirm this.

Typical HHG spectra in indium reach up to H17 with the highest signal strength for the low-order harmonics at pump and fundamental energies of 4 mJ

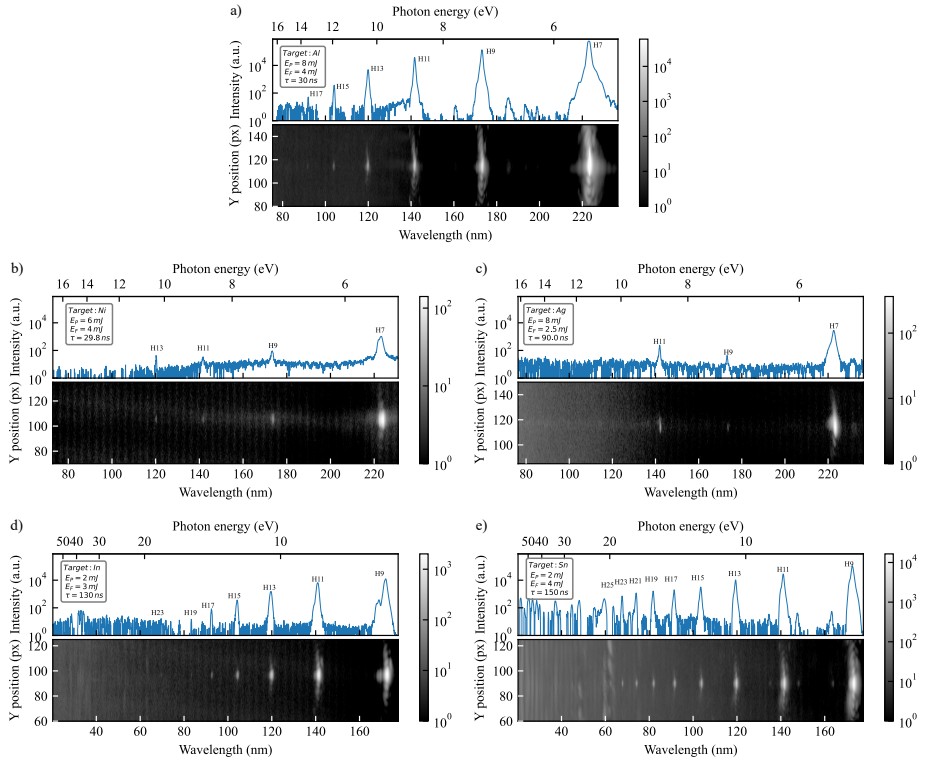

Figure 3.2: Typical HHG spectra for the a) Al, b) Ni, c) Ag, d) In and e) Sn targets. Experimental conditions can be found in the subfigure insets. All bottom panels show EUV camera images after subtraction of pump and fundamental background contributions. All top panels show vertically integrated spectra. Note that the HHG spectra for In and Sn have been acquired at a different EUV camera angle, shifting the spectral range of the spectrometer.

and 2.5 mJ, respectively. For a lower pump energy of 2 mJ, faint H19 and H23 signals are also observed. Contrary to the HHG signals observed in previous materials, In HHG spectra show a more plateau-like behavior up to H19, similar to expected spectra from conventional HHG in noble gases. The optimal delay between pump and fundamental pulses was found to be 140 ns.

The highest-order harmonics up to H25 were generated in tin plasmas. For these HHG spectra, a relatively low pump energy of 2 mJ was needed in combination with a fundamental energy of 4 mJ and a delay of 150 ns. The harmonic strength of H9 is comparable to that of H9 generated in aluminium, although the spectrum extends to much higher photon energies up to 19.9 eV. The HH intensity drops fast from H9 to H15, but a plateau region is observed up to H21, after which the HH intensity drops steeply again. Unfortunately, the harmonic spectrum has its cutoff below the expected resonance at a wavelength of 47.1 nm

or photon energy of 26.3 eV [36].

Overall, large differences are observed in the material-dependent HHG spectra. These differences cannot simply be explained with the differences in atomic weights between the targets as high signal strengths are observed for both light elements such as aluminium as well as for heavier elements such as indium and tin. Furthermore, low signal strengths have also been observed for both the lighter nickel as well as the heavier silver target. Also the first and second ionization potentials of the target do not seem to have a direct correlation with the HH strength. As most of the observed HH photon energies (except for tin) remain below the second ionization potential of the generation medium, a likely explanation is that most of the HHs are generated by neutral atoms rather than ions in the plasma.

3.3.2 HHG as plasma diagnostic

By varying the pump and fundamental laser energies as well as the delay between the two laser pulses, the HHG yield can be optimized, as the influence of these parameters on the local plasma properties results in different phase matching conditions. Vice versa, the HHG spectra at specific fundamental energies may therefore contain information on the plasma properties in which the HHs are generated. Figure 3.3 shows the tin LPP HH yield dependencies on pump energy and fundamental energy. From the pump energy scan, it can be seen that

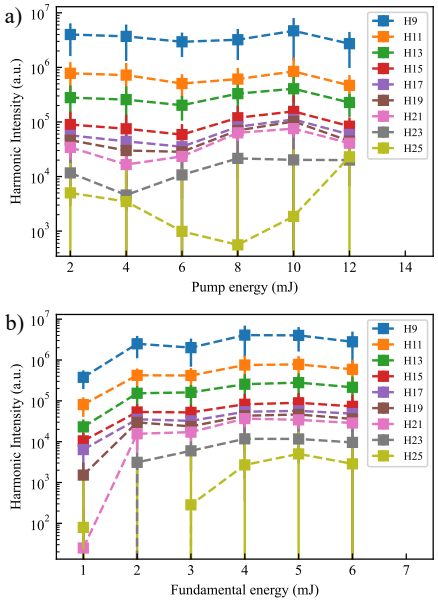

Figure 3.3: a) Pump energy scan for HHG intensity in tin plasmas at fundamental energy of 5 mJ and b) fundamental energy scan for HHG intensity in tin plasmas at pump energy of 2 mJ.

both the high-order harmonics and the low-order harmonics behave similarly, although the higher-order harmonics show a more pronounced decrease in signal strength at pump energies of 4 mJ and 6 mJ, hinting at slight differences in phase matching conditions between the high-order harmonics and the lower-order harmonics. Scanning the fundamental energy shows a steep increase in HH signal between 1 mJ and 2 mJ, after which this growth flattens resulting in stable HHG for higher fundamental energies. The HH signal scales more strongly for the higher-order harmonics. The brightness of H21 varies by more than two orders of magnitude, while the signal from the lower-order harmonics varies by only one order of magnitude.

This difference between lower-order and higher-order harmonics can be visualized even better with individual 2D intensity maps per harmonic for the full energy scan range, as shown in Figure 3.4. The grey scales of these plots are individually normalized. Note that the signal strength of H21 is nearly two orders of magnitude lower than that of H9. The harmonic yield for H9 and H13 vary less strongly as a function of pump and fundamental energies compared to H17 and H21.

From these plots it can be concluded that the brightness of all HHs peaks around pump and fundamental pulse energies of 10 mJ and 6 mJ, and that the higher-order HHs exhibit another local maximum at pump and fundamental energies of 2 mJ and 4 mJ, respectively. However, background signals due to e.g. scattered THG also increase for higher pump energies, which complicates back-

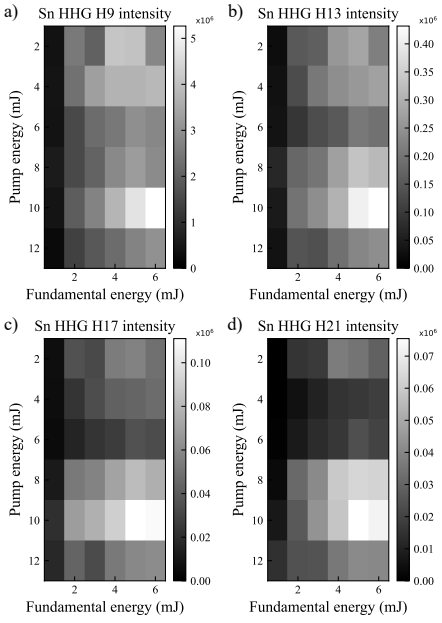

Figure 3.4: HHG intensity dependence on fundamental energy and pump energy in Sn LPP for a) H9, b) H13, c) H17, and d) H21.

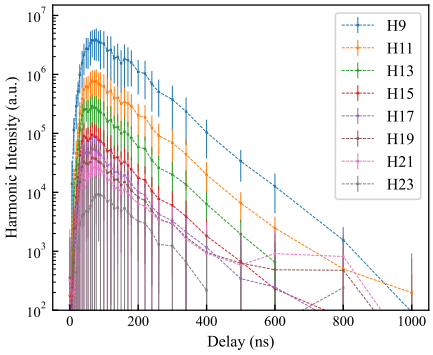

Figure 3.5: Observed HH intensity as a function of time delay between pump and fundamental pulses, for HHG in tin LPP generated with 0.43 ns-long, 2 mJ pump pulses, at a fundamental pulse energy of 4 mJ.

ground subtraction for the highest energies. The resulting lower signal to noise ratio is visible in the larger error bars for the highest pump energies in Fig. 3.3 a).

Scanning the delay between pump and fundamental pulses allows us to examine the temporal expansion dynamics of the tin LPP into the vacuum. The HH intensities as a function of delay are plotted in Figure 3.5. The distance between the fundamental beam and the target is optimized for harmonic yield by barely grazing the target in this delay scan. The estimated distance between the target and the fundamental beam waist is roughly 150 µm. At short delays, no HH signal is observed since the LPP has not expanded far enough into the vacuum to reach the fundamental interaction region. In the first 100 ns, the HH signal grows nearly exponentially as the LPP is expanding into the vacuum and enters the interaction region. The intensity of all harmonics peaks around a delay of $\tau = 80$ ns for this particular target-fundamental distance. After the optimum delay, the LPP expands even further into the vacuum and the medium density decreases, eventually becoming too low to efficiently generate HHs. In this expansion phase, the HH signal decays exponentially with delay. The decay rate of the HH intensities is largely identical for all HHs. We therefore conclude that in the present conditions, the main parameter that influences the yield for HHs up to order 23 is the density of the medium rather than phase matching effects.

3.3.3 Controlling the laser-produced plasma (Changing charge state composition)

All of the above results have been measured with the shortest Gaussian pump pulse length of 0.43 ns. However, the pump laser for these experiments has unique pulse shaping capabilities that allow us to control the generation of the LPP with high accuracy. We exploit this capability by also studying LPP for a longer and square pump pulse with a duration of 60 ns.

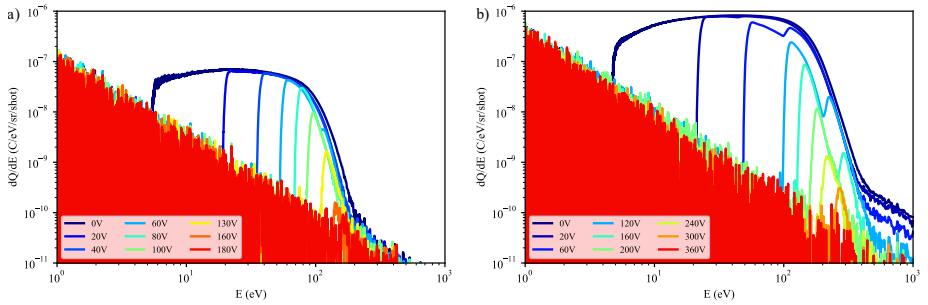

Figure 3.6: Kinetic energy distributions of ions detected with a retarding field energy analyzer for a) 5 mJ pump energy and b) 10 mJ pump energy. Different curves correspond to the set retarding voltages U_{Ret} on the retarding grid.

For these longer pump pulses, changing the laser energy will influence the charge state composition in the LPP [26]. This allows us to see the effects of the charge state composition in the LPP on the HHG spectra. As a proof of principle, we have generated HHs in LPPs pumped with 5 mJ and 10 mJ pump laser energies. The ion kinetic energy distributions dQ/dE measured at various set retarding voltages U_{Ret} for these two cases are plotted in Figures 3.6 a) and b), respectively. Although these plots show the kinetic energy distributions of the ions flying off the plasma, no information about the neutrals can be extracted from these measurements. As the ratio between neutrals and ions would be valuable information relating to the HHG phase-matching, this ratio is subject to further study. Note that the voltages shown are set retarding voltages and the actual voltages applied to the retarding grid may vary slightly because of the limited resolution of the HV supply. At 5 mJ pump energy there is mainly one smooth curve visible, meaning that the LPP mostly contains only singly charged tin ions. At 10 mJ pump energy a double-peaked structure appears, which indicates the presence of both singly and doubly charged tin ions. Additionally, the measured ion current per kinetic energy is higher in the 10 mJ case, as more mass is ablated which results in a higher LPP density. Finally, the maximum kinetic energy of the ions produced with a 10 mJ pump beam is 2-3 times higher than those produced with a 5 mJ pump beam.

We have generated HHs in these two distinct LPPs as a function of pulse delay to compare the dependence of the cutoff energy, the harmonic yield, as well as the temporal dynamics. The optimal HHG spectra for both pump energies are shown in Figures 3.7 a) and b), respectively. With the 60 ns pump pulses at 5 mJ energy, the measured HH intensity is roughly four times lower compared to the HH signal generated in the LPP pumped with 0.43 ns pulses. For this low pump energy case, the observed HHG spectrum remains quite bright and harmonics up to order 23 are observed, which is comparable to the shorter pump pulse case. Similar observations on the HHG cutoff with respect to the pump pulse length have been made by Ganeev et. al [44]. For these longer pump

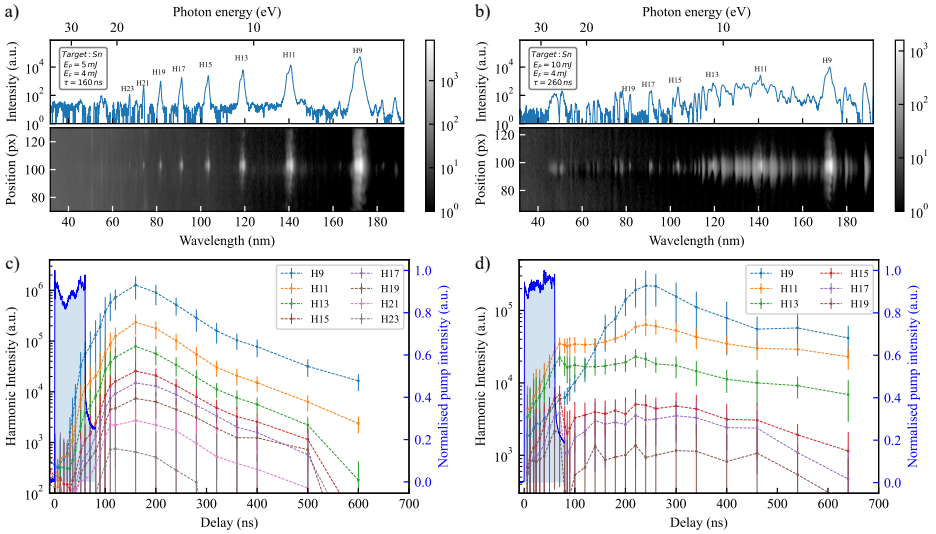

Figure 3.7: HHG spectra for optimized generation conditions using a) 5 mJ and b) 10 mJ pump pulse energy at 60 ns pump pulse duration. The bottom row shows the observed HH intensity as a function of time delay between pump and fundamental, for the same pump energies of c) 5 mJ and d) 10 mJ. The blue shaded curves in c) and d) display the normalized temporal shape of the pump pulses. All HHG spectra and delay scans are generated with 4 mJ fundamental beam energy.

pulses, the pump laser energy has a more pronounced effect on the HH cutoff and intensity. Only HHs up to order 19 were observed when using 10 mJ, 60 ns pump pulses, whereas the highest observed harmonic for the 10 mJ, 0.43 ns pump beam was H23. The observed HH signal strength is significantly lower at 10 mJ pump energy compared to the 5 mJ case. One reason for this decrease in HH signal is the increased fundamental absorption in the higher-density LPP. This increased absorption also leads to a temperature rise in the LPP, resulting in a higher ionization fraction and increased EUV-UV emission, which appears as a multitude of spectral lines that form a background to the measured HHG signals in Fig. 3.7b).

The HH intensities as a function of delay pumped with the 60 ns-long pulses of 5 mJ and 10 mJ are shown in Figs. 3.7 c) and d), respectively. The blue shaded curves display the normalized temporal shape of the pump laser. The slowly decaying tail of these curves can be attributed to the electronic response of the photodiode rather than the actual pump intensity. The pump-to-fundamental time-delay dependence of the HHG also shows markedly different behavior for the 5 mJ and the 10 mJ pump energies, as can be seen in Figs. 3.7 c) and d). At 5 mJ pump energy, the HH signal starts rising after roughly 30 ns delay time. This HHG onset delay is much longer compared to the 0.43 ns pump pulse cases where HH signal appears from delays of $\tau = 10$ ns onwards. After a steep increase up to

roughly 60 ns, the signal keeps growing until it peaks around 160 ns. Afterwards, as the plasma expands into the vacuum its density decreases, leading to a decrease in HH intensity as well.

For the $E_P = 10$ mJ case, the fundamental pulse leads to a more rapid heating of the LPP, resulting in an apparent signal increase in the first tens of nanoseconds as seen in Fig. 3.7d), which however is mainly caused by incoherent background emission from the plasma rather than actual harmonics. The actual HH signal appears above this background after a delay of 130 ns after which it peaks around 260 ns. The decrease in signal strength for the 10 mJ case is much slower compared to the 5 mJ case. Weak HH signals were observed up to delays of 1.6 microseconds, whereas at 5 mJ pump energy the maximum delay for which HH signals remained visible was 1.0 µs.

3.4 Discussion and outlook

The highest-order harmonics generated in our five different targets remained well below values reported in literature [33, 34, 37, 38]. Considering the maximal ponderomotive energy from the peak intensity of the fundamental laser pulses $U_P = 45$ eV for a pulse energy of 4 mJ, much higher-order harmonics could be expected, although plasma effects such as electron defocusing are likely to reduce the actual peak intensity in the plasma. In addition, phase matching effects may be expected to dominate the observed HHG spectrum rather than the single-atom response: free electrons in the plasma and the additional ionization in the leading edge of the relatively long fundamental pulse can therefore also be a cause for the observed HHG cutoff. To this end, it is simplistic but insightful to consider the barrier suppression intensity above which atoms or ions are further ionized [34], which would lead to the generation of significant amounts of free electrons that generally inhibit phase matching. In the case of aluminium, the barrier suppression intensity above which all neutral Al will be ionized is $1.0{\cdot}10^{13}$ W/cm^2. At a central wavelength of 1560 nm, this corresponds to a ponderomotive energy of $U_P = 2.24$ eV. From this, the single atom response predicts a cutoff energy of $E_C = 3.17 \cdot U_P + I_P = 13.2$ eV, which is 16.5 times the photon energy of the fundamental. As this number nearly matches the highest-order harmonic observed with a photon energy of 13.6 eV, it seems reasonable to assume that the observed HHs are generated from neutral Al atoms rather than ions.

Continuing this reasoning, the expected cutoff energies for neutral nickel, silver, indium and tin are 13.1 eV, 10.7 eV, 7.6 eV and 10.1 eV, respectively. These cutoff energies are calculated assuming a barrier suppression intensity scaling of $F_{BSI} = \frac{I_P^2}{4Z}$ [98]. The observed HH cutoff energies in our experiments were 10.4 eV, 8.8 eV, 15.2 eV and 20 eV for Ni, Ag, In and Sn, respectively. From this simple model, we can expect to generate HHs mostly in neutrals for Al, Ni and Ag LPPs, while HHs from singly charged ions can be generated in In and Sn LPPs. However, the harmonic cutoffs for In and Sn do not scale according to a single-atom law with the second ionization potential either, making it apparent that phase matching still dominates HHG in these elements. In general, a better

model is needed to predict whether the HHs are generated from neutrals or ions. Furthermore, shorter fundamental pulses are likely to improve HHG yield as well.

In our energy scans with the HHG in Sn LPPs, we observe variations in HHG signal strength that allow optimizing the yield of individual HHs. For now the observed variations in HHG spectra are too small to consider this a quantitative plasma diagnostic, although we obtained a bright HH signal up to H25.

The delay scans measured with both the 0.43 ns-long pump pulses and the 60 ns-long pump pulses show large differences in HHG spectra. Especially the differences between the two pump energies for the 60 ns-long pulses are very pronounced, whereas this effect was much less noticeable for the 0.43 ns pump pulses. This difference is probably due to the more efficient plasma heating for the 60 ns pulses, leading to an overly dense plasma for efficient HHG.

While the available parameter space especially in terms of pump pulse properties is much larger, the present set of experiments already showcases the capabilities of our LPP-based HHG setup. The present experiments clearly show some characteristics of the expanding LPPs generated by laser pulses of two different pulse lengths. More advanced experiments on HHG in LPPs generated with various temporal laser shapes in combination with ion diagnostics will be performed in future experiments, to systematically characterize these LPPs and optimize HHG yield. Through these experiments, we aim to provide a better understanding of the generation mechanisms and dominant charge states involved in the HHG process.

3.5 Conclusion

We have shown a new experimental setup capable of successfully generating HH radiation of a fundamental laser with a central wavelength of 1560 nm in various LPPs. Large differences in both HH yield and harmonic cutoff energy have been observed which cannot be explained by only considering differences in atomic number and the first and second ionization potentials of the target species. HHG in aluminium LPPs has shown a very bright H7 compared to neighboring harmonics H5 and H9, which may hint to the presence of a resonance enhancement. HHG in tin LPPs has shown the highest-order harmonic of H25 with a bright overall harmonic yield. Energy scans for pump and fundamental lasers have shown differences in harmonic yield and differences in phase matching for different harmonics. A delay scan with the 0.43 ns-long pump pulse has shown an increase in HH yield as the plasma expands into the interaction region, after which the further expansion dilutes the LPP to densities where no efficient HHG is possible. Finally, very different LPP expansion dynamics were observed for the 60 ns-long pump pulses with low and high energy compared to the 0.43 ns-long pump pulses.

Acknowledgments

The authors thank Nik Noest for technical support, Lucas Poirier for his contribution to the RFA data analysis, and Dr. Aneta Stodolna and Tiago de Faria Pinto for their contribution to the development of the setup. This work has been carried out at the Advanced Research Center for Nanolithography (ARCNL), a public-private partnership of the University of Amsterdam, the Vrije Universiteit Amsterdam, the Netherlands Organization for Scientific Research (NWO) and the semiconductor equipment manufacturer ASML.

Declarations

Conflicts of interest The authors declare that they have no conflicts of interest.

Chapter 4

Laser-induced plasma dynamics probed with high-order harmonic generation

Abstract

We present high-order harmonic generation (HHG) in laser-produced tin plasmas under various plasma generation conditions. Temporally shaping the plasma-generating laser pulse envelope shape as well as its duration allows us to control the plasma properties in which the HHG takes place. Adjusting the delay between the plasma-generating pulse and the HHG driving pulse gives insight in the laser-produced plasma expansion dynamics under these varying conditions. The generation efficiency of highest-order harmonics correlates with the presence of high-energy ions with higher average charge state. Lowest-order harmonics are most efficiently generated in lower density plasmas created with longer, square-shaped pump pulses.

4.1 Introduction

High-order harmonic generation (HHG) is an established technique that provides broadband coherent extreme-ultraviolet (XUV) radiation from a compact, table-top setup. This method has been well studied and can be understood by the three step model, describing the nonlinear interaction between the driving ultrafast laser pulse and the generation medium (typically a noble gas) in the single atom and single active electron picture. The three step process occurs every half laser cycle, resulting in a power spectrum consisting of multiple odd harmonics of the fundamental laser frequency. As the HHG process takes place within an optical cycle of the driving pulse, HHG has also opened up the world of attosecond sciences [6].

The concept of producing HHG radiation in laser-produced plasmas (LPPs), rather than noble gases, originates from 1992 [30]. In that experiment, rare-gas-like ions of Li^+, Na^+, and K^+ (produced by exciting alkali metals with a KrF laser) with large ionization potentials were utilized as generation media in an attempt to increase the generated photon energy (cutoff energy). Such cutoff extensions remained limited, as the high density of free electrons leads to phase matching challenges, as well as defocusing effects. Still, large progress has been made in this field. Currently, the highest-order harmonic generated in manganese LPPs is harmonic order 107, and high conversion efficiencies up to $5 \cdot 10^{-5}$ for the 11^{th} - 19^{th} harmonics have been achieved in Zn LPPs [42]. Furthermore, some target materials used for HHG in LPPs have shown resonant behavior of a single harmonic order, under the right circumstances resulting in a two orders of magnitude increase of intensity for the resonant harmonic [37, 38]. A new four-step model has been proposed that splits the final recombination step of the three-step model into recombination to an auto ionizing state and subsequently a resonant recombination to the ground state [36].

Besides the HHG medium, parameters for both the plasma generating (pump) laser, as well as the high-order harmonic driving (fundamental) laser are of vital importance to efficiently generate high-order harmonics. It has been shown that plasmas formed by laser pulses with different durations have different ablation characteristics and ion kinetic energy distributions [18, 19, 99–101]. In turn, these differences are expected to result in different HHG spectra, as their distinct densities and ion kinetic energy distributions affect both the single atom/ion HHG response, as well as the phase matching conditions in the plasma cloud.

Few experiments are found in literature investigating the influence of the pump pulse on the resulting HHG spectrum. It has been shown that varying the pump pulse length over multiple orders of magnitude does not considerably affect the harmonic cutoff when generating in medium to heavy elements [44]. The longest pump pulse length in this study was limited to 210 ps, although a secondary pump laser with a different wavelength and a pulse length of 20 ns was also employed in some of the measurements. The influence of the pump pulse duration on the intensity of the harmonics was not discussed in the abovementioned reference. Further studies have shown that producing the LPP with shorter femtosecond pulses has a positive impact on the signal stability in the case of stationary

targets, as well as an increase in harmonic cutoff and harmonic yield for non-stationary targets [102].

This work presents the generation of high-order harmonics in LPPs produced with varying pump pulse lengths in the range of 0.5 to 50 ns. Furthermore, we control the envelope of the pump pulse to form Gaussian and square shapes, and we tune the delay between the pump pulse and the fundamental driving pulse. To characterize the plasma conditions at which the HHG is produced, we perform ion diagnostics using a retarding field analyzer (RFA)

4.2 Experimental setup

The experimental setup for producing HHG radiation in plasmas pumped with varying pump pulse durations and shapes is fully described in Chapter 2 [89]. To recall, we now briefly describe the setup, as is depicted in the top panel of Figure 4.1. First, the pump laser is focused onto the target of interest in the experimental vacuum chamber. This laser ablates the target in the region of the focal spot with a e^{-2}-diameter of 450 µm, resulting in a laser-produced

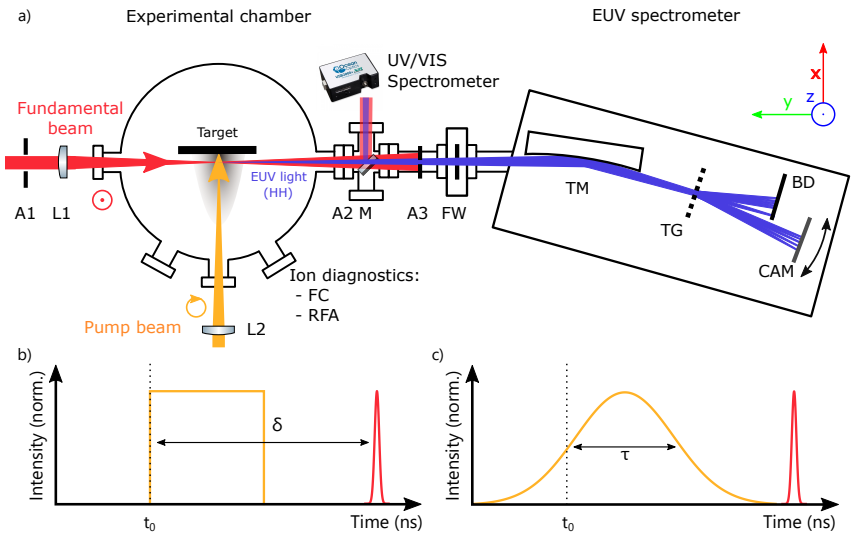

Figure 4.1: a) Experimental setup for producing HHG radiation in laser-produced plasmas. Arrows next to pump and fundamental beams represent their respective polarization state. Optical components: A: Aperture, L1: f = 300 mm lens, L2: f = 1000 mm lens, M: insertable mirror, FW: filter wheel, FC: Faraday cup, RFA: retarding field energy analyzer, TM: toroidal mirror, TG: transmission grating, BD: beam dump, CAM: EUV CCD camera (Greateyes). The two graphs on the bottom represent the parameter space of the current experiment, adjusting the delay δ between pump and fundamental pulse, adjusting the full width at half maximum duration τ of the pump pulse, and shaping the temporal pump pulse in b) square pulses, and c) Gaussian pulses.

plasma at the surface of the target. After an electronically configurable delay, the probe laser (the fundamental beam) for generating harmonics, is focused in this LPP to a e^{-2}-diameter of 120 µm, perpendicular to the pump laser. The peak intensity of the fundamental beam reaches almost $5 \cdot 10^{14}$ W/cm^{-2} for a pulse energy of 5 mJ. At these intensities, high-order harmonics (HHs) are generated in the plasma, which are subsequently imaged by a toroidal mirror onto the EUV CCD camera, detecting the generated EUV radiation. The HHs are spectrally separated by a transmission grating with a groove density of 1000 mm^{-1}, resulting in a spectrometer resolution around 1 nm. Besides the main EUV spectrometer, an insertable mirror can divert the beam to a UV/VIS fiber-based spectrometer (Ocean Optics) to monitor low-order harmonics of the fundamental beam in real-time.

Complementary to the HHG measurements in the plasma for varying pump parameters, we have captured retarding field analyzer (RFA) traces to study the plasma composition upon changing pump pulse length τ and the envelope shape of the pump pulses. During the acquisition of the RFA measurements, the fundamental beam was absent. The RFA ion diagnostics are mounted on the experimental chamber at a small angle of 9° with respect to the incident pump beam, see Fig. 4.1. The RFA measurements allow us to measure the kinetic energy distributions of the ions emitted by the LPP. These distributions are obtained by measuring the time-of-flight ion currents and converting these to ion kinetic energy spectra. Scanning the retarding field voltage on the RFA and performing the bottom-up analysis presented by Poirier et al. [25] allows us to resolve these ion kinetic energy spectra for individual charge states. Faraday-cup-like (FC) kinetic energy spectra can be obtained by turning off the retarding field voltage. For these measurements, data is averaged over ten spots on the target for every retardation voltage. Depending on the pulse duration and its shape, the first few laser shots of every spot are left out of the analysis to discard ion data from native oxides and other contamination sources on the surface of the target. The subsequent 20 laser shots of every spot are selected for data acquisition. The bottom-up analysis for these experiments is limited to retrieve ion kinetic energy spectra up to $z = 4$.

4.2.1 Pump laser pulse parameters

In this work we utilize the unique pulse-shaping capabilities of the sub-nanosecond (SNS) laser system to produce a multitude of pulse shapes that create the plasma at the surface of the tin target in the experimental chamber [88]. More specifically, pulses with either a square or a Gaussian envelope are sent into the experiment, as is depicted by the bottom two panels in Figure 4.1. For both of these temporal shapes, we vary their lengths τ between 0.5 ns and 50 ns. The shortest square pulse is however limited to 2 ns as that is the shortest square pulse that can be achieved with the system. Because of limited space on the target, the data for this work are acquired on two consecutive days. For the best comparison between different pulse shapes, measurements with different shapes (Gaussian and square) at a given pulse duration were performed on the same day.

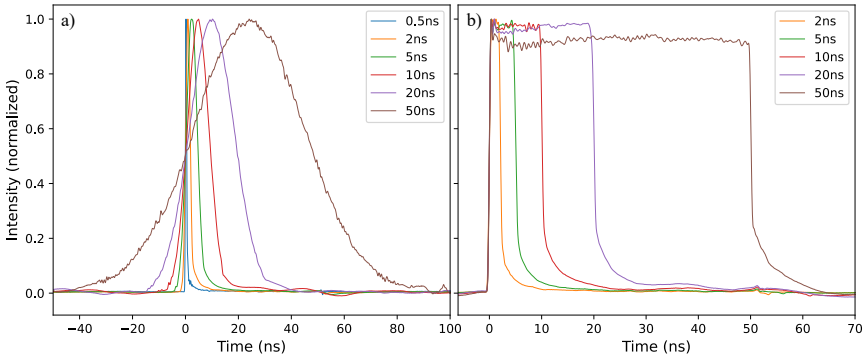

Figure 4.2: Measured pump pulse waveforms for a) Gaussian pump shape, and b) square pump shape. Different curves correspond to the various pulse lengths. These traces are individually normalized for visualization purposes, in all measurements the pulse energy was kept constant at 5 mJ.

The pump pulse energy is kept constant at 5 mJ during all measurements. We measured the temporal shapes of these pulses with a fast photodiode close to the experiment and used this data to optimize the shape as close to the experiment as possible. The resulting traces are plotted in Figure 4.2. In this figure, all curves are normalized to their highest intensity value for better visibility. Note the different time scaling for the two subplots. All pulses show a decaying tail at the end of the pulse, which is particularly visible for the sharp square pulses. These tails are artifacts from the photodiode and are not present in the actual laser pulses.

Besides changing the temporal shape of the pump pulses, we also coarsely scan the delay between pump and fundamental pulses. This allows us to probe the expansion of the LPP into the vacuum chamber. We define this delay as the time between the first half maxima of the pulse intensities, as is depicted in the top right panel of Figure 4.1. The delay is matched with the timescale of the expansion time needed for the LPP to reach the interaction zone with the fundamental beam. Within tens of nanoseconds the LPP has expanded enough to reach the interaction zone, as we have already demonstrated in Chapter 2. From previous measurements on plasma-based HHG, we expect maximum HHG yields around 100 ns delay, after which the HHG signal should gradually decrease. For that reason, we have selected three delays of 50 ns, 100 ns, and 150 ns.

4.3 Influence of temporal pump pulse shape on resulting plasma

To examine the influence of the laser-produced plasma conditions initiated by the pump beam on the resulting HHG, we first study the ions emitted by these LPPs under the various pumping conditions with the RFA. These measurements are displayed in Figure 4.3.

From these plots, we can immediately see a reduction of ions, as well as a reduction of the average charge state present in the LPP, upon increasing the length of the pump pulse. For the shortest pump pulse duration of 0.5 ns, charge states up to $z = 4$ are detected with the RFA. Pumping the target with 2 ns-long pulses results in charge states up to $z = 3$. LPPs pumped by 10 ns-long pulses mostly contain charge states up to $z = 2$, and predominantly 1+ ions are detected for the longest pump pulses of 50 ns. Similarly, the maximum kinetic energy of the detected ions is decreased by roughly one order of magnitude from multiple keV to several hundred eV as the pump pulse length is increased from 0.5 ns to 50 ns.

Differences between ion energy spectra for Gaussian and square pump pulses are more subtle. Especially for the short 2 ns pump pulses, the Gaussian and square pulses result in nearly identical ion energy spectra. However, the presence of higher charge states is slightly more pronounced for the Gaussian pump pulses. This can be attributed to the higher peak intensity of the pump pulses, as well as a longer interaction time period for the heating of the plasma by the laser pulse. Similarly for the 10 ns pump pulses, only a slightly higher fraction of $z = 2$ ions can be spotted for the Gaussian pulses compared to the square pulses. Gaussian and square pulses with lengths of 50 ns vary the most, as is expected from their greater differences in shape. Twice as many ions are generated with the square pump pulse, compared to the Gaussian pump pulse. The overall kinetic energy distribution remains the same shape, although an increase of $z = 2$ ions is present at an energy of 100 eV for the Gaussian pulse.

The decrease of ions emitted by the LPP as a function of pump pulse length can be explained by considering the plasma onset time t_{on} at which laser ablation is initiated. This plasma onset time scales with laser intensity I as $t_{on} \propto I^{-2}$, which has been theoretically predicted and experimentally verified [18, 103]. Increasing the pulse length τ thus results in the reduction of ablated material as the plasma onset time scales faster with laser intensity. This relation can then also explain the difference in ion current for square and Gaussian pulses, as square pulses reach the needed ablation intensity threshold faster than the Gaussian pulses, leading to a higher fraction of absorbed laser energy.

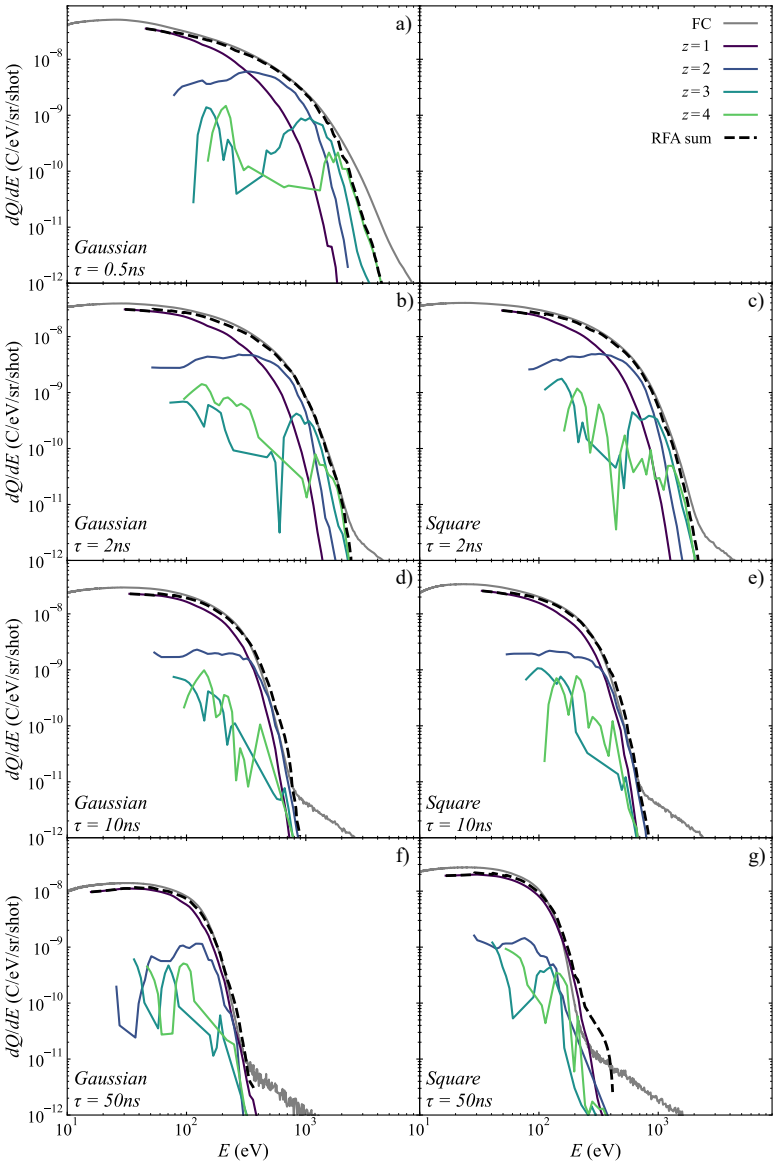

Figure 4.3: Charge state-resolved energy distributions measured with the RFA for both pulse shapes and a selection of pulse lengths. Colored lines correspond to energy distributions for individual charge states z, as retrieved from the bottom-up analysis. The sum of all the colored lines (black dashed curve) matches the FC-like energy distribution (gray line). Different subplots correspond to ion kinetic energy distributions pumped by Gaussian (a), b), d), f)) and square (c), e), g)) pulses at pulse lengths of a) 0.5 ns, b) and c) 2 ns, d) and e) 10ns, and f) and g) 50 ns.

4.4 Influence of temporal pump pulse shape on high-harmonic spectra

4.4.1 Pump pulse shape dependency

Although only small differences in ion kinetic energy spectra were observed between plasmas pumped with a Gaussian or square temporal profile, the nonlinear process of high-order harmonic generation does result in differences in the generated XUV spectra. Figure 4.4 displays a comparison of the HH spectra produced by Gaussian and square pump pulse shapes, for pump pulse durations τ between 0.5 ns and 50 ns, at a fixed delay of $\delta = 100$ ns. These measurements have also been carried out for delays δ of 50 ns and 150 ns. These spectra are shown in appendix 4.A, Figure 4.7. For all of the spectra acquired at a delay of 100 ns, a clear harmonic signal up to harmonic order 19 is visible. In the pump pulse length range up to 5 ns, the Gaussian and square pulses behave quite similar as for these short pulses, the shapes are not very different yet. A clear difference can however be spotted by comparing the fundamental-induced plasma glow background. Note that the pump-induced plasma fluorescence and the fundamental backgrounds have already been subtracted from these spectra. This additional fundamental-induced plasma background is significantly stronger for the plasma formed by the Gaussian pump pulse than for that pumped by the square pulse. The fundamental pulse is thus absorbed more in the Gaussian-pumped plasma. This effect seems to have little effect on the generation of lower-order harmonics, although the higher order harmonics become masked in background noise for the Gaussian pulses. Looking closer at the spectra for short pump pulse lengths of $\tau = 2$ ns and $\tau = 5$ ns, we can see that these higher-order harmonics are still present for the Gaussian-pumped plasma, and are even slightly stronger compared to the square-pumped plasma.

For greater pump pulse lengths at the same delay, the fundamental-induced pump glow background is reduced. This reveals the visibility of higher-order harmonics up to order 27. Considering the actual high-order harmonics generated in these plasmas, the Gaussian- and square-pumped HHG spectra show similar signal strengths for the highest-order harmonics, while the lower-order harmonics are clearly brighter in the square-pumped HHG spectrum. This shows a possible correlation between the presence of higher charge states for the short Gaussian-pumped LPP and the stronger highest-order harmonics, indicating that these highest-order harmonics might be generated in a different ion species. This could then also explain the increase in signal for the lower-order harmonics generated in the square-pumped LPP, as the average charge state in this plasma is lower compared to the 50 ns Gaussian-pumped plasma. Another interesting observation is that for the 50 ns pump pulses, the bandwidth of the generated harmonics is larger for the square pulses compared to the Gaussian pulses.

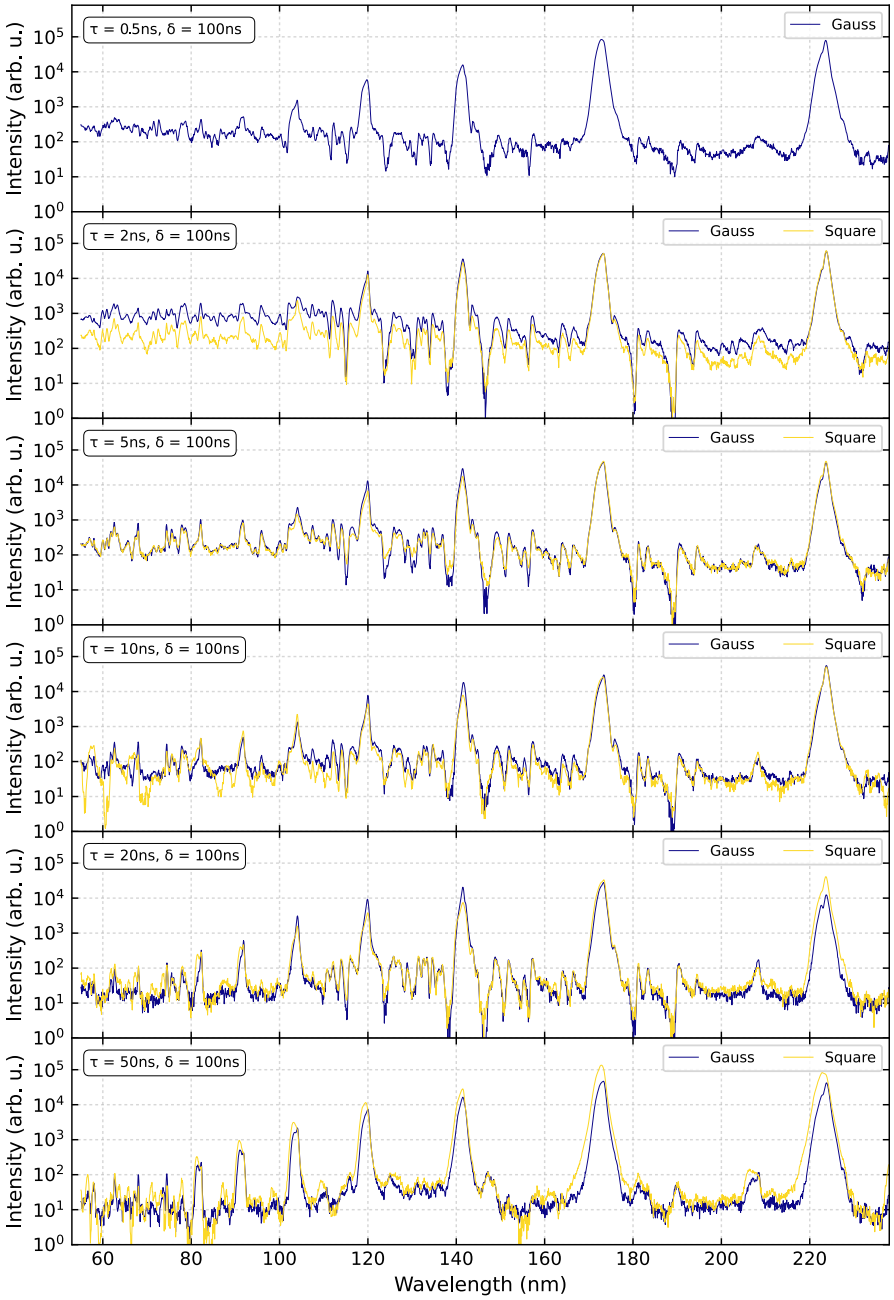

Figure 4.4: Comparison of experimentally obtained HHG spectra pumped with Gaussian or square pulses. All displayed spectra are measured at a fixed delay of $\delta = 100\,\text{ns}$. Different subplots correspond to the various pump pulse lengths τ, ranging from 0.5 ns to 50 ns.

4.4.2 Dependence on pump pulse length

To display the dependence of the pump pulse duration on the HHG spectrum, we have plotted the HHG spectra for the different pump pulse durations in Figure 4.5. The top panel displays the HHG spectra obtained from an LPP generated with Gaussian pulses, and the bottom window shows the HHG spectra from an LPP generated with square pump pulses. Again, both of these figures are acquired at a fixed delay of $\delta = 100$ ns. In both cases we can clearly see the pump-induced plasma glow increasing as the pump pulse length decreases. This can be explained by the lower plasma density for the longer pulse durations, leading to a reduced absorption fraction of the fundamental beam. As for the measurements comparing square and Gaussian pulse shape envelopes, the measurements for different pump pulse durations have also been performed at delays δ of 50 and 150 ns. These results are displayed in appendix 4.A in Figure 4.8. Additionally, individual harmonic yields are plotted as a function of pulse length in Fig. 4.9.

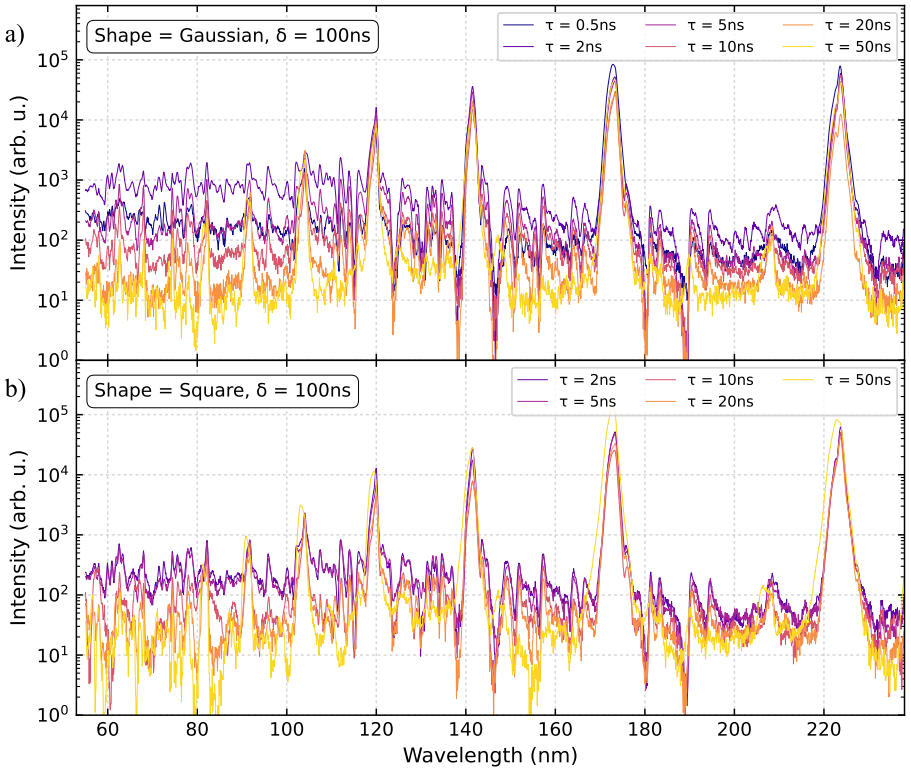

Figure 4.5: Comparison of experimentally obtained HHG spectra pumped with pump pulse durations between 0.5 ns and 50 ns. a) HHG spectra obtained in Gaussian-pumped LPP at delay of 100 ns. b) HHG spectra obtained in square-pumped LPP at delay of 100 ns.

The generated harmonic spectra clearly vary as a function of pulse duration. For the Gaussian pulses, higher signal strength for the complete harmonic spectrum is observed as the pump pulse duration decreases. The fundamental-induced plasma glow background rises faster than the increasing harmonic strength, resulting in a reduced visibility of the harmonics. This effect could however be mitigated by further exploiting the coherent properties of the HHG radiation and decreasing the clear aperture of the EUV spectrometer, reducing the relative fraction of plasma glow on the EUV detector.

The square-pumped HHG spectra show a slightly different behavior as a function of pulse duration. The lower-order harmonics show a local minimum for intermediate pulse lengths of 10 and 20 ns. A clear peak in intensity for the lower-order harmonics is visible for the longest pulse length of 50 ns. However, as for the 50 ns Gaussian pump pulses, the highest-order harmonics are actually weakest for the 50 ns square pump pulses. The two shortest square-shaped pump pulses result in the best overall HHG spectra with intermediate signal strength in the low-order harmonic range and bright harmonic signal up to order 25.

Overall, shorter pump pulses shift the generated harmonic spectra to higher photon energies, but also increases plasma glow in this spectral range. These effects are clearly visible by comparing the HHG spectra for the different pulse durations in Fig. 4.5. From the ion kinetic energy distributions plotted in Fig. 4.3, we observe that the LPP in which the highest-order harmonics are most efficiently generated contains more and faster ions, as well as a higher average charge state. The increase in fundamental-induced plasma glow can thus be attributed to the higher density of the LPP, as the effect decreases with increasing pulse duration.

4.4.3 Pump-to-fundamental delay dependency

So far we have only considered the HHG spectra obtained at a fixed pump-to-fundamental temporal delay δ of 100 ns. To also capture the dynamics of the plasmas formed with different shapes and pulse durations, the harmonic spectra have been recorded at three pump-to-fundamental delays of 50 ns, 100 ns, and 150 ns. We highlight the difference in plasma expansion dynamics in Figure 4.6 by plotting the captured HHG spectra measured at the three different delays for the longest and shortest pulse durations and for both pulse envelope shapes. The shortest delay of 50 ns mostly outperforms the longer delays for the highest-order harmonics pumped with the Gaussian pulse shape. At these short delays, the LPP is still expanding into the interaction region. Because the Gaussian pulses already deposit some of their energy on the target before $t = 0$ ns, more plasma is present in the interaction region for the Gaussian pulses compared to the square pulses, resulting in the better yield. As the plasma expands in the vacuum chamber, initially a dense front of plasma reaches the interaction zone with the fundamental beam. In this initial expansion phase, the HHG yield rises quickly as a function of delay. This can be seen in Fig. 4.6, where the low-order harmonics for all displayed pump pulse configurations show a large increase in signal strength from $\delta = 50$ ns to $\delta = 100$ ns. Intermediate delays of 100 ns result

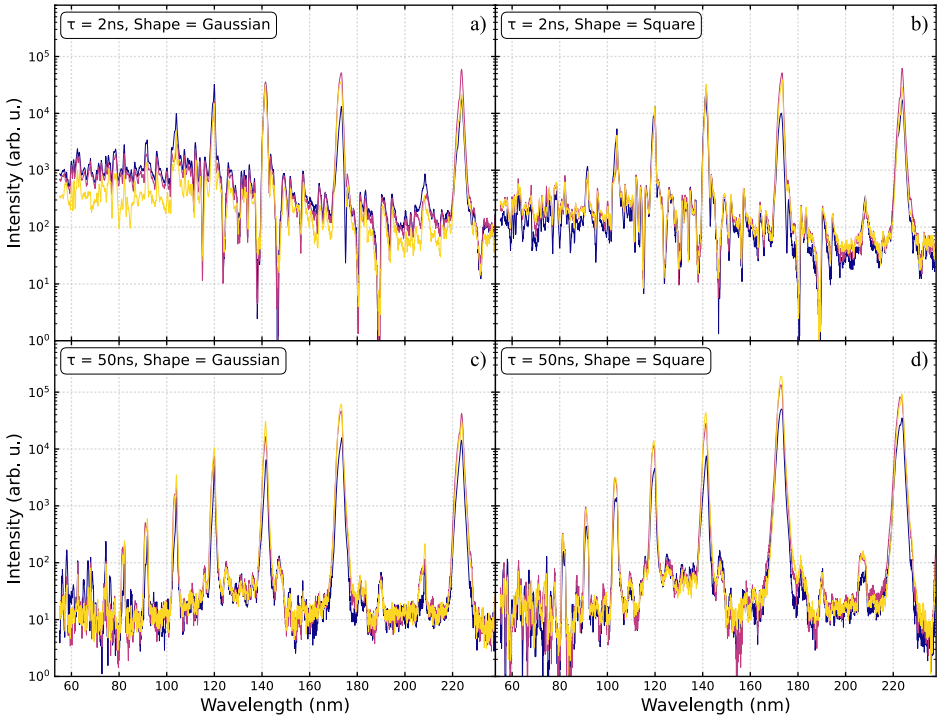

Figure 4.6: Experimentally obtained HHG spectra measured at delays of 50 ns (blue line), 100 ns (purple line), and 150 ns (yellow line). a) and b), LPP pumped by 2 ns pulses with Gaussian and square pulse envelopes, respectively. c) and d), LPP pumped by 50 ns pulses with Gaussian and square pulse envelopes, respectively.

overall in bright HHG spectra across the whole spectral range investigated. The signal strength compared to the highest-order harmonics is comparable of that generated at 50 ns delay. However, the strength is much higher for the lower-order harmonics. Specifically, the strength for harmonic order 9 is up to six times higher for all displayed pulse configurations. Somewhat longer delays of $\delta = 150$ ns result in comparable lower-order harmonic signals compared to the 100 ns delay. Here, long pump pulses result in slightly higher signal strengths. This can be attributed to the slower expansion velocity of the plasma due to the lower peak intensity.

The plasma generated with the 50 ns Gaussian pulses emits ions with kinetic energies in the range of 10 eV to 300 eV. Estimating the distance between the target and the fundamental beam to be 200 µm and assuming plasma expansion purely normal to the target surface, slow ions with energies of 10 eV will traverse the interaction region in roughly 57 ns, while faster 200 eV ions with higher average charge state pass the interaction zone within 12 ns. The average charge state within the interaction zone thus initially steeply increases as the fast ions

reach the fundamental beam. Afterwards, the average charge state decreases as a function of delay. This trend supports the higher signal strength of higher-order harmonics at small delays for the plasma produced by 50 ns Gaussian pulses. Comparing with the 50 ns square pulses, lower signal strength for the highest-order harmonics is expected at these short delays due to the lower average charge state, as is observed in our experiments. Additionally, the increase in low-order harmonic signal for the 50 ns square pump pulse also complies with the correlation to the average charge state. The plasmas generated with 2 ns pulses contain more, faster ions than for the 50 ns pump pulses. The average charge stage is also higher. Following the same reasoning as above, we expect to observe the highest harmonic signal at earlier delays. For the short 2 ns Gaussian pulses, we indeed observe that harmonic orders 13 to 25 have the brightest signal at $\tau = 50$ ns and decrease with increasing delay. The lower-order harmonics generated by slower ions still show an increasing signal strength up to 100 ns, after which the signal also reduces. Similar trends are observed for the 2 ns square pulses.

Besides affecting the HHG spectrum, increasing the delay is also expected to reduce the fundamental-induced plasma glow as the expanding plasma becomes less dense and thus absorbs less from the fundamental pulses. A slight effect of this is observed for the Gaussian pulses, as can be seen in Fig. 4.6. However, the timescale at which the plasma expands into the vacuum chamber exceeds our longest pump-to-fundamental delay of $\delta = 150$ ns, such that a significant fundamental-induced plasma glow is still present at this delay.

Although this portrayed explanation is likely too simple to predict quantitative HHG signal strengths, it does sketch a qualitative picture for the expansion dynamics of the laser-produced plasmas as a factor for HHG yield. As the RFA kinetic energy spectra are calculated from one initial time at which the pump laser starts hitting the target, complex plasma dynamics with ions emitted over a prolonged period of time can not be reconstructed with the RFA measurements. For this reason, numerical modeling with e.g. RALEF-2D radiation-hydrodynamic simulation code can provide more insights into plasma expansion at these early timescales [104].

4.5 Conclusion

In this work, we have investigated the effect of varying plasma formation conditions on high-order harmonic generation. The pump pulse length was varied from 0.5 ns to 50 ns, and both Gaussian- and square-shaped pulse envelopes have been utilized to form the plasma. Additionally, the delay between plasma formation (pump) pulse and harmonic driving (fundamental) pulses have been varied from 50 to 150 ns. By means of RFA measurements for the varying plasma formation conditions, we have shown that short pump pulses result in more dense laser-produced plasmas containing more, faster ions with higher kinetic energies. Pump pulses with Gaussian envelope shapes produce plasmas with fewer ions, although their average charge states are higher.

At a fixed pump to fundamental delay of 100 ns, we have shown that highest-

order harmonics are more efficiently generated in plasmas pumped with Gaussian pulses. This effect is mostly visible for the shortest pump pulse durations and is attributed to the higher average charge state composition of the plasma. On the other hand, lower-order harmonics are most efficiently generated in plasmas pumped with a square-shaped pulse envelope and long pulse duration. This is attributed to the greater amount of low-energy ions with a lower average charge state. For this work, phase-matching effects from these plasma conditions have not been investigated.

Varying the delay between pump and fundamental pulses also results in a change of the overall shape of the generated HHG spectrum. Initially faster ions with higher average charge state enter the interaction zone, which generate the highest-order harmonics most efficiently. As the delay increases, lower-order harmonics are more efficiently generated from slower ions with lower average charge states. For delays greater than 150 ns, the plasma density decreases upon expansion, resulting in a slow decrease of signal strength for all harmonic orders. As future work, it would be interesting to explore the influence of phase matching in more detail. This could be achieved by varying interaction length, using e.g. spatially extended pump spots.

Acknowledgments

The authors thank Nik Noest for technical support, Lucas Poirier for his contribution to the RFA data analysis, and Dr. Aneta Stodolna, Dr. Tiago de Faria Pinto, Dr. Zeudi Mazzotta, and Amelie Heinzerling for their contribution to the development of the setup. This work has been carried out at the Advanced Research Center for Nanolithography (ARCNL), a public-private partnership of the University of Amsterdam, the Vrije Universiteit Amsterdam, the Netherlands Organization for Scientific Research (NWO) and the semiconductor equipment manufacturer ASML.

Declarations

Conflicts of interest The authors declare that they have no conflicts of interest.

4.A HHG spectra and harmonic yields for all varied parameters

Appendix containing plots of HHG spectra for the full parameter space of this work. Also, individual harmonic yields are plotted for the full parameter space.

4.A.1 Dependence on Pump Pulse Shape

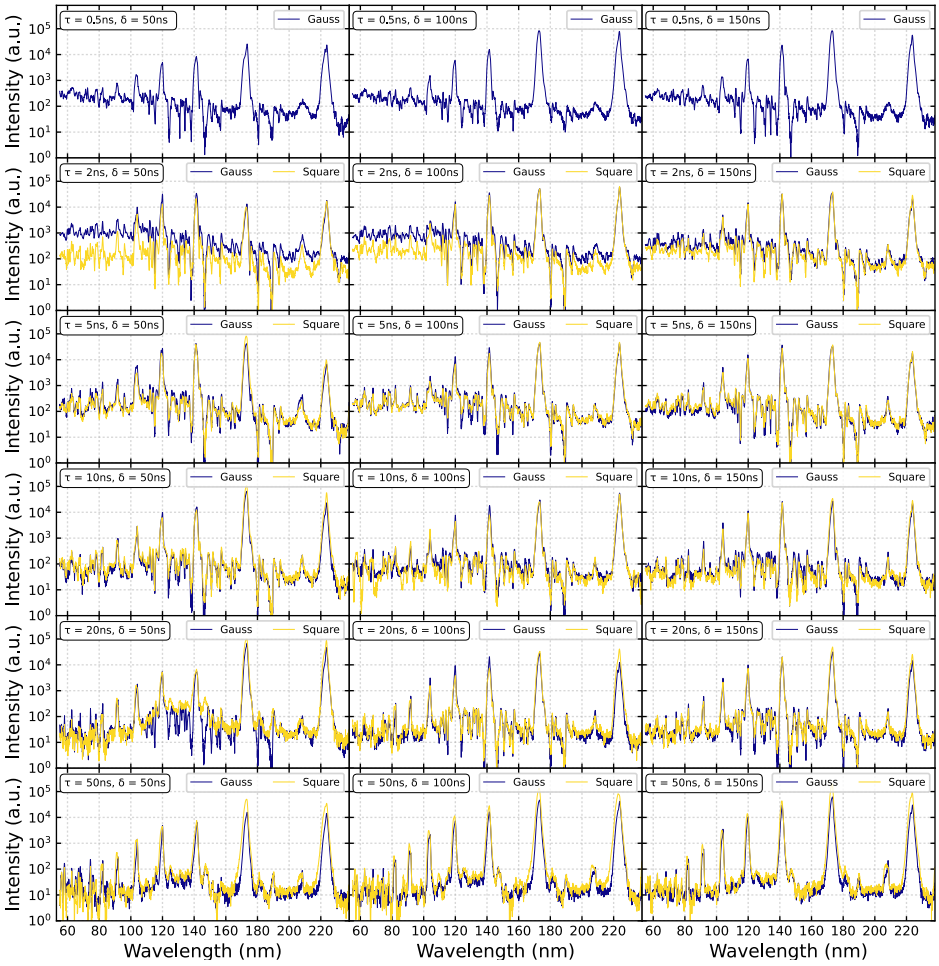

Figure 4.7: HHG spectra for complete parameter space comparing Gaussian (blue lines) and square (yellow lines) pump pulse envelope shapes. Pulse lengths τ and delays δ are indicated for each subplot, a.u. is arbitrary units.

4.A.2 Dependence on Pump Pulse Length

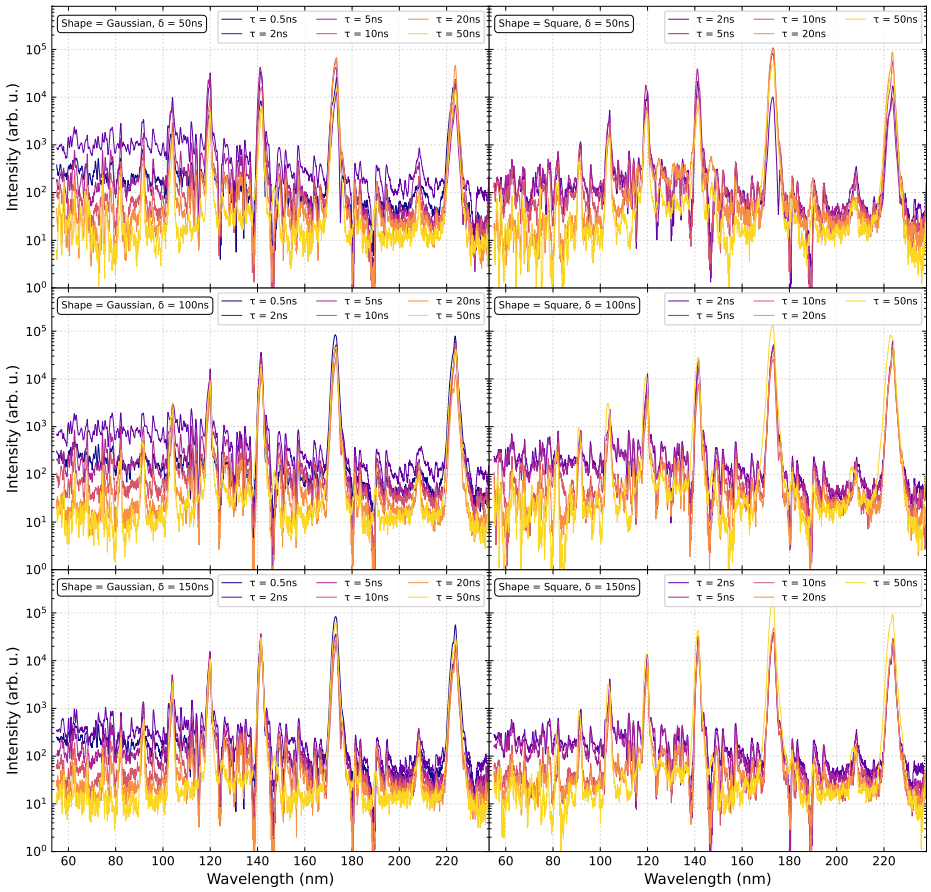

Figure 4.8: HHG spectra for complete parameter space comparing pump pulse lengths τ. Pump pulse envelope shape and delays δ are indicated for each subplot.

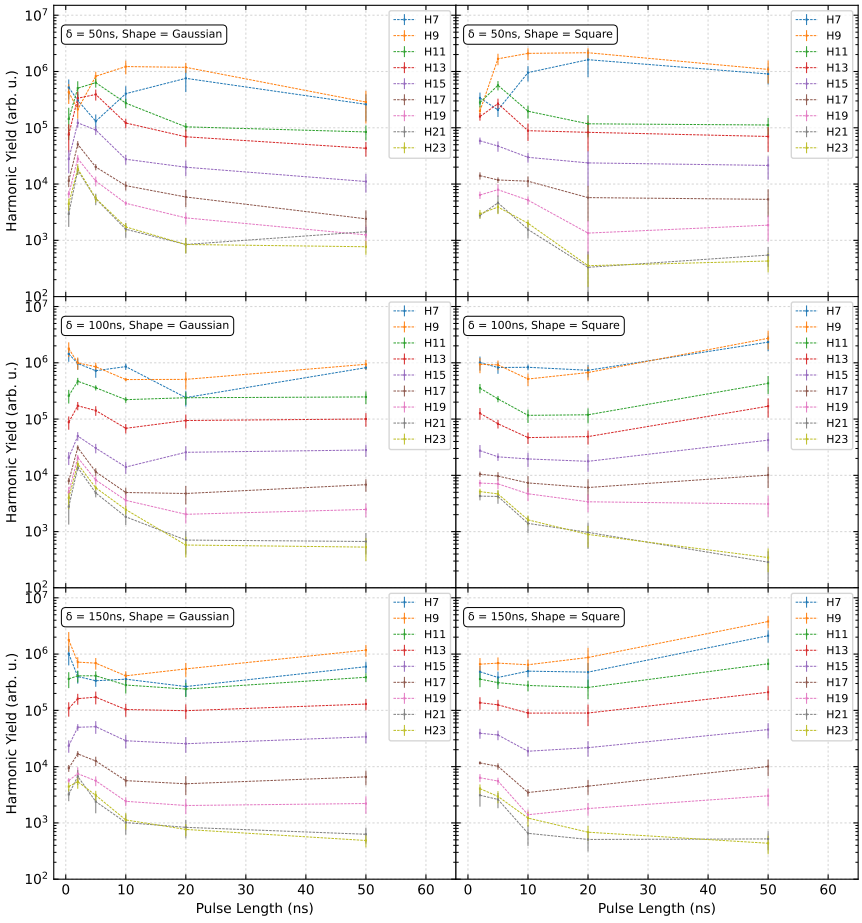

Figure 4.9: Individual harmonic yields as a function of pulse length. a), c), and e), harmonic yields generated in Gaussian-pumped plasmas with pump-to-fundamental delays of 50 ns, 100 ns, and 150 ns, respectively. b), d), and f), harmonic yields generated in square-pumped plasmas with pump-to-fundamental delays of 50 ns, 100 ns, and 150 ns.

4.A.3 Dependence on Delay

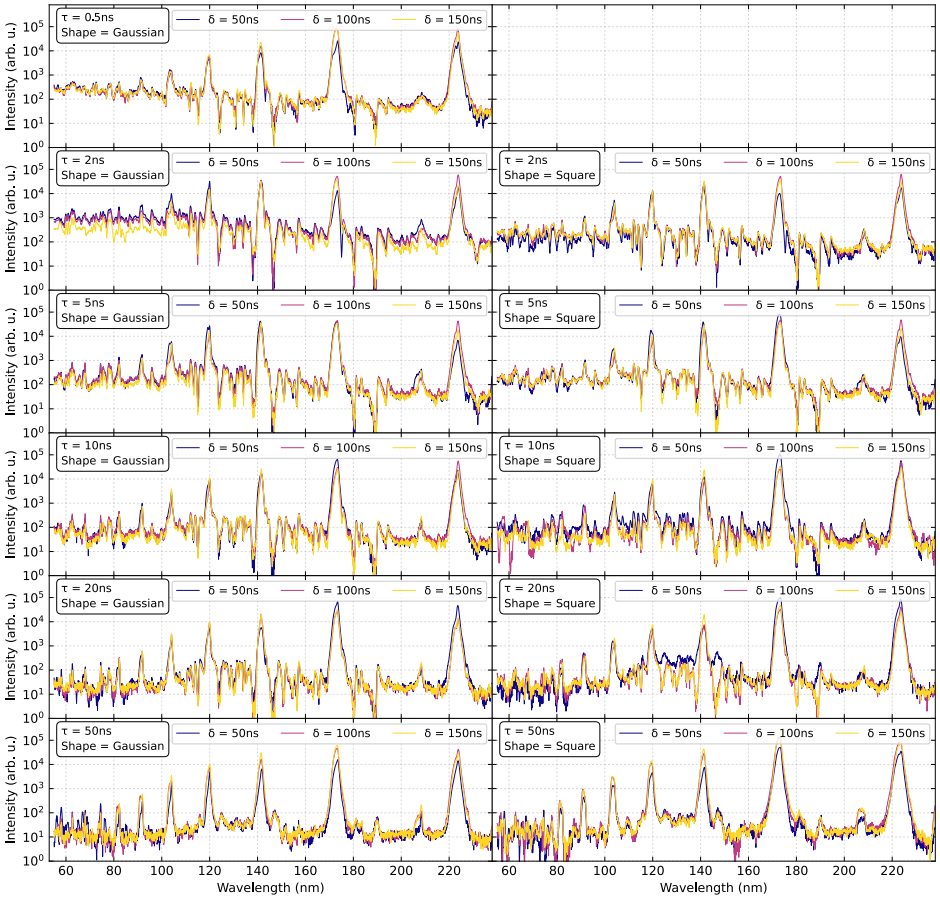

Figure 4.10: HHG spectra for complete parameter space comparing pump-to-fundamental delays δ. Pulse lengths τ and pump pulse envelope shape are indicated for each subplot.

Chapter 5

Sub-cycle dynamics in two-color high-harmonic generation from laser-produced plasmas

Abstract

We present high-order harmonic generation (HHG) in laser-produced aluminium and tin plasmas driven by a two-color field with orthogonal polarization, leading to the generation of both odd and even harmonics. We shape the effective drive field with sub-cycle resolution by controlling the phase between the fundamental wave and its second harmonic. The shape of the drive field influences the electron trajectories of the various harmonics generated in these plasmas. Here we focus on intermediate harmonic orders, with energies around the ionization potential of the target atoms. Clear oscillatory signals are observed in the HHG signals, with strongly harmonic-order-dependent modulation depth and oscillation phase. These results provide evidence for a significant influence of the Coulomb potential on the laser-driven electron trajectories in this spectral range.

This chapter has been published as [105].

5.1 Introduction: high-harmonic generation in laser-produced plasmas

High-order harmonic generation (HHG) is an effective method to generate coherent radiation in the extreme-ultraviolet (XUV) and soft-X-ray spectral ranges with a compact table-top setup (see e.g. [3, 5]). In HHG, an intense ultrashort laser pulse nonlinearly interacts with a medium, leading to the generation of new spectral components that typically appear as high-order harmonics of the driving laser frequency. While low-order harmonic generation [106, 107] was discovered and understood shortly after the invention of the laser, the observation of higher-order harmonics required a non-perturbative theory to be developed. This led to the concept of the three-step model [8, 108], in which electrons tunnel ionize from a ground-state atom, accelerate in the laser field, and recombine with the parent ion, leading to emission of a high-energy photon. The recurring nature of the process at every fundamental field half-cycle results in a train of attosecond light bursts [109], and the time-integrated spectrum consists of discrete harmonics.

Although the most basic version of the three-step model only considers an ionization potential, it was shown that atomic structure can have a significant impact on HHG spectra. The presence of atomic transitions near harmonic frequencies can result in strong resonance enhancement of specific harmonics [37, 38, 110], as well as absorption and spectral reshaping [33, 111]. Thus, the use of specific atomic species can have advantages for the generation of controlled XUV spectra, such as in producing quasi-monochromatic beams. While most HHG experiments employ inert gas-phase elements such as noble gases because of their high ionization potential, favourable transparency and ease-of-use, resonance-induced effects are more readily found in other elements such as metals. Such metallic elements then need to be converted to the gas phase at sufficient pressure to enable HHG, typically via laser-driven vaporization with an auxiliary pump pulse [111]. The resulting laser-produced plasma (LPP) can be used for HHG, while the pump laser parameters may provide an additional level of control [44].

For a single-wavelength laser field in an isotropic medium, the waveform of the subsequent generated light bursts at each half cycle is very similar, except for a π phase shift, causing only odd-order harmonics to be produced. By introducing an asymmetry between positive and negative half-cycles of the electric field, even-order harmonics can be generated as well. Experimentally such an asymmetry can be realized in anisotropic media, or optically by the addition of a laser field at twice the fundamental frequency [14, 112]. The addition of a second-harmonic (2ω) field therefore enables more harmonics to be produced in isotropic media. This option has been explored for LPP-based HHG, leading to the generation of even-order harmonics [46], resonance enhancement of these harmonics [113], as well as modified phase matching properties as a function of the two-color field parameters [43, 48, 114].

An interesting insight from Dudovich et al. was that such a 2ω field can actually be used as a temporal gate that selects specific harmonics [115]. Especially if the 2ω field is polarized perpendicularly to the fundamental field, it can control the recombination step in a time-dependent way [116], thus selecting electron

trajectories with specific energies as a function of the relative phase between the ω and 2ω fields. The interpretation of this attosecond gating mechanism is usually given in terms of the three-step model, where a weak 2ω field is expected to modulate the recombination step by spatially offsetting the electron with respect to the parent ion at the time of recombination [115]. This picture is found to work well for high-order harmonics in the plateau region, but in its basic form does not take the Coulomb potential of the atom or any other atomic structure into account. Extensions to the theory that include Coulomb effects have also been developed [117–119], leading to even better agreement with experimental determinations of the time delays and associated phase shifts on the harmonics. For lower-order harmonics however, such an interpretation can become questionable, as a classical electron trajectory at such low energies remains so close to the parent ion that the atomic potential should have a significant influence. The strong-field theory, also including Coulomb correction, calculates the action of the free electron in the continuum, which is not well defined for electron energies below the ionization potential. Therefore, application of such strong-field models to the presently studied HHG parameter range will lead to challenges. Two-color gating typically shows only weak phase dependence for plateau harmonics [112, 115], with an increasing effect towards the HHG cutoff energy where the electron trajectories qualitatively change [120].

In this paper, we present experimental results on a two-color HHG experiment in LPPs from aluminium (Al) and tin (Sn), in which we focus on the lower-order harmonics. We record HHG spectra as a function of the relative phase between perpendicularly polarized ω and 2ω fields. We observe significant oscillations particularly at the even-order harmonic frequencies, with significant variations in the relative phase of those oscillations between subsequent harmonics. Our results provide evidence that the sub-cycle electron dynamics at these harmonic frequencies are indeed significantly influenced by the atomic potential.

5.2 Theory: HHG in perpendicularly polarized two-color fields

As mentioned, a theoretical description of the HHG process is usually based on the three-step model [8, 108], which has been well established for harmonics with energies well above the ionization potential. However, at lower energies the influence of the atomic potential can be expected to have a significant influence on the electron trajectory, complicating such a model description. Therefore, we take a more phenomenological approach to describe the influence of the perpendicularly polarized two-color field on the HHG emission, based on the model introduced by He et al. [120] for parallel fields.

As a starting point, we assume that in a single-color field the HHG radiation is emitted in the form of short XUV bursts twice per IR cycle, over n cycles of the laser field (Fig. 5.1a). This results in the well known HHG spectrum with discrete odd harmonics spaced by 2ω (Fig. 5.1c). Adding a 2ω field with its polarization parallel to the ω field introduces an asymmetry in the combined field, leading

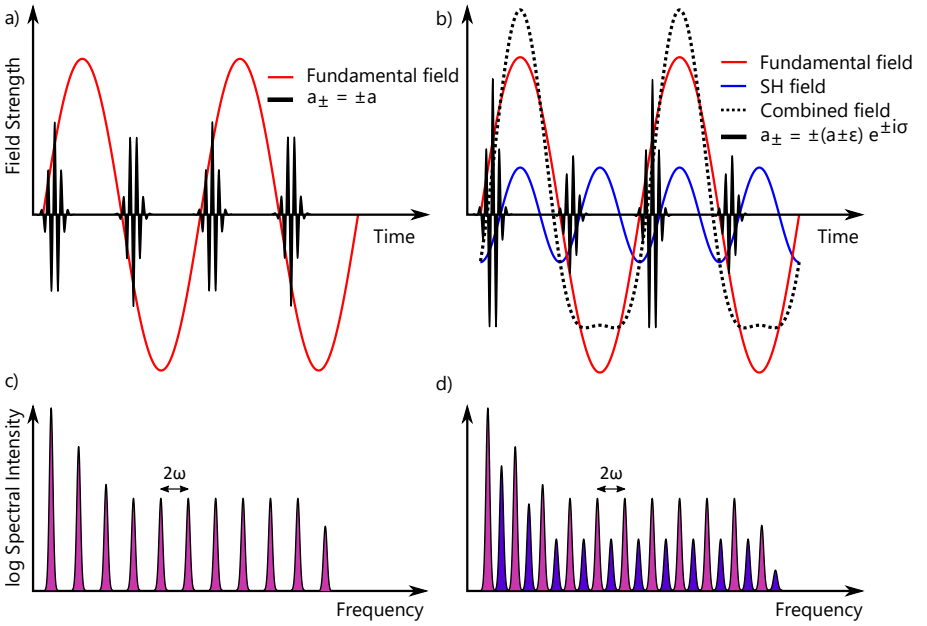

Figure 5.1: Schematic representation of XUV bursts generated by the HHG process. a) and b), time domain illustration for HHG ω and 2ω driving fields with a relative phase of $\pi/2$, respectively. The red curve shows the fundamental field, the blue curve represents its second harmonic and the black-dotted line shows the combined HHG driving field. Solid black pulses represent the $a_{\pm}$ XUV bursts. c,d), schematic drawings of resulting spectral HHG intensities driven by ω and 2ω fields, respectively. Odd harmonics are colored pink and even harmonics are colored purple.

to different amplitudes and phases for the XUV bursts of the first and second half cycles (Fig. 5.1b). Consequently, even harmonics (purple peaks in Fig. 5.1d) appear in the HHG spectrum. Extending this concept to two dimensions for orthogonally-polarized ω (polarized along $\hat{x}$) and 2ω (polarized along $\hat{y}$) driving fields, the XUV pulse trains in the $\hat{x}$ and $\hat{y}$ directions can be formulated as:

$$S_x(t) = \sum_{j=1}^{n} a_+(t) \otimes \delta(t - jT) + a_-(t) \otimes \delta(t - jT - \frac{T}{2})\hat{x}, \tag{5.1}$$

$$S_y(t) = \sum_{j=1}^{n} b_+(t) \otimes \delta(t - jT) + b_-(t) \otimes \delta(t - jT - \frac{T}{2})\hat{y}. \tag{5.2}$$

Here $a_+(t)$, $b_+(t)$, $a_-(t)$, and $b_-(t)$ are the XUV bursts emitted in the first and

second half IR cycles, and T is the period of the fundamental field. The magnitudes of $a_{\pm}(t)$ and $b_{\pm}(t)$ depend on the trajectory that the electron takes in the laser field. To understand the dependence of $a_{\pm}(t)$ and $b_{\pm}(t)$ on the relative phase φ between the two laser fields, it is instructive to visualize the electron motion in such a two-color field in the vicinity of an atom. Figures 5.2a,c show such trajectories for consecutive half-cycles of the fundamental field for a given phase φ between the two fields, in an atom with a p-wave ground state. Figures 5.2b,d show such trajectories for a different phase φ. From these trajectories, the relative signs of $a_{\pm}(t)$ and $b_{\pm}(t)$ can be inferred.

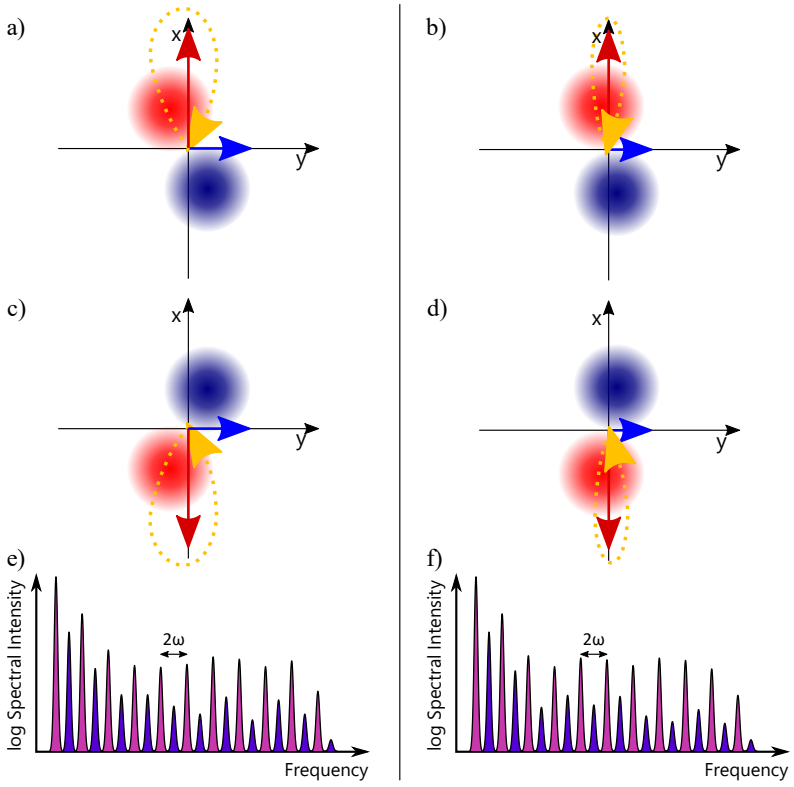

Figure 5.2: Schematic drawing of electron trajectories (orange paths) in a two-color field with perpendicular polarizations. The fundamental and second harmonic are indicated by red and blue vectors, respectively. a) Schematic trajectory for a given phase between the fields, in an atom with a p-orbital ground state. The initial motion is preferentially along the orbital axis (see text and [121]). b) Schematic electron trajectory for another relative phase between the fields. The motion through the atomic potential is different compared to the trajectory in a. c) Trajectory in the next half-cycle for the fields similar to a. d) Trajectory in the next half-cycle for the fields similar to b. e,f) Schematic drawings of the resulting HHG spectra. The relative intensities of the harmonics depend on the phase between the fields.

For a p-wave atomic wave function, initial electron motion and ionization preferentially occur parallel to the p-wave axis [121], which acts as a selection mechanism for atoms with a specific orbital alignment (which remains valid for atomic orbitals with different quantum numbers). The electron motion in the two-color field then results in a non-zero return angle with respect to the orbital, where the angle is influenced by φ. In the strong-field approximation, this can be interpreted as control over the recollision angle, and used for atomic state tomography [116]. More generally, even for lower electron energies the emitted harmonics can be seen as resulting from the interference of the returning electron wave with the ground state, described by a dipole matrix element $\mathbf{d} =< \psi_g|\mathbf{r}|\psi_{el} >$. The magnitude of this dipole at a given frequency determines the strength of the generated field, and the emission direction is perpendicular to the dipole. The projections of this dipole along the polarization directions of the fundamental and second-harmonic fields then give $a(t)$ and $b(t)$: $a(t) = \mathbf{d}\sin\theta$ and $b(t) = \mathbf{d}\cos\theta$, with θ the angle between the dipole and the fundamental polarization direction (the x-axis in Fig. 5.2). In a non-centrosymmetric atomic potential, the two-color field leads to a complex electron trajectory and in general a nonzero return angle with respect to the ground-state orbital, influencing $\mathbf{d}$ and making it dependent on the phase φ. The mirror symmetry (neglecting carrier envelope phase changes and ionization effects) between consecutive half-cycles (compare Figs. 5.2a,c) ensures that $a_+(t) = -a_-(t) = \pm a(t,\varphi)$ and $b_+(t) = b_-(t) = b(t,\varphi)$, where in the latter case no sign change takes place because the driving field in the y-direction is the second harmonic.

With this conceptual understanding of the generation mechanism, a description of the resulting harmonic fields in the spectral domain can be obtained by Fourier transforming Eqs. 5.1 and 5.2, resulting in:

$$S_x(\Omega,\varphi) = \hat{x}A(\Omega,\varphi)\sum_{j=1}^{n} e^{ij\Omega T} - e^{ij\Omega T + i\frac{\Omega T}{2}}, \tag{5.3}$$

$$S_y(\Omega,\varphi) = \hat{y}B(\Omega,\varphi)\sum_{j=1}^{n} e^{ij\Omega T} + e^{ij\Omega T + i\frac{\Omega T}{2}}, \tag{5.4}$$

where $A(\Omega,\varphi)$ and $B(\Omega,\varphi)$ are the Fourier transforms of $a(t,\varphi)$ and $b(t,\varphi)$. The resulting spectral intensity of the HHG radiation in the $\hat{x}$ and $\hat{y}$ directions can then finally be expressed as:

$$|S_x(\Omega,\varphi)|^2 = 4|A(\Omega,\varphi)|^2 \cdot \left|\frac{\sin(\frac{n\Omega T}{2})}{\sin(\frac{\Omega T}{2})}\right|^2 \cdot \sin^2(\frac{\Omega T}{4}), \tag{5.5}$$

$$|S_y(\Omega,\varphi)|^2 = 4|B(\Omega,\varphi)|^2 \cdot \left|\frac{\sin(\frac{n\Omega T}{2})}{\sin(\frac{\Omega T}{2})}\right|^2 \cdot \cos^2(\frac{\Omega T}{4}). \tag{5.6}$$

The $A|(\Omega,\varphi)|^2$ and $|B(\Omega,\varphi)|^2$ terms in these equations describe the spectral intensity of the emitted harmonics at frequencies $\Omega = q\omega$. The second term represents a comb of both odd and even q harmonics. As the number of laser cycles n increases, the width of the comb peaks decreases, reflecting the temporal coherence properties of the pulse train. The last term acts as a modulation on the harmonic spectrum, which has the effect of cancelling the even harmonics in $|S_x|^2$ and the odd harmonics in $|S_y|^2$. Thus, the odd harmonics are polarized in the direction of the fundamental beam and the even harmonics are polarized along the direction of the second harmonic. Given the dependence of $|S_x|^2$ and $|S_y|^2$ on the phase φ between the fundamental and second-harmonic fields, we can expect intensity modulations of the harmonics with a period corresponding to half of a second-harmonic field cycle. The relative intensity of the second harmonic pulses in the current experiment is limited to 1% of the fundamental pulse energy. Hence, we expect the second harmonic field to act as a perturbation to the fundamental field, resulting in a spectrum with strong odd and weak even harmonics. Furthermore, in our HHG spectrometer (see next section) we cannot determine the polarization state of the harmonics. The relative phase φ between the fundamental and second-harmonic fields is controlled by changing the difference in optical path length $\Delta\Lambda$ for the two wavelengths, which in our experiment are 1560 nm for the fundamental and 780 nm for the second harmonic. A phase shift of 2π therefore corresponds to a difference in path length of 390 nm, i.e. $\varphi/2\pi = \Delta\Lambda/390\,nm$. We then expect to observe harmonics that vary in intensity according to the following relation:

$$I_H(\Delta\Lambda) = A_H \cdot \sin^2\left(\frac{\pi\Delta\Lambda}{390\,nm} + \frac{\phi_H}{2}\right) + O_H. \tag{5.7}$$

Here, A_H is the modulation depth of harmonic H, ϕ_H is its phase offset, and O_H is the intensity offset. In this equation, we have set the oscillation period to correspond with an optical path length difference $\Delta\Lambda$ of half the second-harmonic wavelength.

For plateau harmonics well above the ionization potential, which are well described by the strong-field approximation, such modulations are only weakly dependent on harmonic number [115, 120]. In the lower-energy regime considered here, it can be expected that the atomic potential will have a significant influence on the electron motion at different energies. Therefore, the optimum intensity of each harmonic may vary more strongly with phase φ.

5.3 Experimental setup for plasma-based two-color HHG

A schematic overview of the experimental setup is shown in Fig. 5.3. The vacuum system consists of a target chamber where the HHG process takes place, and an EUV spectrometer. A target for plasma generation and HHG is positioned in the experimental chamber. Pump pulses with a duration of 0.43 ns and an energy up to 4 mJ are sent onto this target under normal incidence, creating an expanding LPP. After a certain delay, pulses from the fundamental beam (central wavelength = 1560 nm, energy = 0.5 mJ, pulsewidth = 200 fs) are then sent through this LPP in a direction parallel to the target surface, generating the high-order harmonics within the plasma. The intensity at the focus is estimated to be 0.8×10^{14} W/cm^2. The toroidal mirror in the spectrometer images the HHG spot onto an EUV-sensitive camera. The HHG radiation is spectrally dispersed with a transmission grating with a groove density of 1000 mm^{-1}, after which the 1st diffraction order is resolved on the EUV camera. The grating also acts as an aperture to the HHG beam, blocking parts of the beam with higher divergence such as long trajectories for above-threshold harmonics. The 0th and -1st orders are blocked with a beam dump to prevent scattered signal and damage of the EUV camera. The laser systems used to generate the pump and HHG pulses have been described in detail previously [51, 88].

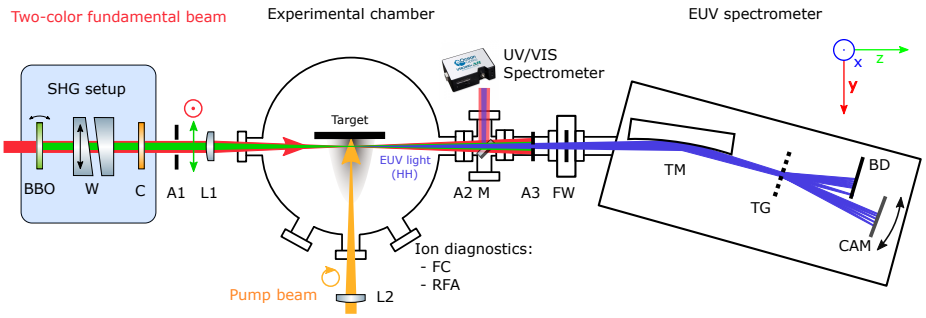

Figure 5.3: Schematic image of the experimental setup. At the bottom and left side, the pump laser and the HHG driving laser with the SHG setup are depicted, respectively. The right side of the schematic shows the experimental chamber in which the high harmonics are generated and the EUV spectrometer. Laser parameters for these experiments were set as follows: pump pulse length: 0.43 ns, pump pulse energy = 2 mJ, fundamental pulse length = 200 fs, fundamental pulse energy = 0.5 mJ, second harmonic energy up to 5 µJ, polarization states are indicated with the respective arrows. Optical components: BBO: nonlinear crystal for frequency doubling, W: UV fused silica wedges, C: calcite plate, A: Aperture, L1: f = 300 mm lens, L2: f = 1000 mm lens, M: insertable mirror, FW: filter wheel, FC: Faraday cup, RFA: retarding field energy analyser, TM: toroidal mirror, TG: transmission grating, BD: beam dump, CAM: EUV camera.

A second-harmonic generation (SHG) stage has been implemented in front of the target chamber, enabling phase-controlled two-color HHG experiments [15, 112, 115, 116]. The SHG stage contains a 200 µm thick type-I BBO crystal cut at $\theta = 19.8°$. The ratio between SHG and fundamental energy can be tuned via the phase matching angle. The relative phase between the fundamental and second harmonic is controlled with a pair of fused silica wedges. Varying the inserted amount of glass results in a wavelength-dependent path length difference $\Delta\Lambda = \Delta n \Delta x \tan\Phi$, where Δx is the transverse wedge displacement and $\Phi = 5°$ is the apex angle of the wedge pair. For UV fused silica, the refractive index difference between the fundamental and its second harmonic $\Delta n = n_{1560} - n_{780} = -0.0098$ [122]. This results in a path length difference of $\Delta\Lambda = 857$ nm per millimeter wedge displacement. A delay of half a second-harmonic cycle – which is the expected periodicity of the oscillations – is thus achieved by shifting the wedge by 455 µm. Accurate path length variation is performed by mounting one of the wedges on a high-accuracy linear piezo-stage (Smaract, model number SLC1760). As the focusing lens and the vacuum viewport also add a time delay due to their group-delay mismatch between fundamental and second harmonic, some additional group-delay compensation is needed to maximize temporal overlap at the plasma. This compensation is achieved with a 1.7 mm thick calcite plate, cut at an angle of $\Theta = 55°$, inserted in the two-color beam. Initial alignment optimization was done by maximizing the sum-frequency generation signal of the two colors produced in another BBO crystal, positioned behind all optical components of the beamline to best mimic experimental conditions. However, as the driving pulses for this experiment are on the long side, the optimum phase matching for the HHG process likely occurs mainly in the leading edge of the fundamental pulse. Therefore, final optimization of the temporal overlap is done by maximizing the signal of the even harmonics measured under typical experimental conditions.

The pump pulse energy for the Al targets was set at 4 mJ while Sn targets were irradiated by pump pulses with energies of 2 mJ, since those parameters lead to the highest signal yield for these materials. The focal spot size of the pump laser on the target is measured to be 450 µm (e^{-2} diameter). The delay between the pump and fundamental pulses has been set to 100 ns. The fundamental pulse length was measured to be 200 fs. Its energy has been limited to 0.5 mJ, to reduce noise originating from stray light of the second harmonic on the EUV camera, as the Si chip of this camera is highly sensitive to this wavelength. To further suppress this stray light, a polarization scheme with vertically polarized fundamental and horizontally polarized second harmonic has been utilized to reduce the second harmonic reflection efficiency of the toroidal mirror. An unfortunate consequence of this polarization setting is that the even harmonics generated in the experimental chamber also experience a sub-optimal reflection on the toroidal mirror, resulting in an underestimation of the intensity ratio of even and odd harmonics. Based on the optical properties of the boron carbide coating on the toroidal mirror, the strength of the 6^{th} harmonic (H6) is likely underestimated by a factor four, while H12 is likely underestimated up to a factor two. We do not compensate for these effects in the data processing, and present

the measured harmonic yield after only static background correction.

For the experiments on Sn, we have scanned the wedge position over 630 µm, corresponding to 0.69 optical cycles of the second harmonic. These measurements were carried out with 5 µJ second harmonic energy, corresponding to a 1% intensity ratio between fundamental and second harmonic. For the Al experiments, we have performed measurements at SHG energies of 0.5 µJ, 2.0 µJ and 5.0 µJ. At the highest energy, we carried out a longer phase scan covering nearly 1.4 optical cycles of the second harmonic.

5.4 Results: phase-dependence in two-color HHG

5.4.1 Typical Harmonic spectra for Al and Sn

Typical HHG spectra measured in Al and Sn plasmas are shown in Figures 5.4 and 5.5, respectively. Both spectra are acquired under identical HHG driving conditions ($E_\omega = 0.5\,\mathrm{mJ}$, $E_{2\omega} = 5\,\mu\mathrm{J}$, 100 ns delay between pump and fundamental). The aluminium and tin targets are pumped with 4 mJ and 2 mJ, as aluminium targets require more energy to ablate. The spectrometer is set to cover a wavelength range between 115 nm and 295 nm. Harmonics 6 up to 13 are contained within this spectral region. The corresponding peaks are marked

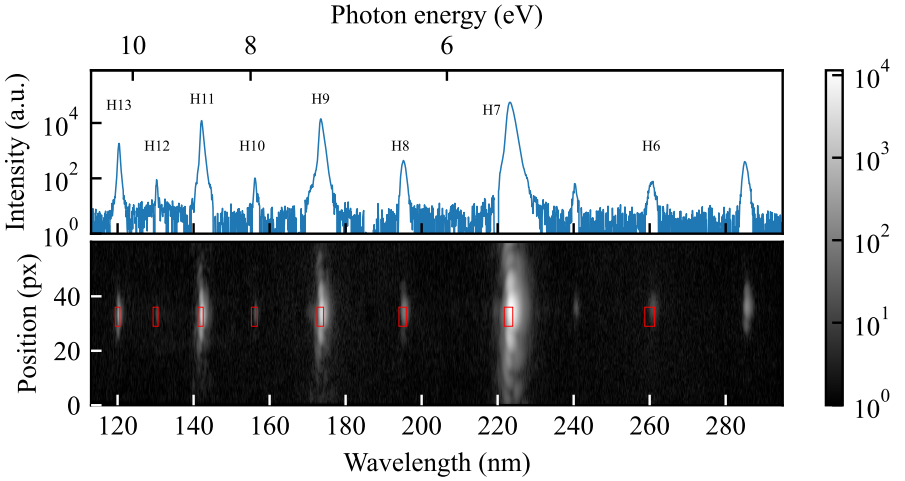

Figure 5.4: Typical HHG spectrum generated in Al plasma, driven by the two-color fundamental field. The bottom panel shows the measured camera image of the HHG generated in the Al plasma. Red rectangles indicate integration areas for individual harmonic yields used in the data analysis for Fig. 5.7. The top panel shows the vertically integrated spectrum of the bottom panel, a.u. is arbitrary units. The ionization potential of Al is 5.98 eV.

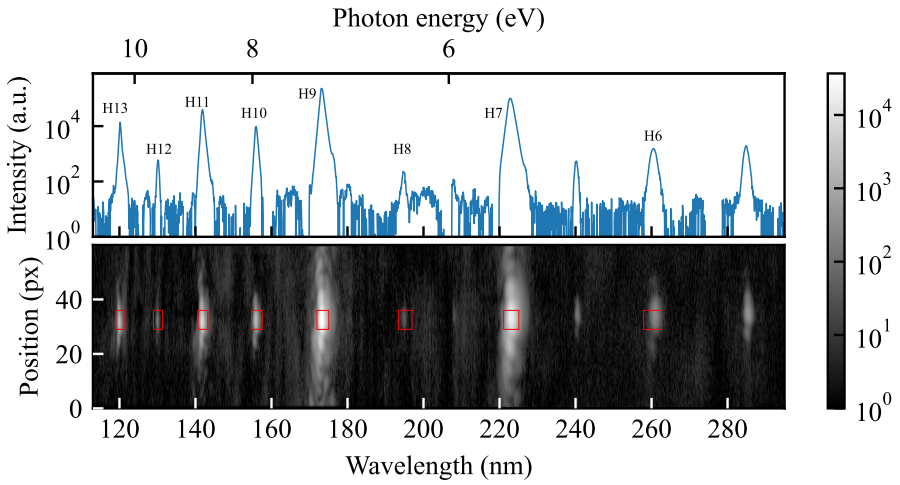

Figure 5.5: Typical HHG spectrum generated in Sn plasma, driven by the two-color fundamental field. The bottom panel shows the measured camera image of the HHG generated in the Sn plasma. The red rectangles indicate integration areas for individual harmonic used in the data analysis for Fig. 5.8. The top panel shows the vertically integrated spectrum of the bottom panel, a.u. is arbitrary units. The ionization potential of Sn is 7.34 eV.

in the plotted spectra. The additional peaks appearing at wavelengths 210 nm, 240 nm and 285 nm result from second order diffraction of harmonics 15, 13 and 11, respectively.

To assess the harmonic yield, the detected signal is averaged over a region of interest (ROI) around each harmonic peak, indicated by the red rectangles in Figs. 5.4 and 5.5. Note that due to a small rotation of the transmission grating, harmonic 6 in the aluminium spectrum is off-center with respect to the selected ROI, underestimating its strength slightly. This does not influence the detection of oscillatory signals as discussed later, although the signal to noise ratio is somewhat decreased. From these two figures, we observe a higher spectral intensity for nearly all the harmonics generated in a tin plasma, compared to the aluminium HHG spectrum. However, harmonics 7 and 8 are generated less efficiently in the tin plasma. Similar trends in the intensity of the odd harmonics have been observed before [89]. The near absence of harmonic 8 in the tin HHG spectrum is surprising, especially since all other even harmonics up to order 12 are much brighter. From the present set of measurements it is not clear whether to attribute this to the single atom or ion response, or to differences in phase-matching conditions in the two LPPs. Further experiments involving controlled changes to the phase-matching conditions, e.g. by varying the interaction length, could provide further insights to this matter.

5.4.2 Influence of second harmonic energy

Figure 5.6a shows the generated HH spectra from aluminium plasmas upon increasing the strength of the second harmonic while keeping the fundamental beam energy constant. Note that the temporal overlap of fundamental and second harmonic pulses may be sub-optimal for the 0.5 µJ and 2 µJ second harmonic energies, as this has been optimized only for the 5 µJ second harmonic energy data. However, given the long duration of the fundamental pulses, this sub-optimal temporal overlap will not significantly alter the resulting HHG spectra. The absolute phase difference between the fundamental and its second harmonic have not been experimentally verified in this experiment as we are mainly interested in the behaviour for relative phase changes. The spectra in Fig. 5.6a are averaged over a range of wedge displacements corresponding to half an optical cycle of the second harmonic. Figure 5.6b shows the harmonic yield of the different even harmonics integrated over a 1% spectral bandwidth.

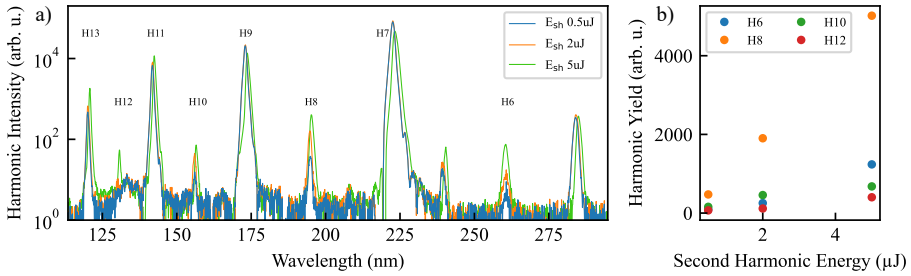

Figure 5.6: a) High-harmonic spectra generated in Al plasma. Different curves correspond to different second-harmonic energies. b) Harmonic yields of even harmonics as a function of second-harmonic energy.

Figure 5.6a shows an increase in harmonic intensity for both odd and even harmonics when increasing the second harmonic energy from 0.5 µJ to 2 µJ. For the odd harmonics, this effect seems strongest for the highest-order harmonics detected. The signal increase for the even harmonics is most pronounced for central harmonics 8 and 10. Further increasing the second harmonic energy up to 5 µJ results in a lower intensity for odd harmonics 7 and 9, while all other harmonics are generated with a higher efficiency. This decrease might in part be attributed to slight changes in optical alignment between these two data sets, which have slightly decreased the generation efficiency of H7 and H9, while the increased presence of the second harmonic leads to stronger even harmonic signals due to the greater drive field asymmetry. Furthermore, the angle of the calcite plate has been tilted by 14° between the acquisition of the lowest two energies data set and the $E_{\mathrm{SH}} = 5\,\mu\mathrm{J}$ data set to re-optimize even-order harmonic generation. For that reason, the direct comparison between these to data sets is not trivial. Nonetheless, the even-order harmonic yield grows linearly with increasing second-harmonic energy. Additionally, the stronger presence of the

second harmonic favorably increased the phase-matching conditions to generate higher-order harmonics with higher efficiency. In contrast to the situation with parallel polarization, for which the ionization rate can increase strongly due to the second-harmonic field, our scheme with perpendicular polarization does not lead to significant changes in ionization rate. This explains the limited effect of the SHG field on the yield of the odd harmonics and overall yield.

5.4.3 Phase-dependence of HHG in Al and Sn

Figure 5.7 shows the yield of all harmonics as a function of the relative phase between the fundamental and its second harmonic in aluminium. Figure 5.7a shows the individual harmonic yields integrated over the respective ROIs indicated in Fig. 5.4 on a logarithmic scale after the subtraction of background noise (explained in detail previously in [89]). Note that the absolute phase difference is not calibrated in these measurements. Instead, we measure harmonic signal fluctuations as a function of path length difference $\Delta\Lambda$. As a function of $\Delta\Lambda$, clear oscillatory behavior is observed for the even harmonics. To further visualize

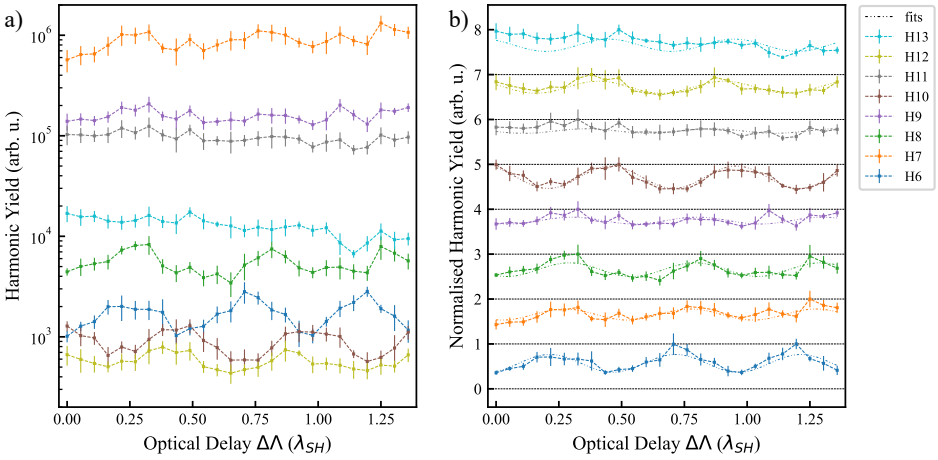

Figure 5.7: Individual harmonic yields generated in the Al plasma as a function of relative phase between fundamental and second harmonic. a) Harmonic yields plotted on a logarithmic scale. b) Normalized harmonic yields plotted on a linear scale, and the traces are shifted vertically and sorted by increasing harmonic order for clarity.

this oscillatory behavior, we have individually normalized these harmonic yields and plotted them with a vertical offset and sorted by increasing harmonic order (for clarity) in Fig. 5.7b. The dash-dotted lines are fits to the model of Eq. 5.7, containing the expected oscillation period for the two-color fields. As the fits are in good agreement with the data, we can confidently state that these oscillations are actually the result of sub-cycle effects in the HHG process. The harmonics clearly oscillate with distinct phases, indicating differences in their electron trajectories.

The extracted oscillation phases of the harmonics generated in Al are plotted in Figure 5.9a. Within the spectral range of these few harmonics, we observe a strong shift in oscillation phases of these harmonics. The harmonic oscillations shift their phases nearly linearly with emitted photon energy. A total phase difference of 0.94π is measured between lowest-order harmonic 6 and highest-order harmonic 13. However, harmonic 10, which shows the most clear oscillation signal, shows a jump in its oscillatory phase compared to the other harmonic orders. The measurements using an Sn target lead to similar results, as displayed in Fig-

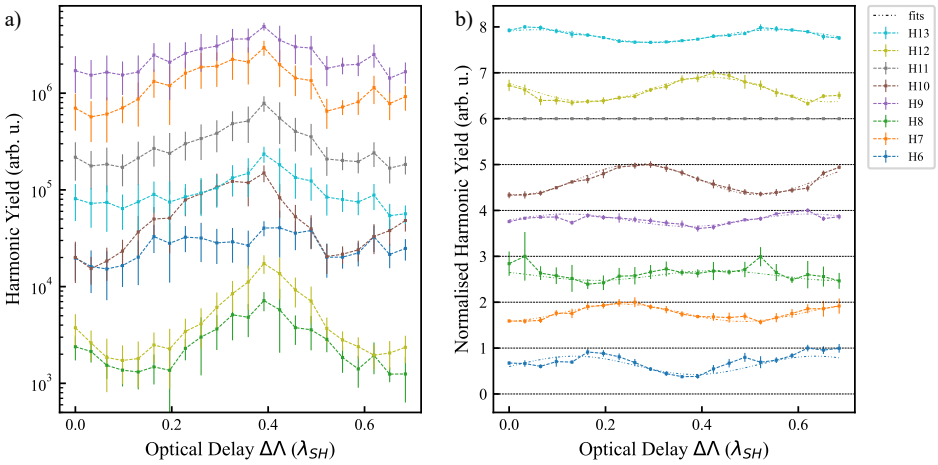

Figure 5.8: Individual harmonic yields generated in the Sn plasma as a function of relative phase between fundamental and second harmonic. a) Harmonic yields plotted on a logarithmic scale. b) Normalized harmonic yields plotted on a linear scale. To remove sample-induced intensity variations from the measurement, every trace is divided by the yield of H11 after which the traces are individually normalized. Traces are shifted vertically and sorted by increasing harmonic order for clarity. For Al, only even-order harmonics are shown, as the odd-order harmonics did not show clear oscillations.

ure 5.8. As with the aluminium dataset, the left panel displays the harmonic yield for harmonic orders 6 to 13 with respect to the path length difference $\Delta\Lambda$, plotted on a logarithmic scale. For this dataset, the sub-cycle effects are not obviously visible in this raw data, as HHG intensity variations introduced by a slight curvature of the tin target obscures the oscillations of the harmonic intensities. For this reason, we have divided the results of Figure 5.8b by the harmonic yield of harmonic order 11 before the individual normalization. Here we have chosen harmonic order 11 to be our reference as its intensity is bright and its photon energy lies reasonably well above the first ionization potential of tin. Hence, we would not expect significant phase-dependent oscillations for this harmonic, making it a suitable reference signal to calibrate systematic intensity variations across the scan from other sources than the sub-cycle phase. Again, the harmonic yields are offset vertically for clarity. After this normalization, it becomes apparent that nearly every harmonic order is indeed oscillating with respect to the path length

difference $\Delta\Lambda$. Only the oscillatory signal from harmonic 8 is less well defined due to a low signal-to-noise ratio, as is also apparent from Figure 5.5. Again, the oscillation period matches with the expected path length variation of 390 nm, providing evidence of the presence of sub-cycle effects in the HHG process. Even more so compared to the aluminium case, harmonics generated in tin oscillate at very distinct phases. The fitted phases of the tin harmonic signals are plotted in Figure 5.9b. The fitted phase differences between adjacent harmonic orders vary from 1 radians up to multiple radians in this spectral range. Furthermore, no clear trend can be observed to describe the relation between the fitted phase and the harmonic order.

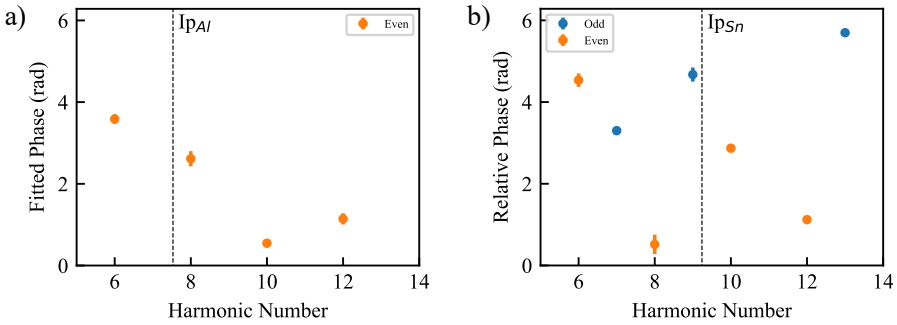

Figure 5.9: Fitted phases for the harmonic orders generated in a) Al plasmas and b) Sn plasmas. The right panel misses a data point at harmonic order 11, as the harmonic yields for these data are taken relative to this harmonic, resulting in a constant signal strength. The ionization potentials of the elements are indicated by vertical dashed lines.

5.4.4 Pump-induced background fluorescence

In addition to the HHG radiation produced in aluminium and tin LPPs, we have also measured the pump-induced background fluorescence for both of these plasmas with the EUV spectrometer in the same spectral region as the measured harmonics. These fluorecence backgrounds have been measured in the absence of the fundamental beam and its second harmonic. The measured aluminium and tin emission spectra are plotted in Figure 5.10a and b, respectively. To assess possible overlap of absorption or emission lines with the HHG spectrum, blue markers indicate the wavelengths of the harmonics. The wavelengths corresponding to the ionization potentials of aluminium and tin have also been indicated within the plots. Finally, we have plotted cumulative spectra for various charge states of aluminium and tin in Figures 5.10a and b, obtained from the National Institute for Standards and Technology (NIST) Atomic Spectra Database [97]. Note that this database contains multiple sources with non-identical experimental conditions and normalization methods. For that reason, we have selected

data that best match our recorded spectra, which are plotted as colored dashed lines. For the aluminium LPP spectrum, mostly ion emission from Al II and Al

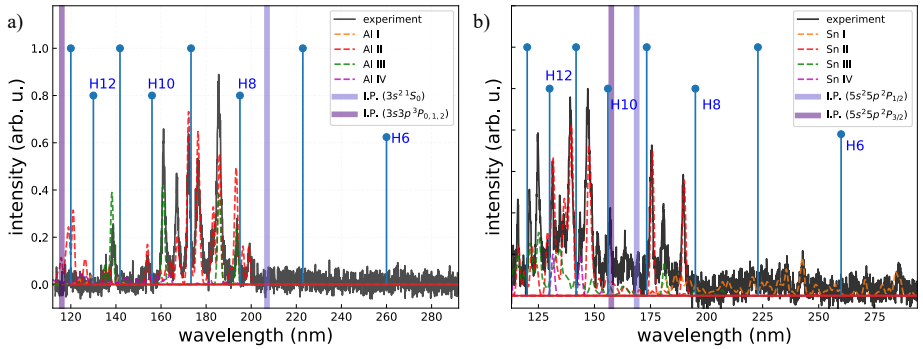

Figure 5.10: Emission spectra of individual charge states overlaid onto experimental background plasma emission spectra of a) aluminium plasma , and b) tin plasma. Colored dashed lines represent cumulative EUV emission spectra obtained from the NIST database for line emission [97]. Black solid lines represent experimentally measured background plasma emission. Blue pins correspond to wavelengths of high-order harmonics. Blue vertical stripes correspond to ionization potentials of Al and Sn.

III is observed. The cumulative NIST spectrum for Al II and Al III matches the emission profile quite well. However, some lines of the measured LPP emission are brighter or dimmer compared to the NIST spectrum. Especially the lines around 138 nm and 195 nm seem to lack intensity. This might be attributed to a changing charge-state composition in the plasma due to its expansion into the vacuum chamber [123], as the EUV camera integrates signals for all 157 pump pulses in a single exposure.

The composite NIST spectrum for the tin LPP also matches the experimentally obtained EUV spectrum quite well. This verifies the presence of Sn I, Sn II, Sn III and Sn IV species in the expanding plasma plume. Similar to the Al plasma spectrum, small discrepancies with the absolute intensities of individual lines are observed. Again, these differences between experimental and NIST spectra might originate from different temperatures of the LPP due to its expansion in the vacuum chamber.

5.5 Discussion

From the obtained results we conclude that our HHG data contains effects due to subcycle dynamics in the different atomic species. To the best of our knowledge, this is the first observation of such dynamics in an LPP. In our experiments, we have limited the energy of the second harmonic to 1% of the fundamental, resulting in oscillating harmonic signals rather than completely switching har-

monics on and off. In this configuration, we generate HHG spectra containing both odd and even harmonics. The even harmonic signal is roughly two orders of magnitude lower than the odd harmonic signal. Interestingly, for the HHG signal produced in Al, the even harmonic with the highest yield is harmonic 8, see Fig. 5.4, while this harmonic is actually the weakest in the case of HHG in tin, see Fig. 5.5. In the case of tin, all other harmonic orders appear stronger compared to the aluminium case.

Unlike the more commonly studied high-energy plateau regime where the strong field approximation holds [112, 115, 116, 120, 124, 125], our present two-color HHG measurements in the low-order regime where the Coulomb potential cannot be neglected show different and interesting results between the two-color phase and the resulting HHG radiation. For HHG in aluminium, the even harmonics show oscillations as a function of path length difference $\Delta\Lambda$. This clearly indicates that indeed the dipole moment $\mathbf{d} =< \psi_g|\mathbf{r}|\psi_{el} >$ depends on the relative phase φ. From Figure 5.9a, it becomes clear that all even harmonics have a different relative phase ϕ_H, showing the dependency of the dipole moment $\mathbf{d}$ on harmonic frequency Ω. Interestingly, the odd-order harmonics do not seem to oscillate as a function of $\Delta\Lambda$. This might be due to a limited signal to noise ratio, or due to a smaller dependency of the dipole moment $\mathbf{d}$ on the relative phase φ, as our second harmonic acts as a small perturbation on the fundamental beam. From these limited points, the exact relation between these relative phases ϕ_H is still unclear, although there seems to be a decreasing trend for increasing harmonic number.

Clear oscillatory behavior is also observed for HHG in tin plasmas, although the signal to noise ratio for harmonic order 8 is too low for an accurate fit to Eq. 5.7. From the distinct phases observed for all other harmonics, we conclude that the normalization by harmonic 11 has not influenced the individual oscillations. Therefore, HHG in tin plasmas also shows a dependence of the dipole moment $\mathbf{d}$ on the relative phase φ, as well as the harmonic frequency Ω. In contrast to the Al case, for HHG in tin plasmas both odd and even orders oscillate as a function of $\Delta\Lambda$. Even more so compared to the aluminium data, the relative oscillation phase of individual harmonics ϕ_H for HHG in tin shows large differences for neighbouring harmonic orders, indicating a more pronounced effect of the Coulomb potential on the resulting HHG radiation.

Regarding any effects of resonant enhancement of specific harmonic-orders, harmonic-order 8 in the aluminium HHG spectrum is notably stronger than the other even harmonics, and its wavelength is close to an Al II emission line. However, harmonic order 10 is also close to an emission line from Al II, and is not particularly bright compared to harmonic order 12. Hence, we can not conclude a clear correlation between the ion emission spectrum and an enhanced HHG signal. For tin, harmonic order 10 in the HHG spectrum is stronger compared to the other even harmonic-orders while it lies close to the Sn $5s^25p^2P_{3/2}$ ionization potential. Because Fig. 5.9b shows no clear trend for the oscillation phases of the harmonics, it is not possible to take the phase of harmonic-order 10 as an indicator for the presence of a resonant effect.

The results suggest that it would be beneficial to perform further experiments

with shorter drive pulses, in order to extend the generated harmonic spectrum to shorter wavelengths. This would allow resonance-enhanced HHG for specific harmonics, like 47 nm in tin LPPs [110]. Combining such a measurement with a phase-controlled two-color drive laser would provide concrete data on the influence of a specific auto-ionizing state on the accumulated phase of the HHG trajectory. Furthermore, a transition from a present, low-order regime where the Coulomb potential is important, to the better-known high-energy plateau regime might be found by examining a broad spectral range covering both low-order harmonics and high-order harmonics.

5.6 Conclusion

We have successfully generated high harmonics driven by a phase-controlled, two-color field with a fundamental wavelength at 1560 nm and its second harmonic at 780 nm in both aluminium and tin LPPs. Similar to the observed HHG spectral variation of odd harmonics generated in different media [89], the even harmonics generated in aluminium and tin also show clear differences in spectral intensity with identical driving fields. Upon increasing the second harmonic energy relative to the fundamental energy, the generation of even harmonics becomes more prominent as the second harmonic breaks the symmetry between the first and second half cycles of the fundamental wave.

Scanning the delay between the ω and 2ω fields gives rise to sub-cycle effects in the generation mechanism, resulting in the experimentally observed oscillations in the HHG signals. For aluminium, these oscillations are mostly observed for the even harmonic-orders. Tin HHG spectra show oscillating signals for both odd and even harmonic-orders. These oscillations have different amplitudes and phases for all generated harmonics. No clear relation between these phases and the harmonic frequency Ω can be extracted from these data, as neighboring harmonics show large jumps in oscillation phases. This suggests that the electron trajectories of the low-order harmonics observed in our experiment are not solely influenced by the electric field of the driving field, as is commonly assumed in the high-energy plateau regime where the strong field approximation holds. Instead, our measurements provide interesting results in the low-energy regime where the atomic Coulomb potential cannot be neglected in the electron acceleration phase of HHG, resulting in the strongly varying oscillation phases for individual harmonics.

Acknowledgments

The authors thank Nik Noest for technical support, and Dr. Aneta Stodolna, Dr. Tiago de Faria Pinto, Dr. Zeudi Mazzotta and Amelie Heinzerling for their contribution to the development of the setup. This work was carried out at ARCNL, a public-private partnership between the University of Amsterdam (UvA), Vrije Universiteit Amsterdam (VU), Rijksuniversiteit Groningen (RUG),

the Dutch Research Council (NWO), and the semiconductor equipment manufacturer ASML.

Declarations

Conflicts of interest The authors declare that they have no conflicts of interest.

Bibliography

[1] G. E. Moore, *Cramming more components onto integrated circuits, Reprinted from Electronics, volume 38, number 8, April 19, 1965, pp.114 ff.*, IEEE Solid-State Circuits Society Newsletter **11**(3):33–35 (2006). 1

[2] G. E. Moore, *Progress in digital integrated electronics [Technical literaiture, Copyright 1975 IEEE. Reprinted, with permission. Technical Digest. International Electron Devices Meeting, IEEE, 1975, pp. 11-13.]*, IEEE Solid-State Circuits Society Newsletter **11**(3):36–37 (2006). 1

[3] A. McPherson, G. Gibson, H. Jara, U. Johann, T. S. Luk, I. A. McIntyre, K. Boyer, and C. K. Rhodes, *Studies of multiphoton production of vacuum-ultraviolet radiation in the rare gases*, J. Opt. Soc. Am. B **4**(4):595–601 (1987). Publisher: Optica Publishing Group. 2, 60

[4] M. Ferray, A. L'Huillier, X. F. Li, L. A. Lompre, G. Mainfray, and C. Manus, *Multiple-harmonic conversion of 1064 nm radiation in rare gases*, Journal of Physics B: Atomic, Molecular and Optical Physics **21**(3):L31 (1988). 2

[5] X. F. Li, A. LHuillier, M. Ferray, L. A. Lompr, and G. Mainfray, *Multiple-harmonic generation in rare gases at high laser intensity*, Physical Review A **39**(11):5751–5761 (1989). 2, 60

[6] F. Krausz and M. Ivanov, *Attosecond physics*, Rev. Mod. Phys. **81**:163–234 (2009). 3, 42

[7] T. Popmintchev, M.-C. Chen, P. Arpin, M. M. Murnane, and H. C. Kapteyn, *The attosecond nonlinear optics of bright coherent X-ray generation*, Nature Photonics **4**(12):822–832 (2010). 3, 5

[8] P. Corkum, *Plasma perspective on strong field multiphoton ionization*, Physical Review Letters **71**(13):1994–1997 (1993). Number: 13. 3, 60, 61

[9] J. L. Krause, K. J. Schafer, and K. C. Kulander, *High-order harmonic generation from atoms and ions in the high intensity regime*, Phys. Rev. Lett. **68**:3535–3538 (1992). 3

[10] S. Roscam Abbing, *Control over Extreme-Ultraviolet High-Harmonic Generation from Gases and Solids*, Phd-thesis - research and graduation internal, Vrije Universiteit Amsterdam (2023). 3

[11] L. Brugnera, D. J. Hoffmann, T. Siegel, F. Frank, A. Zaïr, J. W. G. Tisch, and J. P. Marangos, *Trajectory Selection in High Harmonic Generation by Controlling the Phase between Orthogonal Two-Color Fields*, Phys. Rev.

Lett. **107**:153902 (2011). 4

[12] S. Roscam Abbing, F. Campi, F. S. Sajjadian, N. Lin, P. Smorenburg, and P. M. Kraus, *Divergence Control of High-Harmonic Generation*, Phys. Rev. Applied **13**:054029 (2020). 4

[13] T. T. Liu, T. Kanai, T. Sekikawa, and S. Watanabe, *Significant enhancement of high-order harmonics below* 10 nm *in a two-color laser field*, Phys. Rev. A **73**:063823 (2006). 4

[14] I. J. Kim, C. M. Kim, H. T. Kim, G. H. Lee, Y. S. Lee, J. Y. Park, D. J. Cho, and C. H. Nam, *Highly Efficient High-Harmonic Generation in an Orthogonally Polarized Two-Color Laser Field*, Phys. Rev. Lett. **94**:243901 (2005). 4, 60

[15] S. D. C. Roscam Abbing, F. Campi, A. Zeltsi, P. Smorenburg, and P. M. Kraus, *Divergence and efficiency optimization in polarization-controlled two-color high-harmonic generation*, Scientific Reports **11**(1):24253 (2021). 4, 67

[16] M. B. Gaarde, J. L. Tate, and K. J. Schafer, *Macroscopic aspects of attosecond pulse generation*, Journal of Physics B: Atomic, Molecular and Optical Physics **41**(13):132001 (2008). 5

[17] T. Popmintchev, M.-C. Chen, A. Bahabad, M. Gerrity, P. Sidorenko, O. Cohen, I. P. Christov, M. M. Murnane, and H. C. Kapteyn, *Phase matching of high harmonic generation in the soft and hard X-ray regions of the spectrum*, Proceedings of the National Academy of Sciences **106**(26):10516–10521 (2009). `https://www.pnas.org/doi/pdf/10.1073/pnas.0903748106`. 5

[18] B. N. Chichkov, C. Momma, S. Nolte, F. von Alvensleben, and A. Tünnermann, *Femtosecond, picosecond and nanosecond laser ablation of solids*, Applied Physics A **63**(2):109–115 (1996). 5, 6, 42, 46

[19] X. Wang, S. Zhang, X. Cheng, E. Zhu, W. Hang, and B. Huang, *Ion kinetic energy distributions in laser-induced plasma* (2014). 5, 42

[20] K. Chaudhary, S. Z. H. Rizvi, and J. Ali, *Laser-Induced Plasma and its Applications*, in T. Mieno (editor), *Plasma Science and Technology*, chap. 11, IntechOpen, Rijeka (2016). 5

[21] J. White, P. Dunne, P. Hayden, F. OReilly, and G. OSullivan, *Optimizing 13.5nm laser-produced tin plasma emission as a function of laser wavelength*, Applied Physics Letters **90**(18):181502 (2007). `https://pubs.aip.org/aip/apl/article-pdf/doi/10.1063/1.2735944/8847685/181502_1_online.pdf`. 6

[22] M. Purvis, I. V. Fomenkov, A. A. Schafgans, M. Vargas, S. Rich, Y. Tao, S. I. Rokitski, M. Mulder, E. Buurman, M. Kats, J. Stewart, A. D. LaForge, C. Rajyaguru, G. Vaschenko, A. I. Ershov, *et al.*, *Industrialization of a robust EUV source for high-volume manufacturing and power scaling beyond 250W*, in K. A. Goldberg (editor), *Extreme Ultraviolet (EUV) Lithography IX*, vol. 10583, p. 1058327, International Society for Optics and Photonics, SPIE (2018). 6

[23] R. Schupp, F. Torretti, R. Meijer, M. Bayraktar, J. Scheers, D. Kurilovich, A. Bayerle, K. Eikema, S. Witte, W. Ubachs, R. Hoekstra, and O. Ver-

solato, *Efficient Generation of Extreme Ultraviolet Light From* Nd*:YAG-Driven Microdroplet-Tin Plasma*, Phys. Rev. Applied **12**:014010 (2019). 6, 26

[24] L. Behnke, R. Schupp, Z. Bouza, M. Bayraktar, Z. Mazzotta, R. Meijer, J. Sheil, S. Witte, W. Ubachs, R. Hoekstra, and O. O. Versolato, *Extreme ultraviolet light from a tin plasma driven by a 2-µm-wavelength laser*, Opt. Express **29**(3):4475–4487 (2021). 6, 26

[25] L. Poirier, A. Lassise, Y. Mostafa, L. Behnke, N. Braaksma, L. Assink, R. Hoekstra, and O. O. Versolato, *Energy- and charge-state-resolved spectrometry of tin laser-produced plasma using a retarding field energy analyzer*, Applied Physics B **128**(7):135 (2022). 6, 26, 44

[26] O. O. Versolato, *Physics of laser-driven tin plasma sources of EUV radiation for nanolithography*, Plasma Sources Science and Technology **28**(8):083001 (2019). 6, 36

[27] T. W. Johnston and J. M. Dawson, *Correct values for highfrequency power absorption by inverse bremsstrahlung in plasmas*, The Physics of Fluids **16**(5):722–722 (1973). `https://pubs.aip.org/aip/pfl/article-pdf/16/5/722/12772998/722_1_online.pdf`. 7

[28] P. Mora, *Theoretical model of absorption of laser light by a plasma*, The Physics of Fluids **25**(6):1051–1056 (1982). `https://pubs.aip.org/aip/pfl/article-pdf/25/6/1051/12664532/1051_1_online.pdf`. 7

[29] M. M. Basko, V. G. Novikov, and A. S. Grushin, *On the structure of quasi-stationary laser ablation fronts in strongly radiating plasmas*, Physics of Plasmas **22**(5):053111 (2015). `https://pubs.aip.org/aip/pop/article-pdf/doi/10.1063/1.4921334/13781327/053111_1_online.pdf`. 7

[30] Y. Akiyama, K. Midorikawa, Y. Matsunawa, Y. Nagata, M. Obara, H. Tashiro, and K. Toyoda, *Generation of high-order harmonics using laser-produced rare-gas-like ions*, Phys. Rev. Lett. **69**:2176–2179 (1992). 7, 26, 42

[31] R. Ganeev, M. Suzuki, M. Baba, H. Kuroda, and T. Ozaki, *High-order harmonic generation from boron plasma in the extreme-ultraviolet range*, Opt. Lett. **30**(7):768–770 (2005). 7, 26

[32] R. A. Ganeev, M. Suzuki, M. Baba, and H. Kuroda, *High-order harmonic generation from carbon plasma*, J. Opt. Soc. Am. B **22**(9):1927–1933 (2005). 7, 26

[33] R. Ganeev, M. Baba, M. Suzuki, and H. Kuroda, *High-order harmonic generation from silver plasma*, Physics Letters A **339**(1):103–109 (2005). 7, 26, 38, 60

[34] R. A. Ganeev, M. Suzuki, M. Baba, and H. Kuroda, *33rd harmonic generation from aluminium plasma*, Journal of Modern Optics **53**(10):1451–1458 (2006). `https://doi.org/10.1080/09500340600552265`. 7, 26, 38

[35] V. Strelkov, *Role of Autoionizing State in Resonant High-Order Harmonic Generation and Attosecond Pulse Production*, Phys. Rev. Lett. **104**:123901 (2010). 7

[36] M. A. Fareed, V. V. Strelkov, N. Thiré, S. Mondal, B. E. Schmidt,

F. Légaré, and T. Ozaki, *High-order harmonic generation from the dressed autoionizing states*, Nature Communications **8**(1):16061 (2017). 7, 26, 33, 42

[37] R. A. Ganeev, M. Suzuki, M. Baba, H. Kuroda, and T. Ozaki, *Strong resonance enhancement of a single harmonic generated in the extreme ultraviolet range*, Opt. Lett. **31**(11):1699–1701 (2006). 7, 26, 38, 42, 60

[38] M. Suzuki, M. Baba, R. Ganeev, H. Kuroda, and T. Ozaki, *Anomalous enhancement of a single high-order harmonic by using a laser-ablation tin plume at 47 nm*, Opt. Lett. **31**(22):3306–3308 (2006). 7, 26, 38, 42, 60

[39] R. A. Ganeev, T. Witting, C. Hutchison, F. Frank, M. Tudorovskaya, M. Lein, W. A. Okell, A. Zaïr, J. P. Marangos, and J. W. G. Tisch, *Isolated sub-fs XUV pulse generation in Mn plasma ablation*, Opt. Express **20**(23):25239–25248 (2012). 7

[40] R. A. Ganeev, M. Baba, M. Suzuki, and H. Kuroda, *Optimization of harmonic generation from boron plasma*, Journal of Applied Physics **99**(10):103303 (2006). `https://pubs.aip.org/aip/jap/article-pdf/doi/10.1063/1.2201693/13669855/103303_1_online.pdf`. 7

[41] R. A. Ganeev, L. B. E. Bom, J.-C. Kieffer, and T. Ozaki, *Optimum plasma conditions for the efficient high-order harmonic generation in platinum plasma*, J. Opt. Soc. Am. B **24**(6):1319–1323 (2007). 8

[42] R. A. Ganeev, M. Baba, M. Suzuki, S. Yoneya, and H. Kuroda, *Low- and high-order harmonic generation in the extended plasmas produced by laser ablation of zinc and manganese targets*, Journal of Applied Physics **116**(24):243102 (2014). `https://doi.org/10.1063/1.4905188`. 8, 9, 26, 42

[43] R. A. Ganeev, M. Suzuki, and H. Kuroda, *Quasi-phase-matching-induced enhancement of high-order harmonics during two-colour pump of multi-jet plasmas*, Journal of Physics B: Atomic, Molecular and Optical Physics **47**(10):105401 (2014). 8, 60

[44] R. A. Ganeev, M. Suzuki, M. Baba, and H. Kuroda, *High-order harmonic generation from laser plasma produced by pulses of different duration*, Phys. Rev. A **76**:023805 (2007). 8, 36, 42, 60

[45] S. R. Konda, Y. H. Lai, and W. Li, *Improvement of high-order harmonics from silver plasma plumes induced by femtoseconds laser pulses*, Optics & Laser Technology **146**:107602 (2022). 8

[46] R. A. Ganeev, H. Singhal, P. A. Naik, J. A. Chakera, H. S. Vora, R. A. Khan, and P. D. Gupta, *Systematic studies of two-color pump-induced high-order harmonic generation in plasma plumes*, Physical Review A **82**(5):053831 (2010). 8, 60

[47] R. A. Ganeev, M. Suzuki, and H. Kuroda, *Enhanced harmonic generation using different second-harmonic sources for the two-color pump of extended laser-produced plasmas*, Journal of the Optical Society of America B **31**(4):911 (2014). 8

[48] R. A. Ganeev, G. S. Boltaev, S. Y. Stremoukhov, V. V. Kim, A. V. Andreev, and A. S. Alnaser, *High-order harmonic generation during different overlaps of two-colored pulses in laser-produced plasmas and gases*, The

European Physical Journal D **74**(10):199 (2020). 8, 60

[49] R. A. Ganeev, *High-order harmonics enhancement in laser-induced plasma*, Scientific Reports **13**(1):13951 (2023). 8

[50] C. Hutchison, R. A. Ganeev, T. Witting, F. Frank, W. A. Okell, J. W. G. Tisch, and J. P. Marangos, *Stable generation of high-order harmonics of femtosecond laser radiation from laser produced plasma plumes at 1 kHz pulse repetition rate*, Opt. Lett. **37**(11):2064–2066 (2012). 8, 28

[51] T. de Faria Pinto, J. Mathijssen, K. S. E. Eikema, and S. Witte, *Optical parametric chirped pulse amplifier producing ultrashort 10.5 mJ pulses at 1.55 um*, Opt. Express **27**(21):29829–29837 (2019). 11, 29, 66

[52] I. Fomenkov, D. Brandt, A. Ershov, A. Schafgans, Y. Tao, G. Vaschenko, S. Rokitski, M. Kats, M. Vargas, M. Purvis, R. Rafac, B. La Fontaine, S. De Dea, A. LaForge, J. Stewart, *et al.*, *Light sources for high-volume manufacturing EUV lithography: technology, performance, and power scaling*, Advanced Optical Technologies **6**(3-4) (2017). 12

[53] X. Wang, S. Zhang, X. Cheng, E. Zhu, W. Hang, and B. Huang, *Ion kinetic energy distributions in laser-induced plasma*, Spectrochimica Acta Part B: Atomic Spectroscopy **99**:101–114 (2014). 12

[54] E. Gamaly, *The physics of ultra-short laser interaction with solids at non-relativistic intensities*, Physics Reports **508**(4-5):91–243 (2011). 12

[55] M. M. Basko, M. S. Krivokorytov, A. Yu Vinokhodov, Y. V. Sidelnikov, V. M. Krivtsun, V. V. Medvedev, D. A. Kim, V. O. Kompanets, A. A. Lash, and K. N. Koshelev, *Fragmentation dynamics of liquidmetal droplets under ultra-short laser pulses*, Laser Physics Letters **14**(3):036001 (2017). 12

[56] L. Torrisi, *Ion charge state distributions in plasma produced by pulsed laser irradiations*, Radiation Effects and Defects in Solids **159**(4):249–258 (2004). 12

[57] L. Torrisi, F. Caridi, A. Picciotto, and A. Borrielli, *Energy distribution of particles ejected by laser-generated aluminium plasma*, Nuclear Instruments and Methods in Physics Research Section B: Beam Interactions with Materials and Atoms **252**(2):183–189 (2006). 12

[58] L. Torrisi, F. Caridi, D. Margarone, and A. Borrielli, *Characterization of laser-generated silicon plasma*, Applied Surface Science **254**(7):2090–2095 (2008). 12

[59] F. Caridi, L. Torrisi, D. Margarone, A. Picciotto, A. M. Mezzasalma, and S. Gammino, *Energy distributions of particles ejected from laser-generated pulsed plasmas*, Czechoslovak Journal of Physics **56**(S2):B449–B456 (2006). 12

[60] D. Kurilovich, A. L. Klein, F. Torretti, A. Lassise, R. Hoekstra, W. Ubachs, H. Gelderblom, and O. O. Versolato, *Plasma Propulsion of a Metallic Microdroplet and its Deformation upon Laser Impact*, Physical Review Applied **6**(1) (2016). 12

[61] D. Kurilovich, T. d. F. Pinto, F. Torretti, R. Schupp, J. Scheers, A. S. Stodolna, H. Gelderblom, K. S. Eikema, S. Witte, W. Ubachs, R. Hoekstra, and O. O. Versolato, *Expansion Dynamics after Laser-Induced Cavitation*

in Liquid Tin Microdroplets, Physical Review Applied **10**(5) (2018). 12

[62] A. S. Stodolna, T. de Faria Pinto, F. Ali, A. Bayerle, D. Kurilovich, J. Mathijssen, R. Hoekstra, O. O. Versolato, K. S. E. Eikema, and S. Witte, *Controlling ion kinetic energy distributions in laser produced plasma sources by means of a picosecond pulse pair*, Journal of Applied Physics **124**(5):053303 (2018). 12, 14

[63] A. Bayerle, M. J. Deuzeman, S. v. d. Heijden, D. Kurilovich, T. d. F. Pinto, A. Stodolna, S. Witte, K. S. E. Eikema, W. Ubachs, R. Hoekstra, and O. O. Versolato, *Sn ion energy distributions of ns- and ps-laser produced plasmas*, Plasma Sources Science and Technology **27**(4):045001 (2018). 12

[64] S. Witte, R. T. Zinkstok, W. Hogervorst, and K. S. E. Eikema, *Generation of few-cycle terawatt light pulses using optical parametric chirped pulse amplification*, Optics Express **13**(13):4903 (2005). 12

[65] S. Witte, R. T. Zinkstok, A. L. Wolf, W. Hogervorst, W. Ubachs, and K. S. E. Eikema, *A source of 2 terawatt, 2.7 cycle laser pulses based on noncollinear optical parametric chirped pulse amplification*, Optics Express **14**(18):8168–8177 (2006). 12, 19, 23

[66] S. Witte, R. T. Zinkstok, W. Hogervorst, and K. S. E. Eikema, *Numerical simulations for performance optimization of a few-cycle terawatt NOPCPA system*, Applied Physics B **87**(4):677–684 (2007). 12, 23

[67] F. Tavella, A. Marcinkevicius, and F. Krausz, *90 mJ parametric chirped pulse amplification of 10 fs pulses*, Opt. Express **14**:12822–12827 (2006). 12

[68] M. Schultze, T. Binhammer, A. Steinmann, G. Palmer, M. Emons, and U. Morgner, *Few-cycle OPCPA system at 143 kHz with more than 1 μJ of pulse energy*, Optics Express **18**(3):2836–2841 (2010). 12

[69] S. Prinz, M. Haefner, C. Y. Teisset, R. Bessing, K. Michel, Y. Lee, X. T. Geng, S. Kim, D. E. Kim, T. Metzger, and M. Schultze, *CEP-stable, sub-6 fs, 300-kHz OPCPA system with more than 15 W of average power*, Optics Express **23**(2):1388–1394 (2015). 12

[70] R. Budriunas, T. Stanislauskas, J. Adamonis, A. Aleknaviius, G. Veitas, D. Gadonas, S. Balickas, A. Michailovas, and A. Varanaviius, *53 W average power CEP-stabilized OPCPA system delivering 5.5 TW few cycle pulses at 1 kHz repetition rate*, Optics Express **25**(5):5797–5806 (2017). 12

[71] B. W. Mayer, C. R. Phillips, L. Gallmann, M. M. Fejer, and U. Keller, *Sub-four-cycle laser pulses directly from a high-repetition-rate optical parametric chirped-pulse amplifier at 3.4 μm.*, Optics Letters **38**(21):4265–4268 (2013). 12

[72] G. Andriukaitis, T. Balinas, S. Aliauskas, A. Puglys, A. Baltuka, T. Popmintchev, M.-C. Chen, M. M. Murnane, and H. C. Kapteyn, *90 GW peak power few-cycle mid-infrared pulses from an optical parametric amplifier*, Optics Letters **36**(15):2755 (2011). 12

[73] O. Chalus, P. K. Bates, M. Smolarski, and J. Biegert, *Mid-IR short-pulse OPCPA with micro-Joule energy at 100kHz*, Optics Express **17**(5):3587 (2009). 12

[74] C. Erny, C. Heese, M. Haag, L. Gallmann, and U. Keller, *High-repetition-*

rate optical parametric chirped-pulse amplifier producing 1-μJ, sub-100-fs pulses in the mid-infrared, Optics Express **17**(3):1340 (2009). 12

[75] C. Heese, C. R. Phillips, L. Gallmann, M. M. Fejer, and U. Keller, *Ultra-broadband, highly flexible amplifier for ultrashort midinfrared laser pulses based on aperiodically poled Mg:$LiNbO_3$*, Optics Letters **35**(14):2340 (2010). 12

[76] C. Heese, C. R. Phillips, B. W. Mayer, L. Gallmann, M. M. Fejer, and U. Keller, *75 MW few-cycle mid-infrared pulses from a collinear apodized APPLN-based OPCPA*, Optics Express **20**(24):26888 (2012). 12

[77] D. Kraemer, R. Hua, M. L. Cowan, K. Franjic, and R. J. D. Miller, *Ultrafast noncollinear optical parametric chirped pulse amplification in $KTiOAsO_4$*, Optics Letters **31**(7):981 (2006). 12

[78] D. Kraemer, M. L. Cowan, R. Hua, K. Franjic, and R. J. Dwayne Miller, *High-power femtosecond infrared laser source based on noncollinear optical parametric chirped pulse amplification*, Journal of the Optical Society of America B **24**(4):813 (2007). 12

[79] D. Brida, G. Cirmi, C. Manzoni, S. Bonora, P. Villoresi, S. D. Silvestri, and G. Cerullo, *Sub-two-cycle light pulses at 1.6 μm from an optical parametric amplifier*, Optics Letters p. 3 (2008). 12

[80] D. Brida, G. Krauss, A. Sell, and A. Leitenstorfer, *Ultrabroadband Er:fiber lasers: Ultrabroadband Er:fiber lasers*, Laser & Photonics Reviews **8**(3):409–428 (2014). 12

[81] J. Morgenweg and K. S. E. Eikema, *A 1.8 mJ, picosecond Nd:YVO_4 bounce amplifier pump front-end system for high-accuracy XUV-frequency comb spectroscopy*, Laser Physics Letters **9**(11):781–785 (2012). 13, 14

[82] D. W. E. Noom, S. Witte, J. Morgenweg, R. K. Altmann, and K. S. E. Eikema, *High-energy, high-repetition-rate picosecond pulses from a quasi-CW diode-pumped Nd:YAG system*, Optics Letters **38**(16):3021 (2013). 13, 14, 16

[83] L. Sun, L. Zhang, H. J. Yu, L. Guo, J. L. Ma, J. Zhang, W. Hou, X. C. Lin, and J. M. Li, *880 nm LD pumped passive mode-locked TEM00 Nd:YVO_4 laser based on SESAM*, Laser Physics Letters **7**(10):711 (2010). 13

[84] J. Morgenweg, *Ramsey-comb spectroscopy*, PhD Thesis, Vrije Universiteit Amsterdam (2014). 13

[85] Q. L, N. Kugler, H. Weber, S. Dong, N. Mller, and U. Wittrock, *A novel approach for compensation of birefringence in cylindrical Nd:YAG rods*, Optical and Quantum Electronics **28**(1):57–69 (1996). 16

[86] J. Sherman, *Thermal compensation of a cw-pumped Nd:YAG laser*, Applied Optics **37**(33):7789 (1998). 16

[87] S. Witte and K. S. E. Eikema, *Ultrafast Optical Parametric Chirped-Pulse Amplification*, IEEE Journal of Selected Topics in Quantum Electronics **18**(1):296–307 (2012). 20

[88] R. A. Meijer, A. S. Stodolna, K. S. E. Eikema, and S. Witte, *High-energy Nd:YAG laser system with arbitrary sub-nanosecond pulse shaping capability*, Opt. Lett. **42**(14):2758–2761 (2017). 21, 27, 44, 66

[89] J. Mathijssen, Z. Mazzotta, A. M. Heinzerling, K. S. E. Eikema,

and S. Witte, *Material-specific high-order harmonic generation in laser-produced plasmas for varying plasma dynamics*, Applied Physics B **129**(6):91 (2023). 21, 25, 43, 69, 71, 76

[90] D. Kurilovich, T. d. F. Pinto, F. Torretti, R. Schupp, J. Scheers, A. S. Stodolna, H. Gelderblom, K. S. Eikema, S. Witte, W. Ubachs, R. Hoekstra, and O. O. Versolato, *Expansion Dynamics after Laser-Induced Cavitation in Liquid Tin Microdroplets*, Phys. Rev. Applied **10**:054005 (2018). 26

[91] T. Pinto, J. Mathijssen, R. Meijer, H. Zhang, A. Bayerle, D. Kurilovich, O. Versolato, K. Eikema, and S. Witte, *Cylindrically and non-cylindrically symmetric expansion dynamics of tin microdroplets after ultrashort laser pulse impact*, Applied Physics A **127** (2021). 26

[92] R. A. Meijer, D. Kurilovich, K. S. E. Eikema, O. O. Versolato, and S. Witte, *The transition from short- to long-timescale pre-pulses: Laser-pulse impact on tin microdroplets*, Journal of Applied Physics **131**(10):105905 (2022). `https://doi.org/10.1063/5.0082352`. 26

[93] Z. Bouza, J. Byers, J. Scheers, R. Schupp, Y. Mostafa, L. Behnke, Z. Mazzotta, J. Sheil, W. Ubachs, R. Hoekstra, M. Bayraktar, and O. O. Versolato, *The spectrum of a 1-μm-wavelength-driven tin microdroplet laser-produced plasma source in the 5.5265.5 nm wavelength range*, AIP Advances **11**(12):125003 (2021). `https://doi.org/10.1063/5.0073839`. 26

[94] A. S. Stodolna, T. de Faria Pinto, F. Ali, A. Bayerle, D. Kurilovich, J. Mathijssen, R. Hoekstra, O. O. Versolato, K. S. E. Eikema, and S. Witte, *Controlling ion kinetic energy distributions in laser produced plasma sources by means of a picosecond pulse pair*, Journal of Applied Physics **124**(5):053303 (2018). `https://doi.org/10.1063/1.5033541`. 26

[95] B. Liu, D. Kurilovich, H. Gelderblom, and O. O. Versolato, *Mass Loss from a Stretching Semitransparent Sheet of Liquid Tin*, Phys. Rev. Applied **13**:024035 (2020). 26

[96] L. Poirier, A. Bayerle, A. Lassise, F. Torretti, R. Schupp, L. Behnke, Y. Mostafa, W. Ubachs, O. O. Versolato, and R. Hoekstra, *Cross-calibration of a combined electrostatic and time-of-flight analyzer for energy- and charge-state-resolved spectrometry of tin laser-produced plasma*, Applied Physics B **128**(3):39 (2022). 28

[97] A. Kramida, Yu. Ralchenko, J. Reader, and and NIST ASD Team, NIST Atomic Spectra Database (ver. 5.10), [Online]. Available: `https://physics.nist.gov/asd` [2022, November 29]. National Institute of Standards and Technology, Gaithersburg, MD. (2022). 31, 73, 74

[98] N. B. Delone and V. P. Krainov, *Tunneling and barrier-suppression ionization of atoms and ions in a laser radiation field*, Physics-Uspekhi **41**(5):469–485 (1998). 38

[99] A. Bayerle, M. J. Deuzeman, S. V. D. Heijden, D. Kurilovich, T. D. D. F. Pinto, A. Stodolna, S. Witte, K. S. Eikema, W. Ubachs, R. Hoekstra, and O. O. Versolato, *Sn ion energy distributions of ns- A nd ps-laser produced plasmas*, Plasma Sources Science and Technology **27** (2018). 42

[100] L. Poirier, A. Lassise, R. Hoekstra, J. Sheil, and O. O. Versolato, *Dependence of ion charge-energy emission from Nd:YAG-laser-produced plasma*

on laser intensity in the 0.4 - 40 10 10 W/cm2 range, Physics of Plasmas **30** (2023). 42

[101] T. de Faria Pinto, *Interactions between ultrashort pulses and laser-produced tin plasmas*, Ph.D. thesis, Vrije Universiteit, Amsterdam (2023). 42

[102] G. S. Boltaev, R. A. Ganeev, V. V. Kim, N. A. Abbasi, M. Iqbal, and A. S. Alnaser, *High-order harmonics generation in the plasmas produced on different rotating targets during ablation using 1 kHz and 100 kHz lasers*, Opt. Express **28**(13):18859–18875 (2020). 43

[103] R. A. Meijer, D. Kurilovich, B. Liu, Z. Mazzotta, J. Hernandez-Rueda, O. O. Versolato, and S. Witte, *Nanosecond laser ablation threshold of liquid tin microdroplets*, Applied Physics A **128**(7):570 (2022). 46

[104] D. J. Hemminga, L. Poirier, M. M. Basko, R. Hoekstra, W. Ubachs, O. O. Versolato, and J. Sheil, *High-energy ions from Nd:YAG laser ablation of tin microdroplets: comparison between experiment and a single-fluid hydrodynamic model*, Plasma Sources Science and Technology **30**(10):105006 (2021). 53

[105] J. Mathijssen, E. J. Salumbides, K. S. E. Eikema, and S. Witte, *Subcycle dynamics in two-color high-harmonic generation from laser-produced plasmas*, Opt. Express **32**(17):30824–30838 (2024). 59

[106] P. A. Franken, A. E. Hill, C. W. Peters, and G. Weinreich, *Generation of Optical Harmonics*, Phys. Rev. Lett. **7**:118–119 (1961). 60

[107] G. H. C. New and J. F. Ward, *Optical Third-Harmonic Generation in Gases*, Phys. Rev. Lett. **19**:556–559 (1967). 60

[108] M. Lewenstein, P. Balcou, M. Y. Ivanov, A. LHuillier, and P. B. Corkum, *Theory of high-harmonic generation by low-frequency laser fields*, Physical Review A **49**(3):2117–2132 (1994). Number: 3. 60, 61

[109] P. M. Paul, E. S. Toma, P. Breger, G. Mullot, F. Aug, P. Balcou, H. G. Muller, and P. Agostini, *Observation of a Train of Attosecond Pulses from High Harmonic Generation*, Science **292**(5522):1689–1692 (2001). `https://www.science.org/doi/pdf/10.1126/science.1059413`. 60

[110] M. A. Fareed, V. V. Strelkov, N. Thir, S. Mondal, B. E. Schmidt, F. Lgar, and T. Ozaki, *High-order harmonic generation from the dressed autoionizing states*, Nature Communications **8**(1) (2017). Number: 1. 60, 76

[111] R. Ganeev, *High-order harmonic generation in laser plasma: Recent achievements*, Journal of Physics B: Atomic, Molecular and Optical Physics **40**:R213 (2007). 60

[112] N. Dudovich, O. Smirnova, J. Levesque, Y. Mairesse, M. Y. Ivanov, D. M. Villeneuve, and P. B. Corkum, *Measuring and controlling the birth of attosecond XUV pulses*, Nature Physics **2**(11):781–786 (2006). 60, 61, 67, 75

[113] R. A. Ganeev, J. A. Chakera, P. A. Naik, H. Singhal, R. A. Khan, and P. D. Gupta, *Resonance enhancement of single even harmonic of laser radiation in tin-containing plasma using intensity variation of two-color pump*, Journal of the Optical Society of America B **28**(5):1055 (2011). 60

[114] R. A. Ganeev, C. Hutchison, A. Zar, T. Witting, F. Frank, W. A. Okell, J. W. G. Tisch, and J. P. Marangos, *Enhancement of high harmonics from*

plasmas using two-color pump and chirp variation of 1 kHz Ti:sapphire laser pulses, Optics Express **20**(1):90 (2012). 60

[115] D. Shafir, H. Soifer, B. D. Bruner, M. Dagan, Y. Mairesse, S. Patchkovskii, M. Y. Ivanov, O. Smirnova, and N. Dudovich, *Resolving the time when an electron exits a tunnelling barrier*, Nature **485**(7398):343–346 (2012). 60, 61, 65, 67, 75

[116] D. Shafir, Y. Mairesse, D. M. Villeneuve, P. B. Corkum, and N. Dudovich, *Atomic wavefunctions probed through strong-field light–matterinteraction*, Nature Physics **5**(6):412–416 (2009). 60, 64, 67, 75

[117] L. Torlina and O. Smirnova, *Coulomb time delays in high harmonic generation*, New J. Phys. **19**(2):023012 (2017). 61

[118] S. Yue, S. Xue, H. Du, and M. Lein, *Revealing Coulomb time shifts in high-order harmonic generation by frequency-dependent streaking*, Phys. Rev. A **105**(4):L041103 (2022). 61

[119] S. Yue, J. Liu, S. Xue, H. Du, and M. Lein, *Observing the Coulomb shifts of ionization times in high-order harmonic generation*, Phys. Rev. A **107**(6):063102 (2023). 61

[120] X. He, J. M. Dahlström, R. Rakowski, C. M. Heyl, A. Persson, J. Mauritsson, and A. L'Huillier, *Interference effects in two-color high-order harmonic generation*, Phys. Rev. A **82**:033410 (2010). 61, 65, 75

[121] L. Young, D. A. Arms, E. M. Dufresne, R. W. Dunford, D. L. Ederer, C. Höhr, E. P. Kanter, B. Krässig, E. C. Landahl, E. R. Peterson, J. Rudati, R. Santra, and S. H. Southworth, *X-Ray Microprobe of Orbital Alignment in Strong-Field Ionized Atoms*, Phys. Rev. Lett. **97**:083601 (2006). 63, 64

[122] I. H. Malitson, *Interspecimen Comparison of the Refractive Index of Fused Silica*, J. Opt. Soc. Am. **55**(10):1205–1209 (1965). 67

[123] J. Scheers, R. Schupp, R. Meijer, W. Ubachs, R. Hoekstra, and O. O. Versolato, *Time- and space-resolved optical Stark spectroscopy in the afterglow of laser-produced tin-droplet plasma*, Phys. Rev. E **102**:013204 (2020). 74

[124] G. Doumy, J. Wheeler, C. Roedig, R. Chirla, P. Agostini, and L. F. DiMauro, *Attosecond Synchronization of High-Order Harmonics from Midinfrared Drivers*, Phys. Rev. Lett. **102**:093002 (2009). 75

[125] J. M. Dahlström, T. Fordell, E. Mansten, T. Ruchon, M. Swoboda, K. Klünder, M. Gisselbrecht, A. L'Huillier, and J. Mauritsson, *Atomic and macroscopic measurements of attosecond pulse trains*, Phys. Rev. A **80**:033836 (2009). 75

List of Publications

Chapter 2
T. de Faria Pinto, J. Mathijssen, K. S. E. Eikema, and S. Witte, "*Optical parametric chirped-pulse amplifier producing ultrashort 10.5 mJ pulses at 1.55μm*," Optics Express 27, 29829 (2019).

Chapter 3
J. Mathijssen, Z. Mazzotta, A. Heinzerling, K. S. E. Eikema, and S. Witte, "*Material-specific high-order harmonic generation in laser-produced plasmas for varying plasma dynamics*," Applied Physics B 129 (6), 91 (2023).

Chapter 4
J. Mathijssen, E. Salumbides, K. S. E. Eikema, and S. Witte, "*Laser-Induced Plasma Dynamics Probed with High-Order Harmonic Generation*," in preparation.

Chapter 5
J. Mathijssen, E. Salumbides, K. S. E. Eikema, and S. Witte, "*Sub-cycle dynamics in two-color high-harmonic generation from laser-produced plasmas*," Optics Express 32, 30824-30838 (2024).

The author also contributed to the following publications

1. A. S. Stodolna, T. de Faria Pinto, F. Ali, A. Bayerle, D. Kurilovich, J. Mathijssen, R. Hoekstra, O. O. Versolato, K. S. E. Eikema, S. Witte, "*Controlling ion kinetic energy distributions in laser produced plasma sources by means of a picosecond pulse pair*," Journal of Applied Physics 124, 053303 (2018).

2. T. de Faria Pinto, J. Mathijssen, R. Meijer, H. Zhang, A. Bayerle, D. Kurilovich, O. O. Versolato, K. S. E. Eikema, S. Witte, "*Cylindrically and non-cylindrically symmetric expansion dynamics of tin microdroplets after ultrashort laser pulse impact*," Applied Physics A 127, 93 (2021).

Summary

The discovery of high-order harmonic generation (HHG) in the late eighties of the previous century has enabled us to produce coherent light with an incredibly broad wavelength range extending in the extreme-ultraviolet (EUV) range. The process that generates these burst of EUV radiation occurs when a high-intensity femtosecond laser interacts nonlinearly with a generation medium. Although the efficiency of the HHG process is intrinsically very low, the short wavelengths which are generated in this process allow for high-resolution imaging, facilitating metrology applications such as coherent diffractive imaging or ptychography. Furthermore, the extremely short duration of the generated EUV bursts allow for measuring dynamics at attosecond timescales.

The HHG process is typically driven in one of the noble gases. However, the desire to further extend the highest reachable photon energy has motivated researchers to perform HHG experiments with laser-produced plasmas (LPPs) as the generation medium. With the wide availability of generation media, an interesting finding for driving HHG in LPPs has been that the more complex atomic structures of some generation media has allowed for resonant enhancement up to two orders of magnitude of a single harmonic, resulting in a bright quasi-monochromatic light source in the EUV region. Although significant progress has been made to increase the efficiency of HHG in LPPs, experiments focusing on the effects of plasma charge state composition and fundamental pulse parameters have remained scarce. Therefore, this thesis aims to contribute to the fundamental understanding of HHG in LPPs. To this extent, we perform systematic studies on how varying laser parameters of both pump and fundamental beams affect the HHG process as well as the resulting laser-produced plasmas. Below, we specify the contents of this thesis chapter by chapter.

Chapter 2 of this thesis describes the two laser systems which are needed for the HHG in LPP experiments. The first laser system (producing the 'fundamental' beam) is an optical parametric chirped-pulse amplifier (OPCPA) which drives the highly nonlinear HHG process within the plasma plumes. The pump laser for this femtosecond laser is a picosecond solid-state laser system with a central wavelength of 1064 nm and operates at a repetition frequency of 100 Hz. The maximum output pulse energy is intensity limited and reaches up to 180 mJ for the longest pulse duration of 100 ps. This pulse energy is divided over the three nonlinear amplification stages of the OPCPA system, utilizing KTA crystals as gain medium. The OPCPA is seeded by a commercial erbium-doped fs fiber

laser which outputs 90 fs, 3.5 nJ pulses with a central wavelength of 1560 nm. The amplified pulses are compressed to a pulse length of 180 fs and have energies up to 10.5 mJ. The second laser system (pump) described in this chapter is responsible for driving the plasma generation. It is a nanosecond laser system with many similarities to the pump laser of the femtosecond HHG driving laser. Its 1064 nm CW seed laser can be intensity modulated with a resolution of 0.43 ns by an AOM and a pair of EOMs to generate a pulsed output at 100 Hz with a temporal shape that is pre-compensated for the temporal gain dynamics of both subsequent amplifiers. Pulses with energies ranging between 270 and 450 mJ can be emitted by this system after full amplification, depending on the emitted pulse length. For the HHG experiments performed in this thesis, the pump pulse energy is limited to 20 mJ.

In Chapter 3, we report on our experimental setup for the HHG in LPP measurements. This vacuum vessel comprises an experimental chamber where the plasma formation and the HHG takes place, and an EUV spectrometer with which the HHG spectra are measured. Besides recording HHG spectra, our experimental setup also allows us to measure ion kinetic energy distributions from the generated plasma plumes with retarding field analyzer (RFA) Faraday cup detectors. With this experimental setup, we display initial HHG spectra obtained from our aluminium, nickel, silver, indium, and tin targets. Each element shows a distinct harmonic spectrum with clear variations in overall brightness, as well as the highest harmonic order generated in the plasma plume. A very bright seventh harmonic has been generated in aluminium plasmas. Nickel and silver HHG spectra are more than two orders of magnitude less bright compared to the aluminium HHG spectrum. The highest-order harmonic generated is harmonic 25, which has only been observed with tin plasma. We also report on the optimization procedure of HHG in tin plasmas by tweaking the pulse energies of both pump and probe laser pulses, as well as the delay between these two pulses. This latter parameter accurately depicts the expansion evolution of the plasma plume into the vacuum chamber. Finally, we compare the differences in HHG spectra generated in plasma plumes pumped with short 0.5 ns pulses and longer 50 ns pulses, and we show the difference in plasma expansion dynamics for these two plasmas.

We further investigate the effects of the pump laser parameters on the HHG spectra produced in tin plasmas in Chapter 4. To this extent, we have investigated HHG spectra generated in tin plasmas which have been formed by pump pulses of different shapes (square or Gaussian), different pulse durations (0.5 ns to 50 ns), and varying pump to fundamental delay (50 ns to 150 ns). Furthermore, we separately acquired ion kinetic energy distributions with the RFA detectors.

From our RFA measurements, we observe that pump pulses with shorter durations create denser plasmas containing more ions with higher kinetic energies compared to longer pump pulses. LPPs pumped with Gaussian-shaped pulses yield a lower ion count, while the average charge state composition of this plasma is higher compared to LPPs generated with square-shaped pulses. The higher average charge state composition of the LPPs pumped by the short, Gaussian-shaped pump pulses leads to a higher generation efficiency of the highest-order

harmonics up to H25. Longer pump pulses result in more efficient generation of lower order harmonics. Especially the 50 ns-long square pump pulse has shown a very bright ninth harmonic.

The overall shape of the HHG spectrum also shifts from shorter to longer wavelengths with increasing delay between pump and fundamental laser pulses. As also has been observed in Chapter 3, plasmas generated with shorter pump pulses show different expansion dynamics compared to plasmas generated with longer pump pulses. For the 2 ns pump pulses, highest HHG signal strengths are observed for delays around 100 ns, while the maximum delay of 150 ns yields the most bright harmonics for longer 50 ns pump pulses.

In the final chapter of this thesis, Chapter 5, we investigate the influence of a two-color drive field on the HHG spectra generated in laser-produced aluminium and tin plasmas. Here, we focus on the lower-order harmonics. We first present a theoretical framework for HHG with orthogonally polarized two-color driving fields, and then present the experimental realization by adding a second harmonic generation stage to the experimental setup described in Chapter 3. This setup converts a fraction of the fundamental laser beam into its second harmonic with a BBO crystal. We record HHG spectra as a function of the relative phase between the fundamental field and its second harmonic. In these spectra, we observe oscillatory HHG signals. The aluminium HHG spectra show oscillations mostly for even harmonics, while HHG spectra in tin show oscillations for both even and odd harmonics. The oscillations of individual harmonics are not in phase with each other and show large phase jumps between neighboring harmonics, indicating that in our regime, the electron trajectories of individual harmonics are not solely governed by the electric fields of the driving fields. Instead, these experiments confirm that contributions from the atomic Coulomb potential cannot be neglected when driving HHG in conditions where the strong field approximation does not hold.

Samenvatting

De ontdekking van hoge harmonische generatie (HHG) aan het einde van de jaren tachtig van de vorige eeuw heeft het mogelijk gemaakt om coherent licht te produceren met een grote bandbreedte welke tot in het extreem ultraviolet (EUV) reikt. Het proces dat deze kortstondige pulsen van EUV licht genereert is een niet-lineaire interactie tussen een femtoseconde laser met hoge intensiteit en materie. Hoewel de efficiëntie van dit proces intrinsiek erg laag is, faciliteren de korte golflengtes van het geproduceerde licht coherente beeldvormingstechnieken met enorm hoge resolutie zoals coherente diffractieve beeldvorming of ptychografie. Verder is de tijdsduur van de gegenereerde EUV pulsen enorm kort, wat het meten van snelle processen op attoseconde tijdschaal mogelijk maakt.

Het HHG proces vindt gebruikelijk plaats in een edelgas. De wens om licht te produceren met nog hogere foton energieën heeft echter onderzoekers gemotiveerd om te zoeken naar andere media zoals laser-geproduceerde plasmas (LPPs). De grote variatie in media die dan beschikbaar is heeft onder andere geleid tot de ontdekking dat de complexe atoomstructuur van sommige LPPs kan leiden tot resonante versterking tot twee ordes van grootte van een enkele hogere harmonische, resulterend in een heldere quasi-monochromatische lichtbron in het EUV bereik. Hoewel het produceren van HHG straling in LPPs een significante verbetering heeft ondergaan, blijven studies naar effecten van de ladingstoestand van het plasma en parameters van de fundamentele laser op het HHG spectrum schaars. Daarom beoogt dit proefschrift om bij te dragen aan het fundamenteel begrip van HHG in LPPs.

Hoofdstuk 2 van dit proefschrift beschrijft de twee lasersystemen die worden gebruikt voor de HHG in LPP experimenten. Het eerste lasersysteem, welke de "fundamentele pulsen" levert, is een optische, parametrische versterker van gechirpte pulsen (OPCPA). Deze laser drijft het niet-lineaire HHG proces in de LPPs aan. De pomplaser voor deze OPCPA is een vaste-stof picoseconde laser met een golflengte van 1064 nm en heeft een pulsfrequentie van 100 Hz. Zijn maximale pulsenergie bedraagt 180 mJ voor de langste pulsduur van 100 ps. Deze pulsenergie wordt in de OPCPA verdeeld over de drie niet-lineaire versterkingstrappen, waarbij KTA kristallen worden gebruikt als versterkingsmateriaal. De OPCPA versterkt een fiberlaser met een golflengte van 1560 nm, pulsduur van 90 fs, en een initiële pulsenergie van 3.5 nJ. Deze pulsen worden versterkt tot een energie van 10.5 mJ met een pulsduur van 180 fs. Het tweede lasersysteem is een nanoseconde lasersysteem met grote gelijkenissen aan de pomp laser van het OP-

CPA systeem. Deze laser is verantwoordelijk voor het maken van de LPPs. De continue laser die wordt versterkt in dit systeem kan in intensiteit worden gemoduleerd door een AOM en twee EOMs. Hierdoor worden pulsen gegenereerd met een herhalingsfrequentie van 100 Hz. De pulsvorm van deze pulsen wordt voor de versterker gecompenseerd voor vervormingen tijdens de versterking. Pulsen met energieën tussen 270 en 450 mJ kunnen door dit systeem worden geproduceerd, afhankelijk van de pulsduur. Voor de HHG in LPP experimenten is de maximale pulsenergie gelimiteerd tot 20 mJ.

In hoofdstuk 3 rapporteren we over de experimentele opstelling voor onze HHG in LPP metingen. Dit vacuümvat bestaat uit een kamer waarin de plasma generatie en het HHG proces plaatsvinden, en een EUV spectrometer waarmee de HHG spectra worden gemeten. Naast de EUV spectrometer bevat onze experimentele opstelling ook twee "vertraagd veld analysator (RFA)" Faraday cups waarmee de kinetische energie distributies van de ionen uit het plasma kunnen worden gemeten. Met deze experimentele opstelling tonen we initiële HHG spectra geproduceerd in aluminium, nikkel, zilver, indium en tin plasmas. Ieder element vertoont een uniek HHG spectrum met verschillen in zowel helderheid als de hoogst behaalde harmonische orde. We genereren een enorm heldere zevende harmonische in aluminium plasmas. HHG spectra geproduceerd in nikkel en zilver zijn twee orders van grootte zwakker dan de andere metalen. De hoogste harmonische is orde 25, welke alleen is gedetecteerd met tin plasmas. We doen ook een optimalisatieprocedure voor HHG met tin plasmas. Hierbij variëren we de pulsenergieën van beide lasers, als ook het verschil in aankomsttijd tussen de twee laserpulsen. Deze laatste parameter controleert de expansie van het LPP in de vacuümkamer. Ten slotte maken we een vergelijking tussen HHG in plasma's die zijn gemaakt door korte pomp pulsen van 0.5 ns en langere pomp pulsen van 50 ns. Hierbij tonen we ook de verschillende expansiedynamiek voor deze twee plasma's.

We breiden dit onderzoek naar effecten van de pomp laser op de HHG spectra geproduceerd in tin plasma's uit in hoofdstuk 4. Hiervoor variëren we de temporele vorm van de pomp pulsen (Gaussiaans en een blokpuls), de pulsduur van de pomp pulsen (tussen 0.5 ns en 50 ns), en het verschil in aankomsttijd tussen de pomp puls en de fundamentele puls (tussen de 500 ns en 150 ns). Verder meten we de kinetische energieën van de plasma ionen met de RFA detectoren in onafhankelijke metingen. In deze ion metingen observeren we dat de dichtheid van plasma's geproduceerd door korte pulsen hoger is en de ionen meer kinetische energie hebben in vergelijking met plasma's geproduceerd met langere pulsen. LPPs geproduceerd met Gaussiaanse pulsen bevatten minder ionen, hoewel de gemiddelde ladingstoestand hoger ligt. De hogere gemiddelde ladingstoestand van LPPs gevormd door korte Gaussiaanse pulsen resulteert in een hogere efficiëntie voor het genereren van de hoogste-orde harmonischen tot orde 25. Langere pulsen resulteren in efficiëntere generatie van lagere orde harmonischen. Het zwaartepunt van het HHG spectrum verschuift ook naar langere golflengtes met grotere tijdsverschillen tussen pomp en fundamentele puls. Zoals ook geobserveerd in hoofdstuk 3 vertonen plasma's verschillende dynamiek als ze worden gegenereerd door kortere of langere pulsen. Voor de 2 ns pulsen ligt de ideale

pump tot fundamentele tijdsverschil op 100 ns, terwijl op het grootst gemeten tijdsverschil van 150 ns de meest heldere harmonischen worden gegenereerd in plasma's geproduceerd door lange 50 ns pulsen.

In het laatste hoofdstuk van dit proefschrift, hoofdstuk 5, onderzoeken we de invloed van een tweekleurig fundamenteel veld op de HHG spectra die we in aluminium en tin plasma's produceren. Hier richten we ons op de lagere-orde harmonischen. Hiertoe presenteren we eerst een theoretisch kader voor tweekleurig HHG met orthogonaal gepolariseerde velden. Daarna beschrijven we onze experimentele realisatie van ons tweekleurig HHG experiment met orthogonale polarisatie. In deze opstelling converteren we een klein deel van onze fundamentele laser naar zijn tweede harmonische met behulp van een BBO kristal. We meten HHG spectra als functie van het faseverschil tussen het fundamentele veld en zijn tweede harmonische. De intensiteiten van de verschillende harmonischen oscilleren als functie van deze fase. De aluminium HHG spectra vertonen deze oscillaties voornamelijk bij de even harmonischen, terwijl de tin HHG spectra oscillaties vertonen bij zowel even als oneven harmonischen. Opvallend hierbij is dat de oscillaties van de harmonischen bij zowel aluminium HHG als tin HHG niet in fase lopen en er zelfs grote sprongen in fase zijn tussen opvolgende harmonischen. Dit is een sterke indicatie dat, binnen ons regime, de elektron trajecten van individuele harmonischen niet alleen worden bepaald door het gecombineerd elektrisch veld van de fundamentele lasers. In plaats daarvan bevestigen onze experimenten dat de contributie van de atoompotentiaal niet verwaarloosbaar is in omstandigheden waarbij de sterke veld aanname geen stand houdt.

Acknowledgements

Now that my time as a PhD student at ARCNL has come to an end, I wish to thank all the people who have supported me along the way. You have all made this PhD an enjoyable experience which I will remember forever. I would like to start by thanking all the group members of the EUVGI group.

Stefan, after finishing my master's project under your supervision, I decided to prolong my time in your lab and start my PhD. During all the time I have spent in your group, you have always provided kind support, valuable guidance, patience and trust in me. Together, we set course on this journey which now leaves me proud of the results presented in this thesis. Kjeld, I always enjoyed our discussions and much appreciated your feedback during all group meetings. I could always count on your endless knowledge on lasers.

Tiago, thank you for teaching me all the ins and outs of the laser system. Your initial supervision for laser alignment and early beamtimes during my master's project and start of the PhD has been invaluable while working in the lab. Even after you left our group, I could occasionally ask you to remind me of some specific details about the setup.

Zeudi, you must have been the most colorful appearance within ARCNL. Sharing the lab with you has always been a pleasure. Merging our projects to use the SNS for plasma harmonics has really accelerated the project and boosted my motivation for all experiments. Thank you for turning the lab into a lively atmosphere. Amelie, thank you for all your contributions to rebuilding the laser system after the move, and for your help with redesigning the Spanish Inquisition setup towards HHG in LPPs. Edcel, many thanks for all your help during the final experiments of my PhD journey.

Randy, we have shared the lab space for many years and I appreciate all your help with the SNS. We were also sharing opposite desks in the office, which at some times might not have been the optimal choice given our long legs. Maisie, you were always on the other side of the laser safety curtains. Thanks for occasionally lending me a hand in the lab. Also, many thanks for your culinary advise whenever we visited a Chinese restaurant. Kevin, it was great to have you in the lab next door. We visited each other's lab countless times to restock or to ask for help with the laser systems. These distractions were sometimes just the thing I needed during a rough day in the lab. Sharing laser frustrations and spending breaks with you has resulted in a wonderful friendship. Also many thanks for teaching how to work with the FIB. Anne, Antonios and Fengling, many thanks

for all the useful discussions we had on lasers and HHG, and of course also for your friendship. I would also like to thank all of the other EUVGI group members for the useful discussions, the nice lunches and coffee breaks we shared. In particular I would like to mention Ale, Aneta, Hao, Patrick, Matthias, Matthijs and Maksym. Lucas, being able to borrow your RFAs, and you helping me with the analysis of the ion traces is much obliged.

Without the support of the lab technicians at ARCNL my PhD journey would have looked a lot different. Nik, thank you for all your efforts to make the lab both a safer and a more efficient workspace. I still greatly value the remote control for the lights of the optical table which has helped me greatly to align critical parts of the laser system. Besides that, thank you for all the mental support, life advice, numerous casual conversations, and for lending me your concrete drill. Arend-Jan, thank you for always being around whenever I had some issue with my vacuum setup and for lending some components to keep me going. Here, I also wish to thank the AMOLF support team and the Nanolab staff. In particular, I wish to thank Henkjan for the 3D design of the EUV spectrometer, Marco for the support on the "Spanish Inquisition" software.

I would also like to express my gratitude to the ARCNL management team. Joost, Marjan and Wim, thank you for keeping ARCNL running smoothly, even with the move to the new building. You have created a unique working environment in which I really enjoyed working. Additionally, I want to thank the ARCNL secretary for all of their support. In particular, I wish to mention Cathelijne, Rosa, Romy, and Marja.

Naturally, I also wish to thank all my fellow PV members Viktor, Maisie, Vanessa, Görsel, Maarten, Fiona, John, Zazo, Lucas, Yahia, Ksenia, Ester, Sylvianne, Neha. Together, we organized some amazing events like the potlucks, movie nights, pub quiz, and the ARCNL outings. I will always remember our epic roaring 20's Christmas party and the (maybe slightly too) competitive foosball tournaments. Randy, "Lange en Jan" made a great team for these competitions. Matthias, I will fondly look back to our friendship and our foosball rivalry. Thanks to the complete ARCNL family for participating in all the PV events and all the nice chats we had.

To all my friends outside of work, all the dinners and board game nights with you have greatly helped me to relax during the weekends, thanks guys! Mark, Sjoerd, thanks for always being there for me, listening to my complaints about again having to realign the laser, and for showing me all corners on the squash court. Leander, thanks for your friendship, your interest in my work, all the nice dinners we shared and the many hours of Tribes we played.

Mam, pap, thanks for supporting me throughout my life and for stimulating my interest in science and experimenting. To my brothers, Arnold, Ralph, and Lucas, thank you for all your support and encouragement. Rudie, Linda, thanks for always welcoming me at your place, and for all the support you have given me.

Finally, I cannot thank you enough Eline, as you have been around for this complete adventure and have always provided lots of love and support. Also, many thanks for all your care during the last phases of my PhD so I could finish

this thesis more efficiently. Together, we have been so fortunate to welcome both Jules and Guus during my PhD. I have never been happier with our family and will always be grateful for this joy. Jules, thank you for helping me with “typing” the final bits of this booklet.